UNIVERSIDADE FEDERAL FLUMINENSE
ESCOLA DE ENGENHARIA
PROGRAMA DE PÓS-GRADUAÇÃO EM ENGENHARIA ELÉTRICA E DE TELECOMUNICAÇÕES

TIAGO OGIONI COSTALONGA

Unmanned Aircraft System's Radar Detection: Statistical Analysis and Modeling of the Radar-Cross Section

NITERÓI

2024

UNIVERSIDADE FEDERAL FLUMINENSE
ESCOLA DE ENGENHARIA
PROGRAMA DE PÓS-GRADUAÇÃO EM ENGENHARIA ELÉTRICA E DE TELECOMUNICAÇÕES

TIAGO OGIONI COSTALONGA

Unmanned Aircraft System's Radar Detection: Statistical Analysis and Modeling of the Radar-Cross Section

Dissertação de Mestrado apresentada ao Programa de Pós-Graduação em Engenharia Elétrica e de Telecomunicações da Universidade Federal Fluminense como requisito parcial para a obtenção do título de Mestre em Engenharia Elétrica e de Telecomunicações. Área de concentração: Sistemas de Telecomunicações.

Orientador:
D.Sc. Victor Fernandes

Co-orientadora:
D.Sc. Vanessa Przybylski Ribeiro Magri

NITERÓI

2024

Ficha catalográfica automática - SDC/BEE
Gerada com informações fornecidas pelo autor

C837u Costalonga, Tiago Ogioni
Unmanned Aircraft System's Radar Detection: Statistical Analysis and Modeling of the Radar-Cross Section / Tiago Ogioni Costalonga. - 2024.
108 p.: il.

Orientador: Victor Fernandes.
Coorientador: Vanessa Przybylski Ribeiro Magri.
Dissertação (mestrado)-Universidade Federal Fluminense, Escola de Engenharia, Niterói, 2024.

1. Radar. 2. Drone. 3. Seção reta radar. 4. Estatística. 5. Produção intelectual. I. Fernandes, Victor, orientador. II. Magri, Vanessa Przybylski Ribeiro, coorientadora. III. Universidade Federal Fluminense. Escola de Engenharia. IV. Título.

CDD - XXX

Bibliotecário responsável: Debora do Nascimento - CRB7/6368

TIAGO OGIONI COSTALONGA

Unmanned Aircraft System's Radar Detection: Statistical Analysis and Modeling of the Radar-Cross Section

Dissertação de Mestrado apresentada ao Programa de Pós-Graduação em Engenharia Elétrica e de Telecomunicações da Universidade Federal Fluminense como requisito parcial para a obtenção do título de Mestre em Engenharia Elétrica e de Telecomunicações. Área de concentração: Sistemas de Telecomunicações.

Aprovada em 16 de março de 2024.

BANCA EXAMINADORA

Victor Fernandes

Prof. Victor Fernandes, D.Sc. – Orientador, UFF

Profª. Vanessa P. R. Magri, D.Sc. – Coorientadora, UFF

Roberto Brauer Di Renna

Prof. Roberto Brauer Di Renna, D.Sc. – UFF

Guilherme Ribeiro Colen

Prof. Guilherme Ribeiro Colen, D.Sc. – CIAA-MB

Niterói

2024

À minha filha, Sofia, que você sempre tenha a curiosidade de aprender, a coragem de questionar e a sabedoria para entender.

Acknowledgment

Primeiramente, gostaria de expressar minha profunda gratidão a Deus e à Nossa Senhora Aparecida, por me concederem a força e a perseverança necessárias para concluir este trabalho.

Aos meus pais, que sempre foram minha fonte de inspiração e encorajamento, meu mais sincero agradecimento. Vocês me ensinaram o valor do trabalho duro e da dedicação, e eu sou eternamente grato por isso.

À minha esposa, Mirella, e à nossa filha, Sofia, agradeço de coração. Sua paciência, apoio e amor incondicional foram fundamentais durante este processo e, sem vocês do meu lado, nada disso seria possível. Vocês estiveram comigo em cada passo desse caminho. Amo vocês.

Aos meus orientadores, Victor Fernandes e Vanessa Magri, agradeço pela orientação, paciência e conhecimento compartilhados. Vocês foram essenciais para a realização deste trabalho.

Aos meus amigos, agradeço pelo apoio e pelas palavras de incentivo nos momentos de dificuldade. Vocês tornaram esta jornada muito mais agradável.

Ao Artur Martini Coelho Brandão, da empresa AMB Serviços Eletrônicos, agradeço pela disponibilização e manutenção do radar Furuno FAR-2117 e ao Capitão de Fragata Vieira e ao servidor civil Rafael Assis, do CASNAV, pelo empréstimo de um radar FMCW da Marinha do Brasil. Estes equipamentos foram cruciais para a realização das minhas pesquisas.

Por fim, gostaria de expressar minha gratidão à Marinha do Brasil, pela oportunidade de cursar o mestrado. Esta experiência foi fundamental para o meu crescimento pessoal e profissional.

Este trabalho é dedicado a todos vocês.

Resumo

Esta dissertação apresenta uma investigação da detecção de sistemas de aeronaves não tripuladas (do inglês, *unmanned aircraft systems* (UAS)) usando diferentes abordagens. Primeiro, a viabilidade de detectar um drone DJI Phantom IV com um radar pulsado operando na banda X é investigada por meio de simulações e medições de campo. Em segundo lugar, análises estatísticas e modelagem de vários conjuntos de dados da seção reta radar (do inglês, *radar cross-section* (RCS)) são realizadas. Os conjuntos de dados de RCS são gerados por simulações e também obtidos por medições, para diferentes frequências e ângulos de elevação. A modelagem dos conjuntos de dados de RCS é realizada com base em três critérios: Log-Likelihood, critério de informação de Akaike e critério de informação bayesiano. Além disso, a influência dessa modelagem no alcance de detecção do radar é analisada. Os resultados numéricos mostram que o radar pulsado na banda X pode detectar o drone DJI Phantom IV até uma distância de 425 m e que a RCS de diferentes UASs é predominantemente modelado por variáveis aleatórias do tipo Exponenciais ou Pareto Generalizada, dependendo da frequência e do ângulo de elevação. A modelagem da RCS pode melhorar o desempenho de detecção do radar, reduzindo a perda de flutuação e aumentando a probabilidade de detecção. Assim, esta dissertação contribui para o desenvolvimento de técnicas eficazes para detectar UASs usando sistemas de radar.

Palavras-chave: Drone, Radar, Detecção, RCS, Modelagem.

Abstract

This thesis presents an investigation of the radar detection of unmanned aircraft systems (UASs) using different approaches. First, the feasibility of detecting a DJI Phantom IV drone with a pulsed radar operating in the X-band is investigated through simulations and field measurements. Second, statistical analysis and modeling of various datasets of the radar cross-section (RCS) are performed. RCS datasets are generated by simulations and also obtained by measurements, for different frequency tones and elevation angles. The modeling of RCS datasets is realized based on three criteria: Log-likelihood, Akaike information criterion, and Bayesian information criterion. Also, the influence of this modeling on the radar detection range is analyzed. Numerical results show that the X-band pulsed radar may detect the DJI Phantom IV drone up to a distance of 425 m and that the RCS of distinct UASs is predominantly modeled by Exponential or Generalized Pareto random variables, depending on the frequency tone and the elevation angle. The RCS modeling can improve the radar detection performance by reducing the fluctuation loss and increasing the detection probability. Thus, this thesis contributes to the development of effective techniques for detecting UASs using radar systems.

Keywords: UAS, Radar, Detection, RCS, Modeling.

List of Figures

List of Tables

List of Acronyms

RCS	*radar cross-section*
UAS	*Unmmaned Aircraft System*
DRONEII	Drone Industry Insigths
FAA	Federal Aviation Administration
ANAC	Agência Nacional de Aviação Civil
VLOS	visual line of sight
BVLOS	beyond visual line of sight
LLK	Log-Likelihood
AIC	Akaike Information Criterion
BIC	Bayesian Informtion Criterion
MLE	Maximum Likelihood Estimation
RF	radio-frequency
RL-GO	Ray Launching Geometrical Optics
AREPS	Advanced Refractive Effects Prediction System
UFF	Universidade Federal Fluminense
IEEE	Institute of Electronic and Electrical Engineering
CW	continuous wave
PRF	pulse repetition frequency
PL	pulse length
PRT	pulse repetition time
FM	frequency modulation
FMCW	frequency-modulated continuous wave
NF	noise figure
SNR	signal-to-noise ratio

ITU International Telecommunication Union

PDF probability density function

IMO International Maritime Organization

IEC International Electrotechnical Commission

SRF sweep repetition frequency

VNA Vector Network Analyzer

CDF cumulative distribution function

Contents

Chapter 1

Introduction

Nowadays, the world is experiencing an increase in the popularity and quantity of drones. According to Drone Industry Insigths (DRONEII) company, a leader in drone market research, in 2023 it was recorded a global total of 7.6 million drone flight hours in two operations types: visual line of sight (VLOS) and beyond visual line of sight (BVLOS) [1]. Figure 1.1 shows a visual representation of the number of flight hours of drones by country, where a larger circle circumference indicates higher flight hours. It is possible to note that the VLOS operation is more common than the BVLOS one. In addition, China is the leader in drone use for both types of operations, followed by the USA. In Brazil, drone use is slightly lower than in Canada and only higher than in South Korea.

Yet, according to Federal Aviation Administration (FAA), the agency responsible for controlling and regulating North American's civil airspace, in its last Fiscal Year report, by the end of 2022 had about 1.69 million registered recreational drone units and about 727 thousand registered commercial drone units on the territory of the United States [2]. In Brazil, although drone units are far less than that, there was a significant increase in the number of registered drones. According to data available on the Agência Nacional de Aviação Civil (ANAC) website [3], from June 2017 to May 2022 the number of registered commercial and recreational drones increased from approximately $30,000$ units to over $90,000$ units, as can be observed in Figure 1.2.

Although the term drone is often used by the media and society, *Unmmaned Aircraft System* (UAS) is a more acceptable term by the academic community [4]. These aircraft can be used in a wide variety of useful applications, such as entertainment (e.g., photography, cinematography [5]), commerce (e.g., delivery of products [6], last-mile delivery [7]), security (e.g., factory security [8], police drones [9]) and even in healthcare (e.g., organ delivery [10]). However, UASs can also be aimed at negative goals, including terrorism

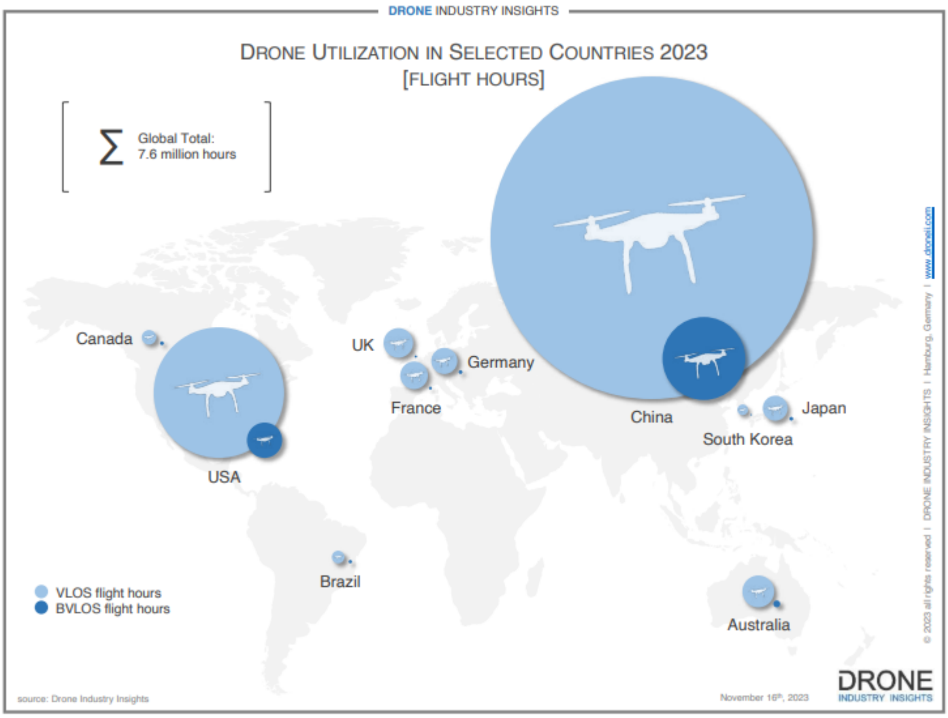

Figure 1.1: Flight hours in VLOS and BVLOS operations by country [1].

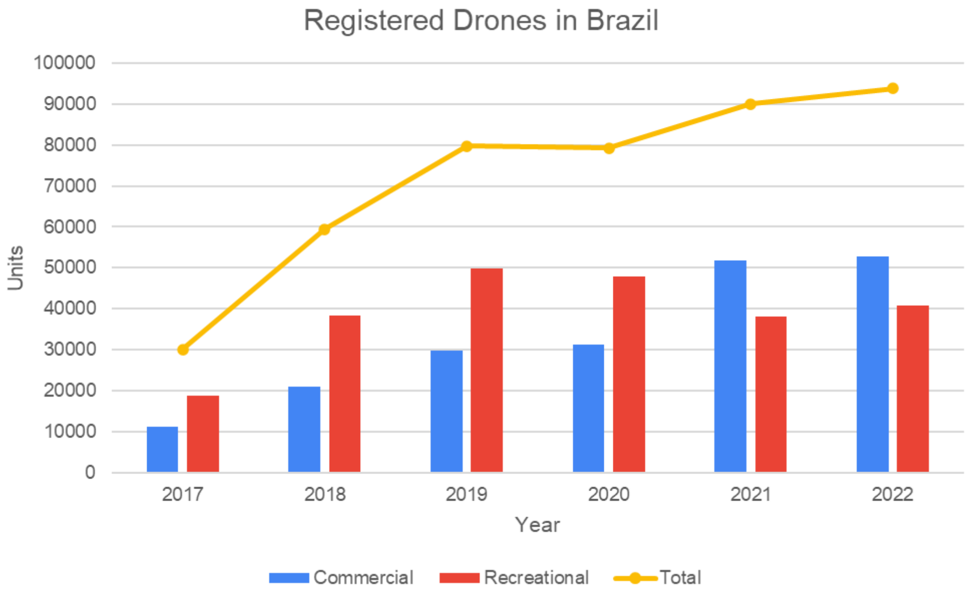

Figure 1.2: Registered commercial and recreational drones in Brazilian territory.

[11], drug trafficking [12], and espionage [13]. Therefore, it is necessary to find ways of counteracting the aforementioned threats caused by the widespread of UASs.

With the aim of safeguarding the privacy and security of individuals and organizations, the increasing prevalence of drones has spurred the development of techniques for detecting, classifying, and identifying drones. Detection involves determining whether a drone is present in the monitored region. Classification is the determination of the type or category of the detected drone. This could be based on its size, shape, model, or other distinguishing characteristics. Identification is a more specific process that involves determining the exact model of the drone. Identification can provide detailed information about the drone, such as its capabilities, range, payload capacity, and more. Each of these steps plays a crucial role in the overall process of drone monitoring and management and requires different techniques and technologies.

Considering only the drone detection process, there are some techniques that rely on visual methods of detection, using images or videos, while others rely on acoustic detection. There are also techniques that focus on passive detection of radio-frequency (RF) emissions between the operator and the UAS, as well as those that utilize radar for detection. Each of these methods has its own set of advantages and limitations, which are presented in the following.

- **Visual Detection**: this approach uses video cameras [14] [15] or infrared [16] to detect the UAS in a given search volume. However, this detection modality operates unsatisfactorily under unfavorable atmospheric conditions (such as clouds, fog, rain, snow) or limited visibility (such as during the night) [14]. Although high-quality infrared cameras solve some of these problems, their costs are still very high, making research in this area difficult [17]. Additionally, buildings or other constructions can obstruct the line of sight between the camera and the UAS, significantly decreasing its detection ability.

- **Acoustic Detection**: this type of detection involves analyzing the sound emitted by the UAS through sets of microphones [18]. After this analysis, a database can be produced with the specific sound fingerprint of each aircraft and can then be used, also, to identify and classify them [19]. This detection modality works well for short distances of up to 150 m [20]. However, its precision is greatly impaired when detection is carried out in environments with a lot of noise, such as urban areas and airports [21]. Furthermore, some UAS models have noise cancellation techniques that make the use of this approach for detection unfeasible.

- **Passive Detection**: this detection technique exploits the fact that drones have an on-board transceiver to communicate with the operator [22] [23]. In this way, by capturing the electromagnetic signals exchanged between them, it is possible to determine where the UAS is located and even the location of its operator [24]. However, this solution fails when the drone is operated autonomously [25]. In these cases, the drone generally flies using preprogrammed GPS reference points, and its communication with the operator is limited [19].

- **Radar Detection**: this approach consists of using active radars that emit electromagnetic waves and capture the reflected signals, determining the presence of targets based on the energy reflected by them [26]. Unlike visual detection, these radars are effective even in adverse atmospheric conditions. Furthermore, since its principle is not based on mechanical waves, the radars are immune to sound noise, unlike acoustic detection. Moreover, they do not require communication between the drone and the operator for detection, as passive detection requires. However, radars are extremely dependent on the *radar cross-section* (RCS) of targets, typically represented as the effective area that intercepts the transmitted radar power and scatters it back to the radar receiver, which in the case of UAS can be minimal [27]. Furthermore, depending on the operating frequency, radars can have a high path loss due to atmospheric attenuation, limiting their detection range [28].

Radar stands as a pivotal device in the realm of detection systems due to its dual capability of detecting the presence of a target and also measuring its range with high precision. No other method can compete with radar in terms of its resilience to weather variations and its long-range measurement capacity [26]. Therefore, the role of radar as a detection and range measurement tool is of paramount importance in various fields, strengthening its position as an unrivaled technique in these aspects.

Thus, as radar detection overcomes the main limitations of the other detection techniques mentioned above, this thesis proposes investigating radar detection in two steps: the first is through the theoretical employ of the radar equation to determine whether it is possible or not to detect a usual commercial drone with an X-band pulsed radar by means of simulation and field measurement. In that manner, it is possible to analyze the aspects of radar detection of a target that lies at the edge of two scatter regions due to its body size and the wavelength of the X-band signal. The second step is to evaluate the impact, in the radar range, treating RCS as a constant or as a random variable. In addition, the possibility of modeling the RCS according to the usual random variables is evaluated.

1.1 Objectives

The following objectives are meant to be achieved in this thesis:

- To explore the viability of detecting a DJI Phantom IV drone utilizing an X-band pulsed radar, employing a two-fold methodology encompassing simulations and field measurements. Starting with Feko software simulations to determine the RCS value specific to the Phantom IV, this thesis introduces two distinct methods, facilitated by Matlab software, for analyzing the radar equation and deriving the system loss parameter. Furthermore, the military software AREPS is employed, and its results are meticulously compared with the Matlab-based methods. This iterative process enhances the robustness of the assessment. Culminating in on-site field measurements, where the X-band pulsed radar is deployed alongside the DJI Phantom IV. This investigative process entails a comprehensive examination of the detection capabilities of an X-band pulsed radar system when faced with the specific characteristics of a commercial drone. By integrating advanced simulations and conducting real-world field measurements, it is expected to assess the feasibility and efficacy of employing X-band pulsed radar for the detection of the DJI Phantom IV. This dual approach, combining advanced simulations with real-world assessments, provides a holistic understanding of X-band pulsed radar's performance, contributing valuable insights into the practical aspects of drone detection in diverse and dynamic real-world scenarios.

- To perform statistical analysis specifically targeting multiple datasets of RCS acquired from different UASs. The complexity of this task requires a multifaceted approach that incorporates the utilization of probability density functions, cumulative distribution functions, and the generation of histograms for each unique RCS dataset. By employing these advanced analytical techniques, it is expected to gain a profound understanding of the inherent variability within the RCS datasets, facilitating more robust and accurate modeling. This intricate process involves not only extracting valuable insights from individual datasets, but also establishing connections and patterns across various UASs.

- To determine the optimal random variable for modeling the RCS dataset. This selection process involves evaluating probability distributions against the histogram of the RCS data using three distinct criteria: Log-Likelihood (LLK), Akaike Information Criterion (AIC), and Bayesian Informtion Criterion (BIC). The aim is to identify probability distributions that closely align with the empirical distribution of the RCS data, employing a nuanced approach that considers statistical measures such as LLK, AIC, and BIC. This meticulous analysis enables the determination of the most suitable random variable, contributing to a refined and accurate representation of the underlying probability distribution that governs the RCS dataset.

- To assess the impact of RCS modeling on both radar detection range and overall detection performance. This evaluative process involves a comprehensive examination that uses the radar range equation and incorporates the parameters intrinsic to a real-world radar system. By leveraging the radar range equation and the relevant system parameters, it is expected to gauge how RCS modeling influences not only the reach of radar detection but also its overall effectiveness. This analytical approach provides insights into the intricate interplay between RCS modeling and the essential components of radar systems, shedding light on the nuanced factors that contribute to the radar's detection capabilities and performance.

1.2 Thesis outline

The remainder of this document is organized as follows:

- Chapter 2 introduces the basics of radar detection, such as the radar system, the radar equation, the radar cross-section, and the effects of the atmosphere on the electromagnetic waves. It also presents the classification of radars according to their frequency bands, their ability to measure the Doppler effect, and the waveform of their transmitted signal.

- Chapter 3 investigates the use of the FAR-2117 X-band pulsed radar to detect the DJI Phantom IV drone. Initially, it presents the formulation of the problem when using this kind of radar to detect drones. In addition, it discusses two methods of analysis employing the radar range equation. For this, radar cross-section, radar range, and detection probability simulations are introduced. Subsequently, field measurements were made to validate the results obtained by the simulations.

- Chapter 4 discusses the statistical analysis and modeling of the RCS of a DJI Phantom IV drone and of a database composed of 9 different UASs [29]. For the Phantom IV drone, the RCS datasets are generated through simulations for distinct frequencies and elevation angles, while in the UASs dataset the RCS were measured in an anechoic chamber. In addition, the impacts of RCS modeling on the radar detection range are analyzed.

- Chapter 5 states the concluding remarks of this thesis, revisiting the main points discussed, highlighting the main contributions, and establishing future work.

Chapter 2

Radar Detection

This chapter presents a brief history of the origin of the radar system and its definition. Also presents its classification regarding the operating frequency bands, the ability to measure the Doppler effect, and the transmitted signal's waveform. Furthermore, the radar equation for pulsed and frequency-modulated continuous wave (FMCW) radar systems and relevant parameters that affect the radar detection are discussed.

2.1 Radar System

The term radar is an acronym for ***Ra****dio* ***D****etection* ***A****nd* ***R****anging*. Radar is a system that emits electromagnetic waves and captures the reflected signals, also called echo radar, determining the presence, distance, and speed of targets based on the energy reflected by them. This system was one of the main scientific discoveries during World War II, which helped change the course of this war and thus shape the modern society [30].

The first step towards the development of radar began in 1886 by the German physicist Heinrich Hertz. Using an equipment that emitted pulses at a frequency close to 455 MHz, Hertz demonstrated that radio waves could be reflected in metallic objects [31]. Then, in 1904, another German engineer, Christian Hülsmeyer, created a device that could detect ships from a distance using radio waves, but at that time it had neither commercial nor military success [32].

It was only in the 1930s that radar began to be used for military purposes, mainly during World War II. British Robert Watson-Watt was the pioneer in creating a practical and effective radar system, which allowed the British to detect German planes that were bombing the country. This system became known as *Chain Home* [33]. Radar was fundamental to the Allied victory in the Battle of Britain and on other fronts of the war [30].

Since then, radar systems have continued to be improved and applied in various civil and military areas, being used to control air traffic, predict the weather, navigate at sea and in the air, defend against ballistic missiles, explore space and, recently, to help guide autonomous cars. In general, the main functions of a radar system are [34]:

- **Search**: also called surveillance, this function involves searching for possible targets of interest in a given volume of space.
- **Detection**: radar detection is the determination that a target is present in the search volume. This is usually done by setting a received signal threshold that excludes most noise and other interfering signals, if the reflected signal exceeds a given threshold the target is detected.
- **Measurement**: based on the reflection of the target's signal, the radar system can calculate the distance and direction, in angular coordinates, of its position.
- **Tracking**: radar tracking is the determination of the path of a moving target from a series of consecutive position measurements.
- **Estimation of target characteristics**: a radar system can estimate other attributes of the target to better characterize or identify it. These estimations may include RCS, fluctuations of RCS with time, target size, target shape, and target motion characteristics by means of the Doppler effect.

Basically, radars are classified according to their operating frequency band, their ability to measure the *Doppler* effect, and the transmitted signal's waveform. These classifications are discussed in the following subsections.

2.1.1 Frequency Bands

Because radars were widely used during World War II, their frequency bands used letter codes to distinguish each other. Although, initially, this code was used to maintain the military secrecy of operations, over time, they continued to be used and accepted by the scientific community, even being approved as a standard by Institute of Electronic and Electrical Engineering (IEEE) [35] and as a recommendation by International Telecommunication Union (ITU)-R [36]. Table 2.1 shows the frequency bands, as well as the corresponding designation of the IEEE Standard — adopted in this thesis — and ITU-R Recommendation.

Table 2.1: Letters designations for radar system frequency bands in IEEE and ITU.

Frequency bands	IEEE standard	ITU-R recommendation
3-30 MHz	HF	HF
30-300 MHz	VHF	VHF
0.3-1 GHz	UHF	UHF (0.3-3 GHz)
1-2 GHz	L	
2-4 GHz	S	
4-8 GHz	C	SHF (3-30 GHz)
8-12 GHz	X	
12-18 GHz	Ku	
18-27 GHz	K	
27-40 GHz	Ka	
40-75 GHz	V	EHF (30-300 GHz)
75-110 GHz	W	
110-300 GHz	mm	

Most research related to radar detection of UAS has focused on radar systems operating in L-band (1-2 GHz) [37], S-band (2-4 GHz) [38], X-band (8-12 GHz) [39], Ku-band (12-18 GHz) [40], K-band (18-27 GHz) [41], and Ka-band (27-40 GHz) [42].

2.1.2 Doppler Effect

The Doppler effect is a physical phenomenon described by a change in the measured frequency of a mechanical or electromagnetic wave in relation to an observer who is moving relative to the source of the wave. This effect was discovered by Austrian physicist Christian Doppler in 1842 and has several applications in science and technology.

Radar systems with the ability to measure the Doppler effect are *coherent*, while its counterpart is *incoherent*. A coherent radar system is capable of maintaining a constant phase relationship between transmitted and received signals, allowing detection of the Doppler effect and, consequently, measurement of a target's speed [43]. Yet, there are those radar systems that measure the *micro-Doppler* effect and can also obtain a specific signature of a target, such as, for example, the rotation speed of the propellers of an UAS

[44]. Doppler shift in radar systems is given by [45]

$$f_{msd} = f_{trm}\left(\frac{c \pm v_{rdr}}{c \pm v_{tgt}\cos\beta}\right) = f_{trm}\left(\frac{1 \pm \dfrac{v_{rdr}}{c}}{1 \pm \dfrac{v_{tgt}\cos\beta}{c}}\right), \tag{2.1}$$

in which f_{msd} and f_{trm} are, respectively, the frequency of the measured signal by the radar receiver side and the frequency of the transmitted signal by the radar transmitter side, both in Hertz; $c \approx 3 \times 10^8$ meters per second represents the speed of light, while v_{rdr} and v_{tgt} are, respectively, the magnitudes of the radar system's speed and the target's speed, both in meters per second. Also, β is the angle between the target speed's vector and a vector pointing to the target with the origin in the radar.

Figure 2.1 shows an illustration of the Doppler Effect in a radar system with the given parameters. For a coherent radar system, f_{msd} and f_{trm} are known. Also, in some cases, the radar is not moving linearly ($v_{rdr} = 0$) and β can be determined by the angular position of the radar's antenna and the direction of movement of the target. Therefore, the remaining term, v_{tgt}, can be calculated through the knowledge of the other parameters.

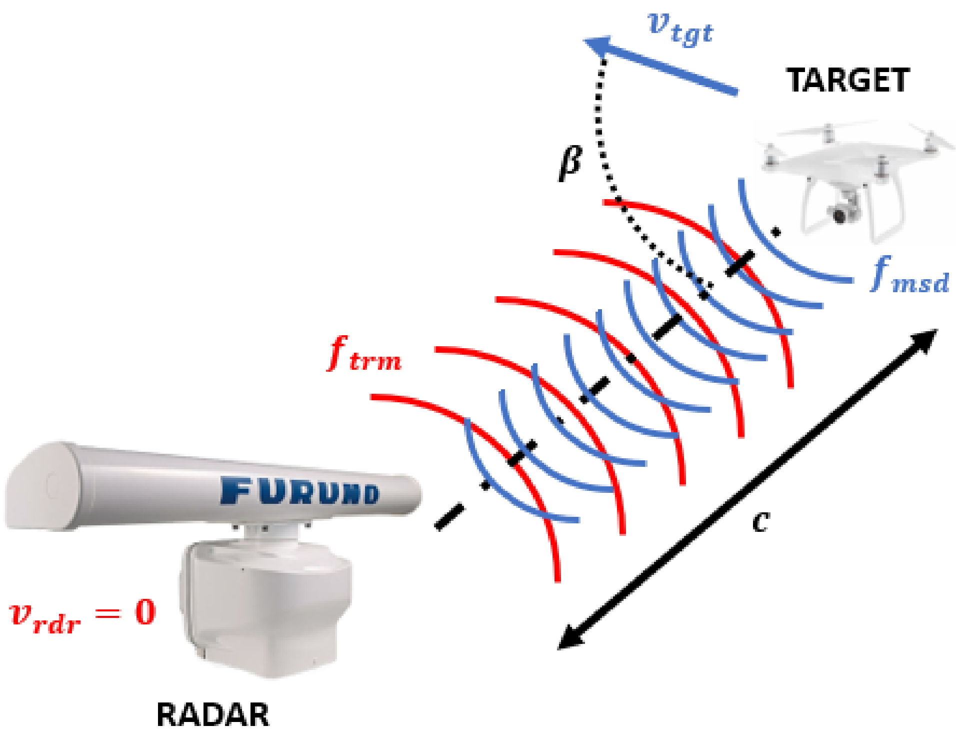

Figure 2.1: Illustration of the Doppler Effect in a radar system.

2.1.3 Transmitted Signal's Waveform

Regarding the transmitted signal, radar systems are classified into two main groups: pulsed radars and continuous wave (CW) radars [46]. Pulsed radar emits intermittent bursts of radio frequency energy, allowing for precise range measurements and effective clutter rejection. In contrast, CW radar continuously emits a waveform, making it well-suited for continuous tracking and exploiting the Doppler effect for velocity measurements. Furthermore, while pulsed radars use a single antenna for transmission and reception, CW radars require two separate antennas for simultaneous transmission and reception [26]. In addition to these types of radars, not presented in this thesis, there are techniques that aim to improve these systems, such as pulse compression radar, which basically combines a continuous wave modulated in frequency with the pulses of a pulsed radar, aiming to improve the resolution and signal-to-noise ratio of the radar. However, each of them has unique characteristics with respect to power consumption, clutter rejection, complexity, costs, and applications.

In terms of power consumption, pulsed radar systems often demand higher power levels during the transmission phase due to the intense energy required to generate short pulses. On the other hand, CW radar systems maintain a more consistent power demand as they emit a continuous waveform without interruptions. Clutter rejection is another distinguishing factor, with pulsed radars excelling in cluttered environments because of their intermittent nature, allowing for improved discrimination between signals and unwanted echoes. CW radar systems may face challenges in cluttered environments, as their continuous transmission lacks distinct time intervals between pulses for effective clutter rejection [47]. Considering their complexity and costs, pulsed radar systems tend to be more complex and expensive, especially in applications that require advanced signal processing techniques for target discrimination and tracking. CW radar, with its simpler design, is often more cost-effective, making it suitable for applications that prioritize continuous tracking and basic Doppler velocity measurements [47]. Pulsed radar systems are commonly employed in applications where high precision, accurate range measurements, and clutter rejection are critical, such as in air traffic control, military tracking, and surveillance. On the other hand, CW radar systems are suitable for tasks that require continuous tracking and basic Doppler velocity measurements, including police speed guns, weather monitoring, and certain aerospace applications. The choice between pulsed and CW radars depends on the specific requirements of the application, with designers weighing the advantages and limitations of each technology [26].

2.1.3.1 Pulsed Radar System

Pulsed radars operate with short-duration signals that are transmitted and received by a single antenna. Figure 2.2 illustrates the transmitted signal from a pulsed radar system along with its main operating parameters. During the pulse transmission interval, i.e., the pulse length (PL), the radar system blocks the reception channel to avoid receiving high power due to this transmission. After this interval and before the next pulse transmission, the radar system waits for the reflected signals from the target. The time between each transmitted pulse, T_p, is called pulse repetition time (PRT), given in seconds, with $T_p = f_p^{-1}$, in which f_p is the pulse repetition frequency (PRF), i.e., is the frequency at which the pulses are transmitted, given in Hertz. The bandwidth of the transmitter, B_W^{TX}, is referenced as inversely proportional to the pulse length, and the bandwidth of the receiver, B_W^{RX}, is kept constant in the radar design, in general, $B_W^{RX} > B_W^{TX}$.

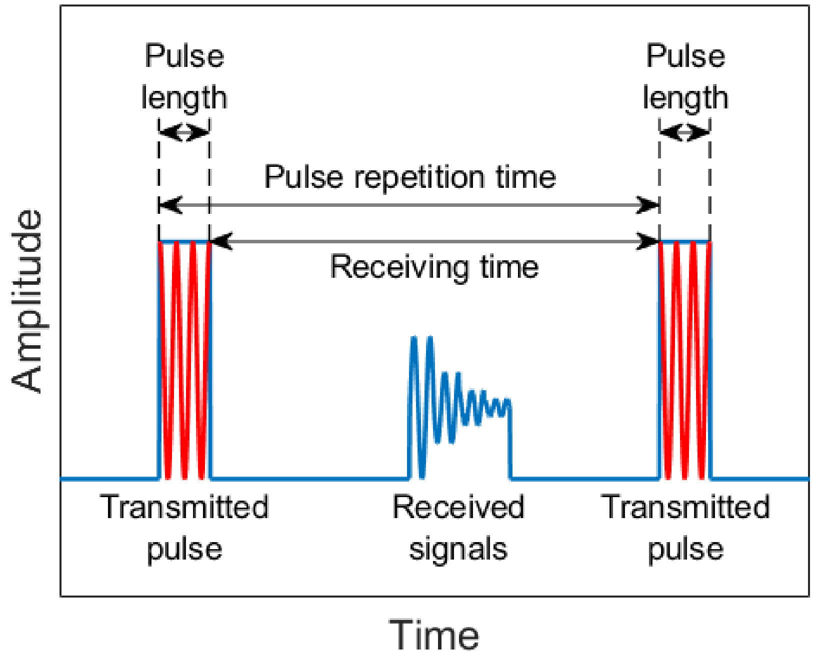

Figure 2.2: Transmitted and received signals of a pulsed radar system. The red line refers to the signal in the operating frequency of the radar.

To calculate the distance to a target, the radar system measures the time interval that a single transmitted pulse takes to travel from the radar to the target and vice-versa. This is called round-trip time of the signal. Considering that electromagnetic waves travels, in free space, at the speed of light, then, the distance to a target is given by

$$R = \frac{c\Delta t}{2}, \tag{2.2}$$

in which Δt is the round-trip time of the signal in seconds.

Another important parameter of a pulsed radar system is its Maximum Unambiguous Range, which is defined as the greatest distance at which a transmitted radar pulse can travel and return between consecutive pulses and still produce reliable information [26]. Observe that if $\Delta t < T_p$, the return signal arrives before the next pulse is transmitted. If $\Delta t = T_p$, the reflected signal arrives exactly when the next pulse is transmitted. If $\Delta t > T_p$, the reflected signal arrives after the next pulse is emitted and there is an ambiguity, i.e., the radar cannot tell whether the reflected signal came from the first or the second pulse.

Therefore, the maximum unambiguous range is the distance at which $\Delta t < T_p$ and it is given by

$$R_{un} = \frac{cT_p}{2} = \frac{c}{2f_p}. \tag{2.3}$$

2.1.3.2 CW Radar System

CW radar systems continuously and simultaneously transmit and receive the echoes reflected by the targets and, therefore, require an antenna for transmission and another for reception. The speed and trajectory of a moving target can be determined by observing frequency changes on the radar receiver side due to the Doppler effect. Purely CW radar systems cannot perform range measurements without some additional modulation, such as frequency modulation (FM). CW radars that use FM are called FMCW radars. Figure 2.3 shows the variation of the amplitude over time of transmitted and reflected signals of an up-chirp FMCW radar system. Note that the reflected signal has the same waveform as the transmitted signal but is delayed by the round-trip time, Δt.

Thus, to calculate Δt, (2.2) can be rewritten as

$$\Delta t = \frac{2R}{c}. \tag{2.4}$$

The main characteristic of an FMCW signal is its *chirp*, which is defined as a signal that increases linearly in frequency over time. Each chirp signal has a defined time interval of duration (also known as sweep repetition time, T_s), bandwidth (B_w), and sweep repetition frequency (SRF) (f_s). The latter refers to the frequency at which the entire chirp is repeated and is given by the relation $f_s = 1/T_s$ [48].

Figure 2.4 shows a graph of the FMCW transmitted and reflected signal's frequency

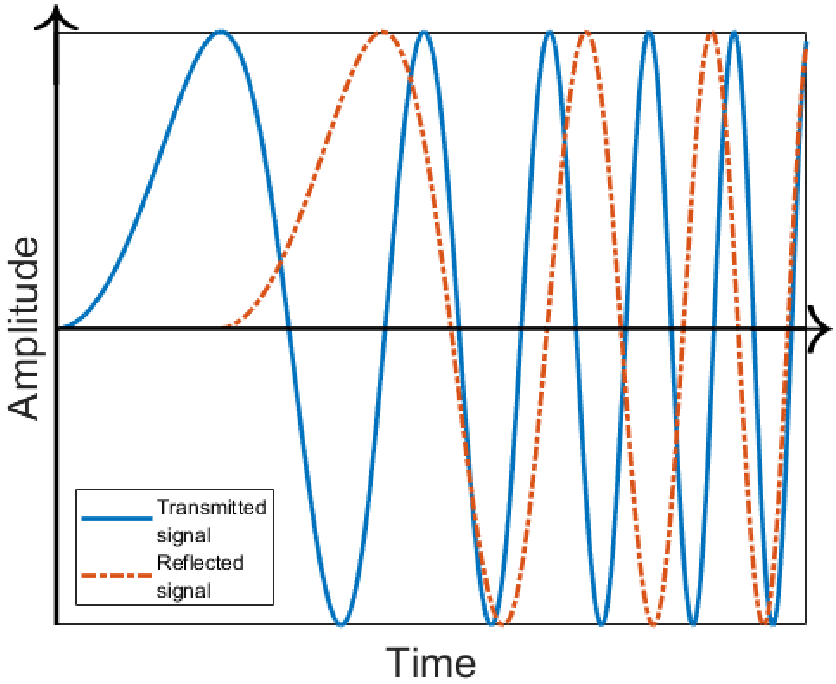

Figure 2.3: Transmitted and reflected signals of a FMCW radar system in amplitude over time.

variation over time, in which Δf is the frequency variation between the transmitted and reflected signal, T_s is the *chirp* interval, f_0 is the initial frequency, B_W^{TX} is the bandwidth at the transmitter, and f_D is the frequency shift observed by the radar system.

Observing the Figure 2.4, it is possible to notice that there is a difference Δf between the transmitted and the reflected signals. The measurement of this difference by the radar system led to the delayed time, Δt of the reflected signal and, consequently, to the calculation of the target distance R by (2.4), in every transmission (or *chirp*) period T_s, in which the frequency f_0 is varied up to $f_0 + B_W^{TX}$. Furthermore, when the signal is measured over several chirp periods, the Doppler effect allows one to observe a frequency shift f_D for a target approaching or moving away from the radar. Thus, the target's speed can be measured by (2.1).

2.2 Radar Equation

The radar equation is a mathematical expression that describes the relationship between the radar range and the parameters of the transmitter and receiver sides of the radar system, the target, and the surrounding environment. It is a valuable tool for estimating the maximum distance at which a radar can detect a target, as well as for analyzing

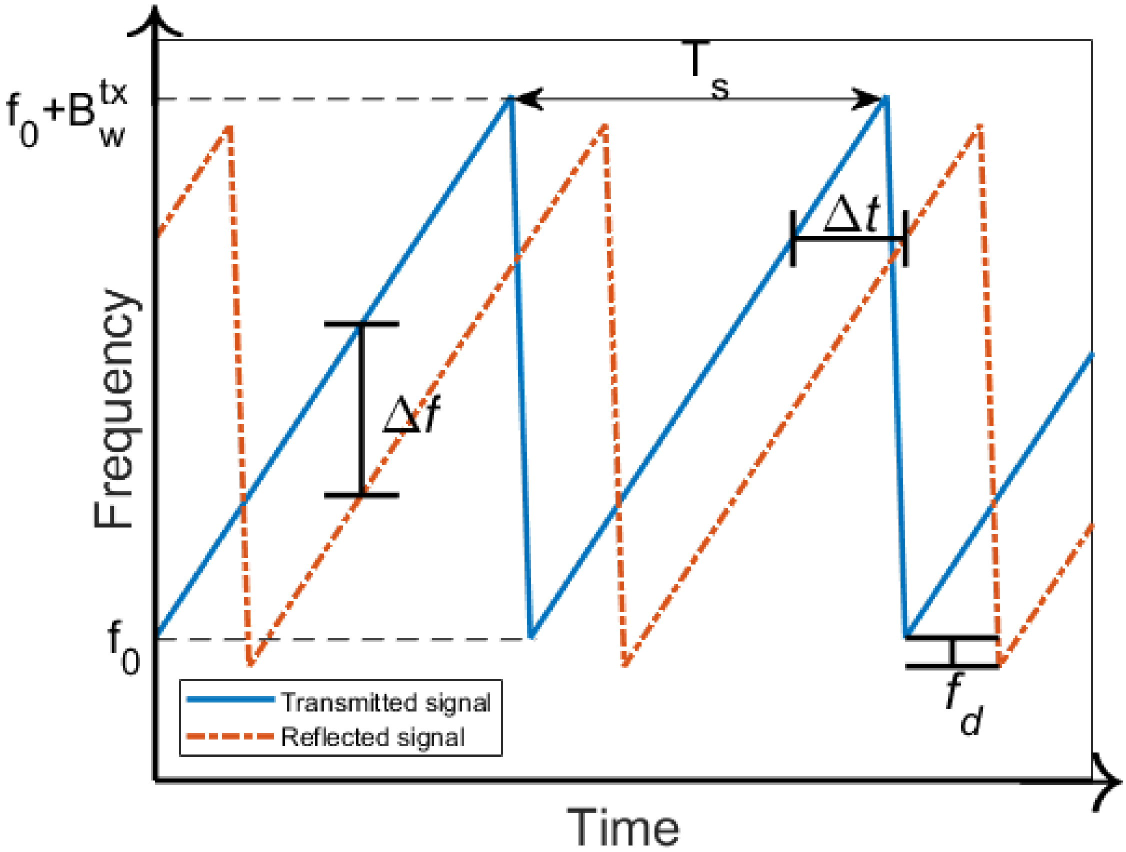

Figure 2.4: Transmitted and reflected signals from a FMCW radar system in frequency over time.

the factors that influence radar performance. Moreover, it is an essential instrument for assisting in radar system design [26].

In the radar equation's simplest form, the maximum radar range is given by [43]

$$R_{\max}^4 = \frac{P_t G_t G_r \lambda^2 \sigma}{(4\pi)^3 S_{min}}, \tag{2.5}$$

in which P_t is the transmitted power in Watts, G_t and G_r are, respectively, the gains of the transmitting and receiving antennas (for a pulsed radar system, $G_t = G_r = G$). Also, λ is the wavelength of the transmitted signal in meters, σ is the target's RCS in square meters, and S_{min} is the minimum detectable signal power by the radar, given in Watts. Note that, except for σ, all other parameters are intrinsic to the radar system.

However, (2.5) does not provide an adequate prediction of the maximum radar range, since there are some external factors that affect its performance, such as:

- The statistical nature of the minimum detectable signal;

- Fluctuations and uncertainties in the RCS of targets;
- System-related losses;
- Effects of electromagnetic wave propagation in the atmosphere.

As mentioned before, both S_{min} and σ are subject to random variations, and, thus, uncertainty is introduced in the radar range. In this regard, the radar equation becomes a function of the detection probability (P_d) and the false alarm probability (P_{fa}). P_d is the probability of detecting a target when there really is one, while P_{fa} is the probability of detecting when there is no target present. In the following, each external factor that affects the performance of a radar systems is discussed. First, it is presented for the case of a pulsed radar system, then, at last, the radar equation is modified for the case of a FMCW radar system.

2.2.1 Signal Detection in Noise

The radar's ability to detect a target is influenced by the minimum signal strength, S_{min}, that allows the reflected signal to be discerned from noise. To occur the radar detection, a decision threshold is established in the equipment's receiver, so that a value above this threshold represents the echo of a target and values below this threshold represent some unwanted noise. However, there may be cases in which a radar echo, originating from a target actually present, has a level lower than the established threshold and, therefore, it is not detected.

Figure 2.5 illustrates a signal reflected with noise by a radar system as a function of time, as well as some established thresholds. In this figure, the noise amplitude (blue line) may result in false detection. Note that, considering the Threshold 1 (black dash line), the target signal (red line) which has the higher amplitude will be detected by the radar, but the lower target signal will not. Now, considering the Threshold 2 (yellow dash line), note that both the higher target signal and noise signal will be indicated by the radar as two distinct targets, increasing the false alarm occurrence. Although the threshold can be changed, it must be considered that reducing its value may result in a greater probability of detecting false alarms, for example when the Threshold 3 (green dash line) is selected.

Although used in (2.5), the parameter S_{min} is not the best one to analyze the performance of a radar system, it is preferable to use the signal-to-noise ratio (SNR) S/N which, basically, measures how much the detectable signal's power is greater or lower than

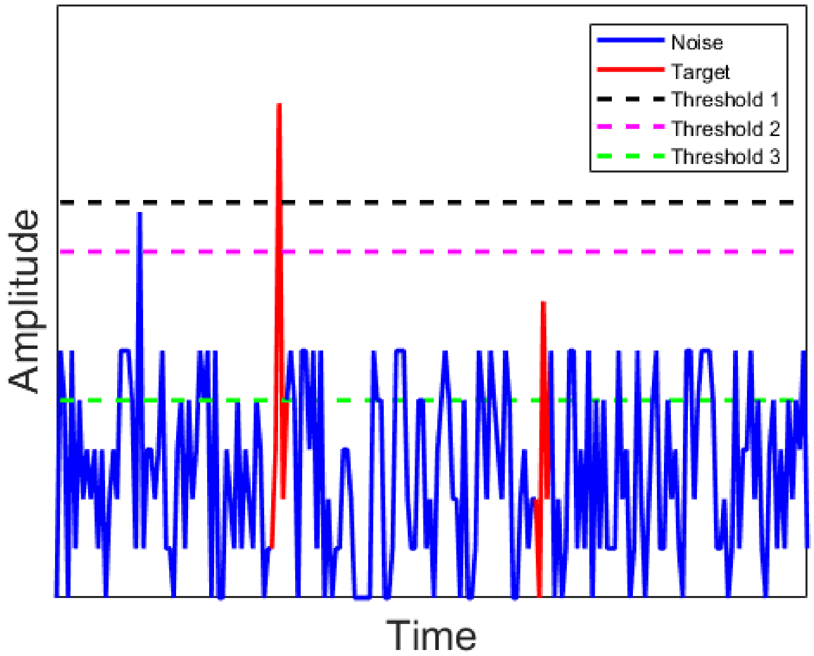

Figure 2.5: Thresholds candidates and signals received by a radar system.

the noise's power. To find the relation between S_{min} and S/N, consider that the noise's power at the radar receiver is given by

$$N_i = kT_0B_W^{RX}F, \tag{2.6}$$

in which k is the Boltzmann constant ($1,38.10^{-23}$ J/K), T_0 is the standard noise temperature (290 K), and F is the noise figure (NF). NF is a measure that indicates the degradation of the signal caused by noise in a radar system. It is calculated as the ratio between the input SNR, S_i/N_i, and the output SNR, S_0/N_0, of the device [43] and it is given by

$$F = \frac{S_i/N_i}{S_0/N_0}. \tag{2.7}$$

Replacing the (2.6) into (2.7) and rearranging, then

$$S_i = kT_0BWF\left(\frac{S_0}{N_0}\right). \tag{2.8}$$

If $S_i = S_{min}$, then $\left(\frac{S_0}{N_0}\right) = \left(\frac{S_0}{N_0}\right)_{min}$, thus, (2.8) results in

$$S_{min} = kT_0BWF\left(\frac{S_0}{N_0}\right)_{min}. \tag{2.9}$$

Replacing (2.9) into (2.5), considering $G_t = G_r = G$, and omitting subscripts in S/N terms, then

$$R^4_{\max} = \frac{P_t G^2 \lambda^2 \sigma}{(4\pi)^3 k T_0 B_W^{RX} F (S/N)}. \tag{2.10}$$

The advantage of using (S/N) instead of S_{min} is that its value can be expressed as a function of P_d and P_{fa}. The relationship between (S/N), in dB, when only one pulse is received, P_d and P_{fa} for an accuracy of 0.2 dB considering $10^{-7} \leq P_{fa} \leq 10^{-3}$ and $0.1 \leq P_d \leq 0.9$ is given by [49]

$$(S/N)_1 = 10 \log (A + 0.12AB + 1.7B), \tag{2.11}$$

in which $A = \ln (0.62/P_{fa})$ and $B = \ln [P_d/(1 - P_d)]$. Figure 2.6 shows the SNR, (S/N), required for a given P_d and P_{fa}. This relationship applies to a single receive pulse. Note that, as P_d and P_{fa} are parameters determined in the design of a radar system, then, with those values, it is possible to obtain the value of required $(S/N)_1$ through the graph. For example, considering a radar system design which requires $P_d = 0.8$ and $P_{fa} = 10^{-3}$, then the required $(S/N)_1$, for a single pulse, is about 10 dB.

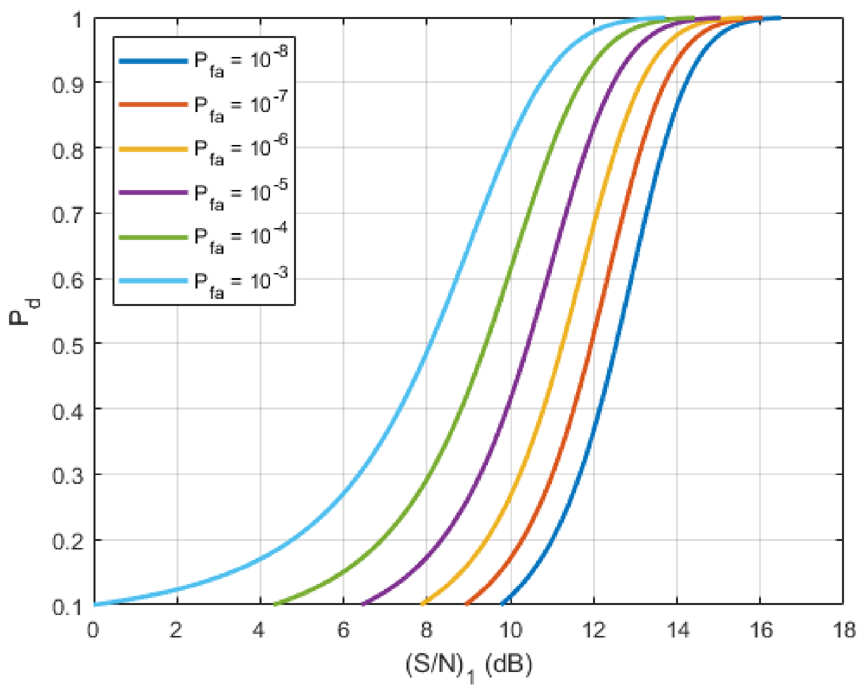

Figure 2.6: Relation between $(S/N)_1$ and P_d for some P_{fa} values.

A pulsed radar often emits and receives several pulses, called a pulse train. The number of pulses, n, received by the radar is given by [26]

$$n = \frac{\theta_{bh} f_p}{6\omega_r}, \tag{2.12}$$

in which θ_{bh} is the horizontal beamwidth in degrees, f_p is the radar PRF in Hertz, and ω_r is the antenna rotation speed in rotations-per-minute. Thus, an approximation for S/N, in dB, when n pulses are received is given by [26]

$$(S/N)_n = -5\log(n) + \left(6,2 + \frac{4,54}{\sqrt{n+0,44}}\right)\log(A + 0.12AB + 1.7B), \tag{2.13}$$

in which A and B are the same as in (2.11). (2.13) has an error of less than 0.2 dB for $1 \leq n \leq 8096$, considering $10^{-7} \leq P_{fa} \leq 10^{-3}$ and $0.1 \leq P_d \leq 0.9$. Figure 2.7 shows the relation between $(S/N)_n$ and P_d for some P_{fa} values, considering different values of n.

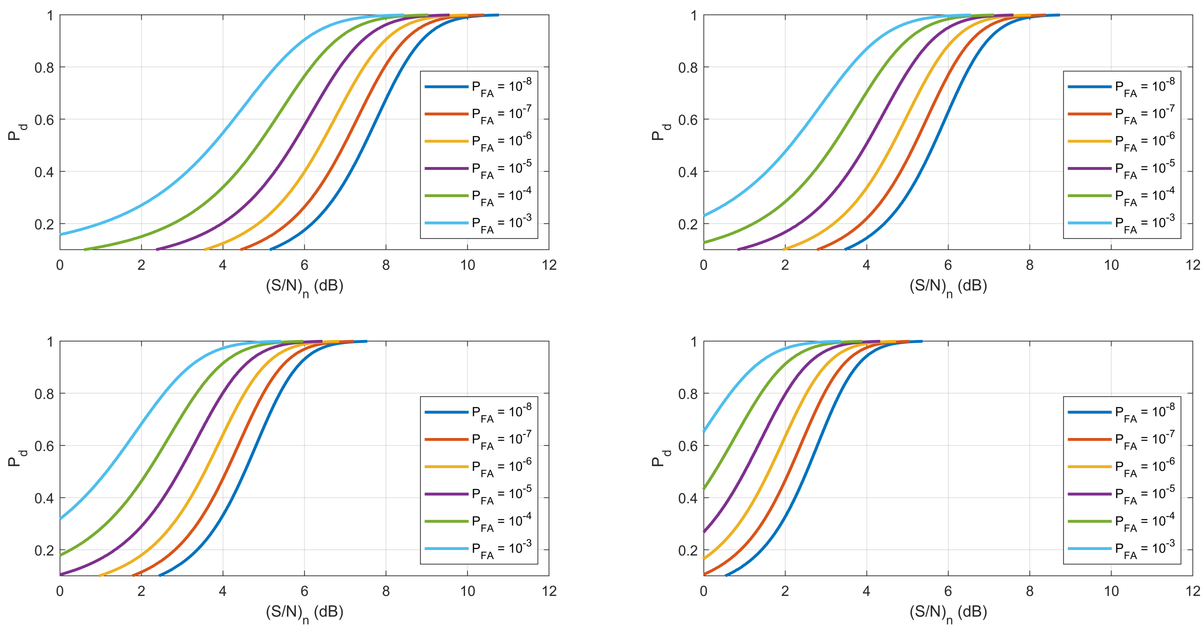

Figure 2.7: Relation between $(S/N)_n$ and P_d for some P_{fa} values, considering, from left to right and from top to bottom, $n = 3, n = 7, n = 10, n = 20$.

Comparing the Figures 2.6 and 2.7, it is possible to observe a decrease in the required SNR for the same P_d and P_{fa}. For example, in Figure 2.7, for $P_d = 0.8$ and $P_{fa} = 10^{-3}$, the required $(S/N)_n$ is about 6.2 dB for $n = 3$, 3.6 dB for $n = 7$, 2.5 dB for $n = 10$, and 0.6 dB for $n = 20$, unlike the 10 dB found in Figure 2.6 for $n = 1$. Thus, this process of adding n pulses, called *Pulse Integration*, allows for the detection of targets with weaker signals, which can result in a lower transmission power per pulse.

Pulse integration in radars is a technique that aims to improve target detection by processing multiple received echoes. There are two types of pulse integration: coherent and non-coherent. The difference between them is related to the processing of the pulse phase.

In coherent radar processing, the phase of the transmitted and received pulses is constant and is used to extract additional information about the target, such as its radial velocity (Doppler effect) and its size (angular resolution). This type of processing is used in radars that have transmitters with power amplifiers powered by a stable continuous oscillation, which serves as a phase reference. This type of integration is more complex, but provides accurate Doppler frequency measurements and better target detection [26].

In non-coherent radar processing, the phase of the transmitted and received pulses is random and it is not considered. The amplitudes of echoes received from the same target are added together, thus increasing the signal-to-noise ratio. This type of processing is used in radars that have self-oscillating transmitters, which do not have a stable phase reference. This type of integration is simpler, lower cost, and suitability for certain applications [43].

The advantages of coherent processing over non-coherent processing are: greater sensitivity in target detection, greater ability to discriminate close or overlapping targets, greater ability to measure the radial velocity of targets and greater ability to suppress interference and noise. In both cases, the integration efficiency is given by [26]

$$E_i(n) = \frac{(S/N)_1}{n(S/N)_n}. \tag{2.14}$$

For coherent integration $E_i(n) \approx 1$ and for non-coherent $E_i(n) < 1$. The improvement in the SNR when n pulses are integrated is called the *Integration Factor*, $I_i(n)$, which is given by

$$I_i(n) = nE_i(n). \tag{2.15}$$

Figure 2.8 shows the graphs for $I_i(n)$ as a function of n for some P_d values, considering different values for P_{fa}. Observe that, for the same n and increasing P_{fa}, $I_i(n)$ decreases for the same P_d. Besides, for the same n, $I_i(n)$ is less sensitive to P_{fa} changes, e.g., considering $\Delta I_i(n) = I_{i,P_d=a}(n) - I_{i,P_d=b}(n)$, for $a = 1$, $b = 0.2$, and $P_{fa} = 10^{-6}$, $\Delta I_i(50) = 6.3$, for $P_{fa} = 10^{-3}$, $\Delta I_i(50) = 7.5$, i.e., a variation of 10.000% in P_{fa} produced a variation of, approximately, 19% in $I_i(n)$.

Considering, now, the Pulse Integration, (2.10) can be rewritten as

$$R_{\max}^4 = \frac{P_t G^2 \lambda^2 \sigma}{(4\pi)^3 k T_0 B_W^{RX} F (S/N)_n}. \tag{2.16}$$

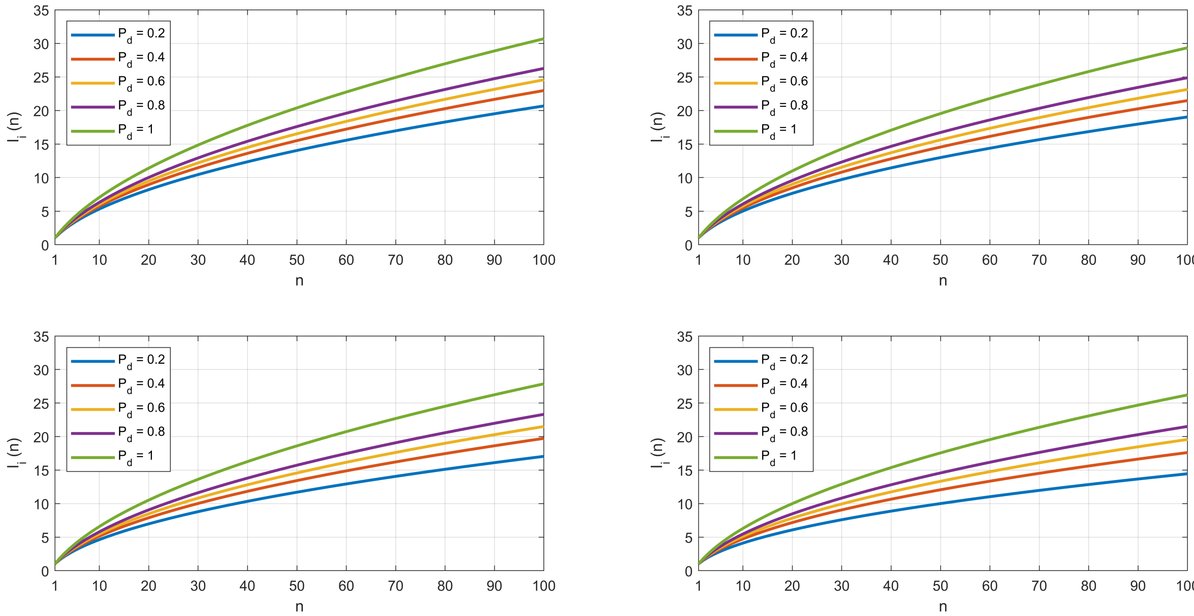

Figure 2.8: Integration Factor, $I_i(n)$, as function of the number of integrated pulses, n, for some P_d, considering, from left to right and from top to bottom, $P_{fa} = 10^{-6}$, $P_{fa} = 10^{-5}$, $P_{fa} = 10^{-4}$, $P_{fa} = 10^{-3}$.

Alternatively, rearranging and replacing (2.14) in (2.16), the Radar Equation becomes

$$R_{\max}^4 = \frac{P_t G^2 n E_i(n) \lambda^2 \sigma}{(4\pi)^3 k T_0 B_W^{RX} F (S/N)_1}. \tag{2.17}$$

2.2.2 Radar Cross-Section

According to IEEE, the formal definition of RCS is [50]:

> A measure of the reflective strength of a radar target, usually represented by the symbol σ and measured in square meters. RCS is defined as 4π times the ratio of the power per unit of solid angle scattered in a specified direction to the power per unit area in a plane wave incident on the scatterer from a specified direction. More precisely, it is the limit of that ratio as the distance from the scatterer to the point where the scattered power is measured approaches infinity.

In other words, the RCS, σ, is proportional to the ratio between the power density reflected by the target, $|E_{rft}|^2$, and the power density incident on it, $|E_{ind}|^2$, within the limit of an infinite distance between the transmitter and receiver, as given by

$$\sigma = \lim_{r \to \infty} 4\pi r^2 \left(\frac{|E_{rft}|^2}{|E_{ind}|^2} \right), \tag{2.18}$$

in which E_{rft} and E_{ind} are, respectively, the scattered and the incident electric field, and r is the distance between the transmitter and the receiver, in meters.

This definition assumes that the target is in free space without obstacles or interference, and in the distance condition of *far field*, so the incident wave on the target becomes plane. The far field distance, d_F, is given by [51]

$$d_F \geq \frac{2D^2}{\lambda}, \tag{2.19}$$

in which, D is the length of the antenna and λ is the wavelength of the incident wave, both in meters.

There are three RCS measurement types: *monostatic* or *backscatter*, *forward-scatter*, and *bistatic*. The monostatic is the most common method of RCS measurement, at it the transmitter and receiver antennas are col-located, i.e., the incident and reflected scattering directions are the same but in opposite sense. They can use or not the same antenna to transmit and receive. The forward-scatter is the measure of the scattered power in the forward direction of the transmitter antenna, and it is usually 180° out of phase with the incident wave. The bistatic is when the scattered energy is dispersed or bounced back in all directions, except for the direction of incidence or its opposite. Figure 2.9 illustrates these three RCS measurement types, regarding the transmitter, T_X, and receiver, R_X, antennas and target location. Transmitter antenna, T_X, is the same for them.

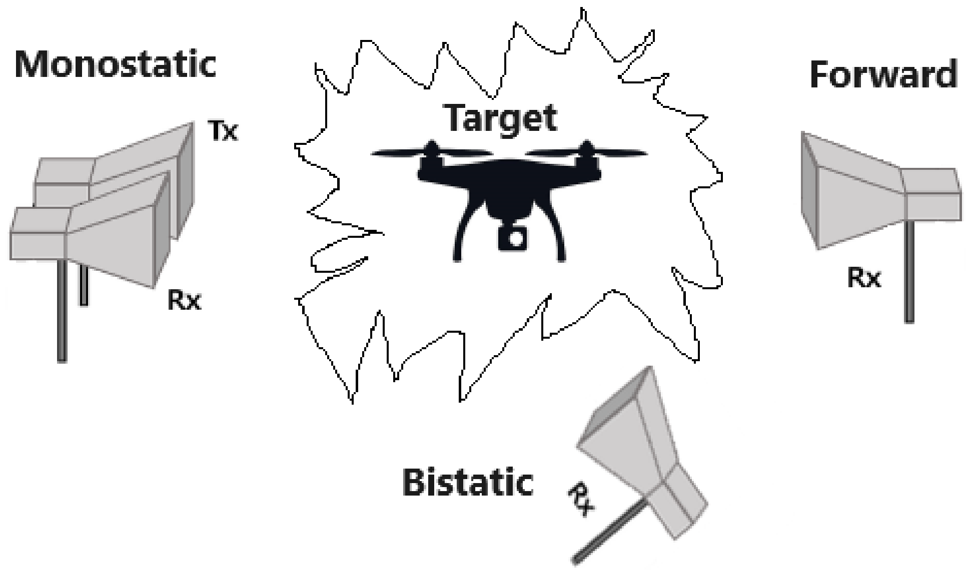

Figure 2.9: RCS measurement types: monostatic or backscatter, forward-scatter, and bistatic.

In relation to a radar system, RCS expresses the ability of a target to reflect the radio waves that fall on it, that is, it is a measure of radar visibility. It depends on the shape, size, orientation, and material of the target, as well as the frequency and polarization of the incident wave. It is measured in square meters (m^2) or in its decibel form ($dBsm$) and can vary from small values, for stealth or small targets, to considerable values, for spherical targets or targets with metallic surfaces. Table 2.2 presents average RCS values of some targets for radars with operating frequencies in the X-band [26].

Table 2.2: Common measured RCS in X-band frequency.

Target	$\boldsymbol{\sigma(m^2)}$	$\boldsymbol{\sigma(dBsm)}$
Large bird	0,01	-20
Conventional winged missile	0,1	-2
Human	1	0
Helicopter	3	4,8
Cabin cruiser	10	10
Automobile	100	20
Pickup truck	200	23

The mechanism of scattering depends on body size (L) relative to the wavelength (λ) of the incident wave. There are three scattering regions: Rayleigh, Resonant or Mie, and Optics. The Rayleigh region is defined for $L \ll \lambda$, where the scattering is induced by dipole moments, i.e., the incident electromagnetic wave interacts with the target and induces an electric current on its surface. The induced current then radiates a secondary electromagnetic wave, the scattered one. In this region, RCS is determined by the volume of the scattered target rather than by its shape [34].

The resonant or Mie region occurs when $L \approx \lambda$, in which surface wave effects such as edge, and creeping waves traveling along with optical effects are relevant. Alterations in the RCS are a result of frequency variations, due to the constructive and destructive interference of two waves. One wave is the direct reflection from the target's front face. The other is the creeping wave that circumnavigates the target, returns to the radar, and interferes with the reflection from the target's front [27].

Finally, the Optics region is established when $L \gg \lambda$, resulting in insignificant surface wave effects whereas only optical effects take place and the RCS approaches the physical area of the target face reflected as the frequency is increased. It is important to notice that this does not mean that the RCS is equal to the geometric area of the target [26].

Since there is no unanimity, in the literature, about the limits of these regions, this thesis adopted, in practical terms, that the regions are limited by $L < \lambda$ (Rayleigh), $\lambda < L < 10\lambda$ (Resonant or Mie) and $L > 10\lambda$ (Optics) [27]. Figure 2.10 shows a sphere's RCS in these three regions, in which σ is normalized regarding the projected area of the sphere (i.e., the area of a circle, πa^2) and the sphere circumference is normalized by the wavelength (λ) [28].

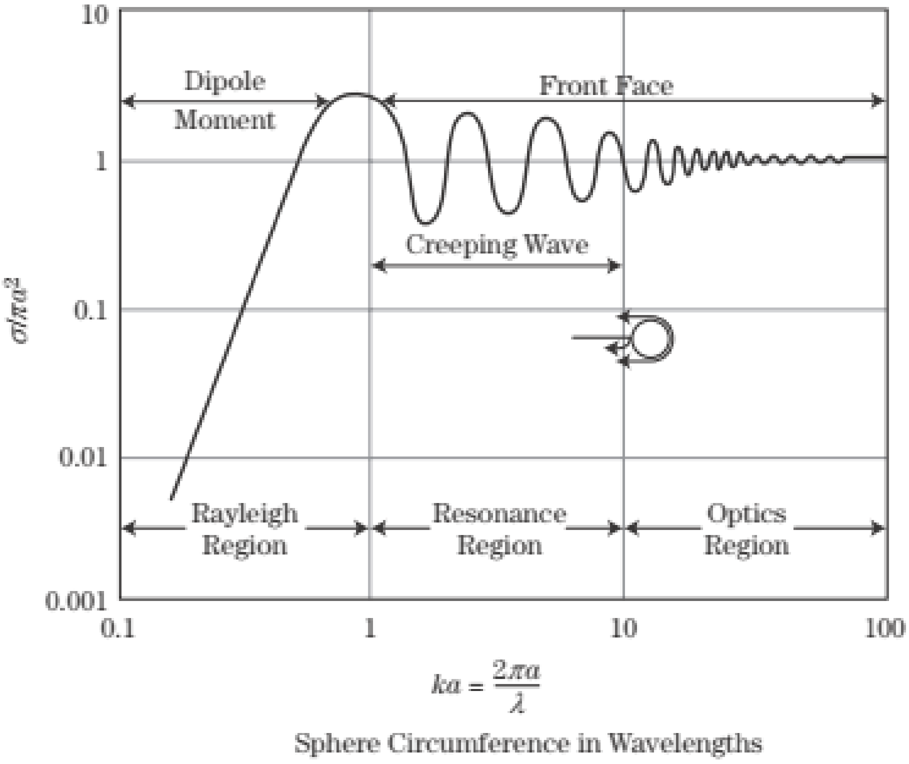

Figure 2.10: Normalized sphere's RCS in Rayleigh, Resonance or Mie, and Optics regions [28].

Another important analysis of the RCS is the Swerling cases. Introduced by Peter Swerling in 1954, they are widely used in radar system design and analysis. These cases are a set of statistical models that describe the fluctuations of the target's RCS due to its movement or orientation [52]. The Swerling cases differ in how they assume the target RCS changes over time and space [53]. The Swerling I case applies to a target that has its RCS amplitude varying, independently, from scan to scan, ruled by a chi-square probability density function (PDF) with two degrees of freedom, such small UASs. The Swerling II case applies to a target that has the same PDF characteristics as the Swerling I case, but its RCS changes randomly from pulse to pulse [54]. This can be used to model a target with diversity, such as frequency, space, or polarization.

The Swerling III and IV cases apply to a target that has one large scatterer and several smaller ones, such as a ship. The Swerling III case assumes that the RCS of the large scatterer is constant, while the RCS of the smaller ones changes randomly from scan to scan, according to a chi-square PDF with four degrees of freedom. The Swerling IV case assumes that the RCS of both the large and small scatterers changes randomly from pulse to pulse, with the same PDF as Swerling III case [54].

There is, also, the Swerling 0 case (steady target or nonfluctuating target), which is a reference value that assumes a constant average target RCS. In general, Swerling demonstrated that the statistical properties of Swerling I and II models are applicable to targets made up of numerous small scatterers with similar RCS values. On the other hand, the statistical characteristics of Swerling III and IV models are suitable for targets composed of one large RCS scatterer accompanied by many small scatterers with equal RCS values [52].

The fluctuations of the target RCS affect the radar performance in terms of detection probability and range. Named as fluctuation loss, L_f, it is associated with the reduction in detection probability or range due to the variations of the target RCS value. The fluctuation loss depends on the number of pulses integrated, the detection probability, the false alarm probability and the Swerling case. Figures 2.11, 2.12, and 2.13 show L_f as a function of P_d for Swerling cases I, II, III, IV, and 0, considering $P_{fa} = \{10^{-10}, 10^{-4}\}$ and assuming the number of integrated pulses $n = \{4, 10, 20\}$.

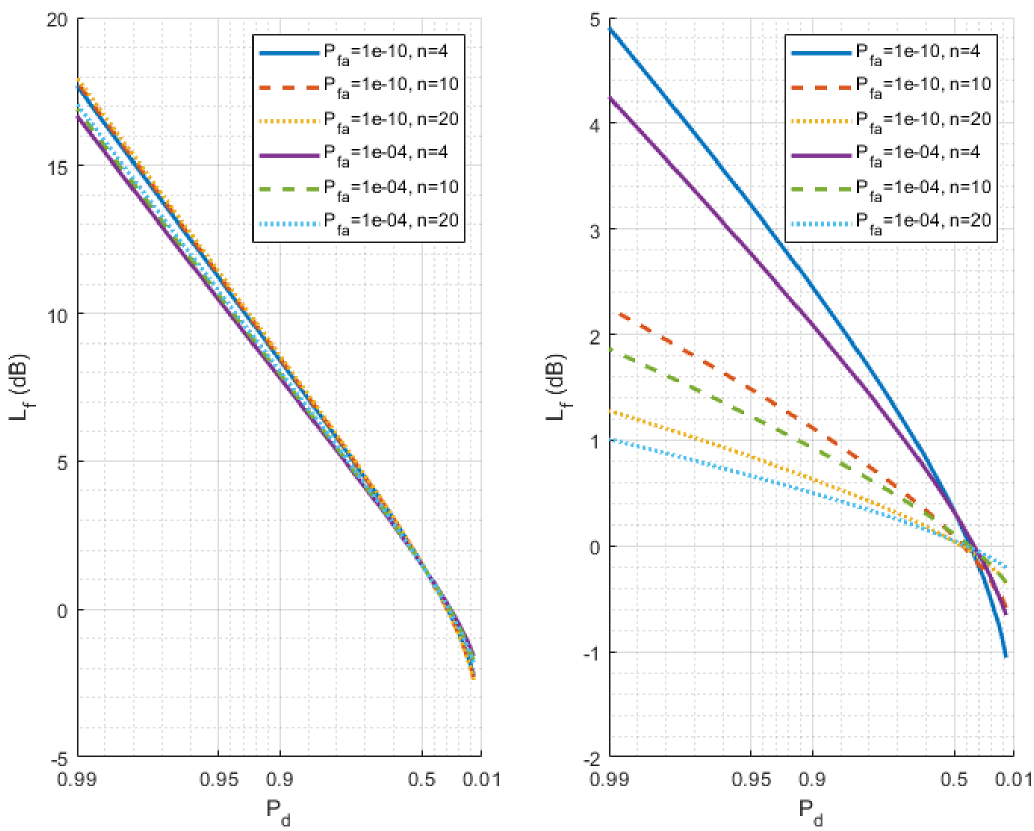

Figure 2.11: L_f as a function of P_d for Swerling cases I (left) and II (right).

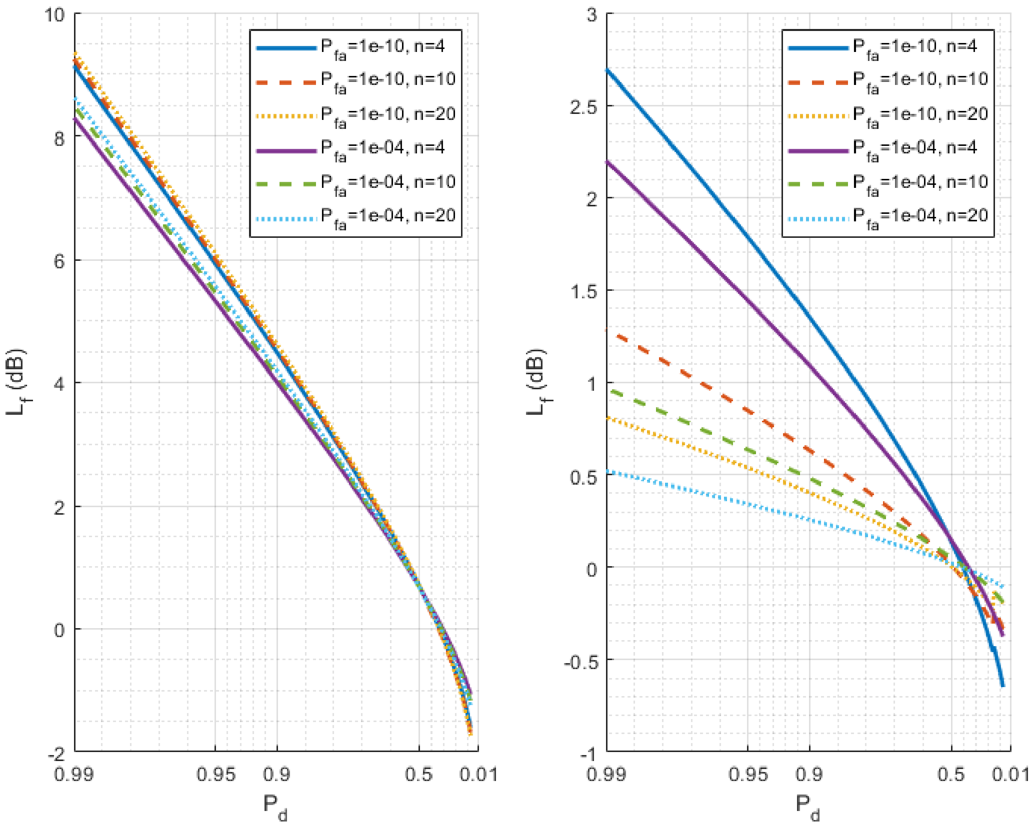

Figure 2.12: L_f as a function of P_d for Swerling cases III (left) and IV (right).

This outcome indicates that for the Swerling I and III scenarios, where there's no variation in RCS from pulse-to-pulse, the loss is not significantly affected by the number of pulses, n. However, it's highly dependent on the detection probability, P_d. Elevated required P_d values lead to substantial fluctuation loss. In the Swerling II and IV models situation, where the RCS varies from pulse-to-pulse, the L_f is highly dependent on the number of pulses and diminishes quickly with n. The fluctuation loss doesn't strongly depend on P_{fa} in both Swerling I and III scenarios. In Swerling 0 case, it is possible to note that the loss isn't significantly affected by increasing P_d because is the case of a steady target, i.e., it doesn't have significantly variation in the average RCS values.

Adding L_f in (2.17), results in

$$R_{\max}^4 = \frac{P_t G^2 n E_i(n) \lambda^2 \sigma}{(4\pi)^3 k T_0 B_W^{RX} F (S/N)_1 L_f}. \tag{2.20}$$

Despite introducing the integration loss, it is important to notice that (2.20) still does not consider others internal losses of a radar system, often called *System Losses*.

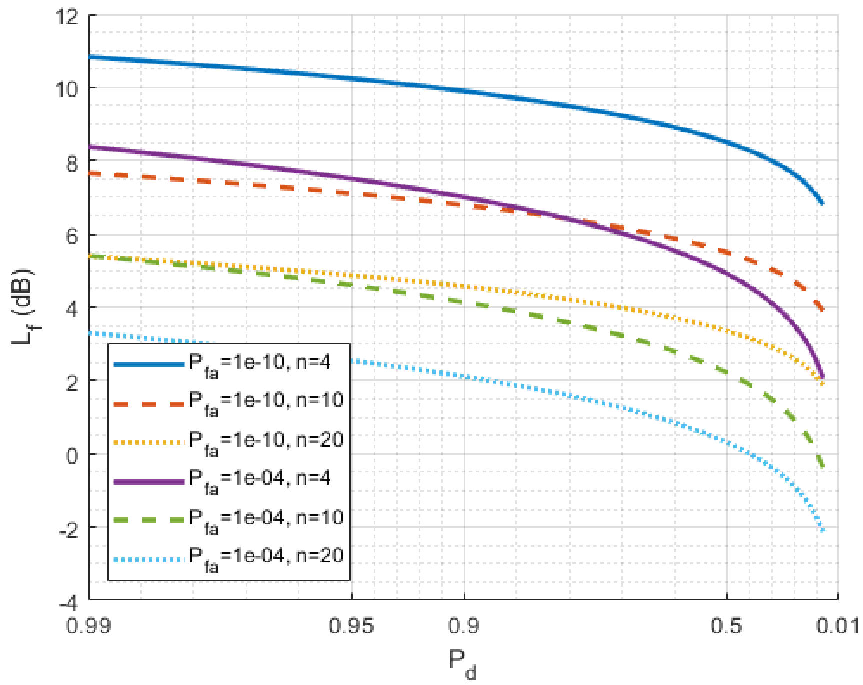

Figure 2.13: L_f as a function of P_d for Swerling case 0.

2.2.3 System Losses

There are various losses associated with a radar system, such as microwave plumbing losses, antenna losses, signal processing losses, fluctuation loss, operator loss, and equipment degradation. Individually, they can be small, but when are added up they can result in a significant total loss. According to [46], it is not unusual for the system loss, L_s, to assume values varying from 10 dB to over 20 dB.

Despite L_s being an important parameter, some of it can only be, arbitrarily, assigned such as the operator losses, and other losses are statistical-nature and can only be estimated [55]. Another problem in obtaining L_s parameter, is the information from the manufacturer. According to [26], there are different methods for estimating system losses and their impact on radar performance, and there is no consensus on which one is the best. Radar sellers may tend to underestimate the total system loss and claim a higher performance than what a radar buyer or an independent evaluator may expect. To verify or compare the performance claims made by different radar manufacturers, it is essential to know what losses each radar designer has accounted for.

Adding L_s in (2.20), it becomes

$$R_{\max}^4 = \frac{P_t G^2 n E_i(n) \lambda^2 \sigma}{(4\pi)^3 k T_0 B_W^{RX} F (S/N)_1 L_f L_s}. \tag{2.21}$$

2.2.4 Effects of Electromagnetic Propagation in the Atmosphere

There are two factors that affect the performance of a radar system, which are related to its operating frequency.

The first factor is the one-way attenuation caused by the absorption of gases in the atmosphere. Figure 2.14 shows the attenuation due to the resonance of water vapor and oxygen molecules as a function of the radar system's operating frequency [56]. Note that there is a resonance peak in the water vapor curve at approximately 22 GHz, at which the attenuation is approximately 0.19 dB/km. The resonance peak due to oxygen molecules is at 60 GHz, in which the attenuation jumps from 0.27 dB/km at 50 GHz to 15.17 dB/km.

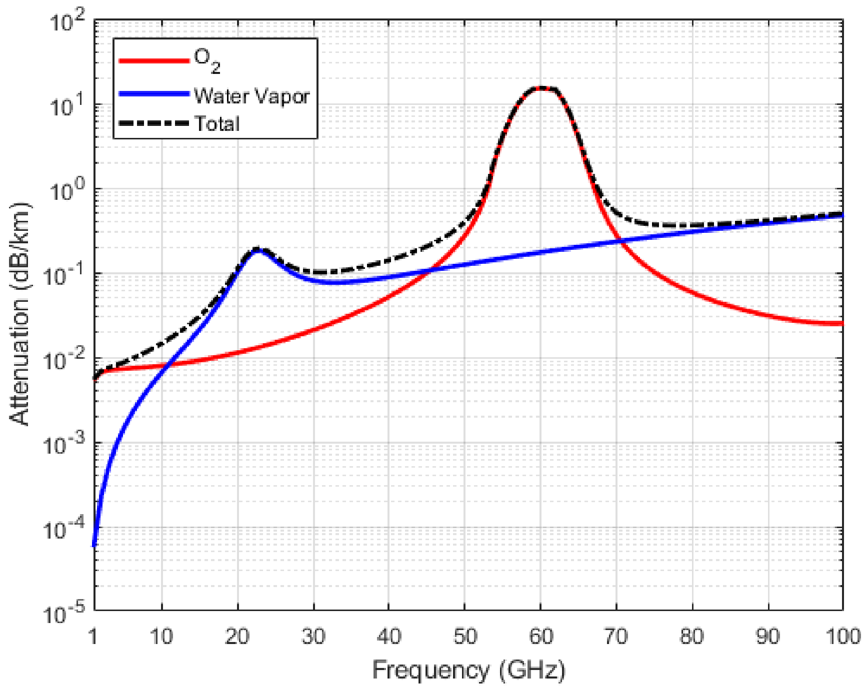

Figure 2.14: Attenuation of the electromagnetic waves by water vapor and oxygen as a function of the frequency.

Note that for frequencies below 10 GHz, atmospheric attenuation has no significant effect, with its total value being in the order of 10^{-2} dB/km. For frequencies above 10 GHz, the attenuation not only increases, but becomes more dependent on peculiar absorption characteristics of atmospheric gases, such as water vapor and oxygen, which causes the resonance peaks [57].

The second factor is the one-way attenuation caused by weather conditions. Figure 2.15 shows the attenuation effect for different rainfall intensities as a function of the operating frequency [57]. Note that frequencies below 10 GHz begin to experience attenuation greater than 1 dB when the precipitation rate is greater than 40 mm/h, corresponding to excessive rainfall. Frequencies close to 100 GHz are attenuated by the same amount from light rain, corresponding to a precipitation rate of just 1 mm/h.

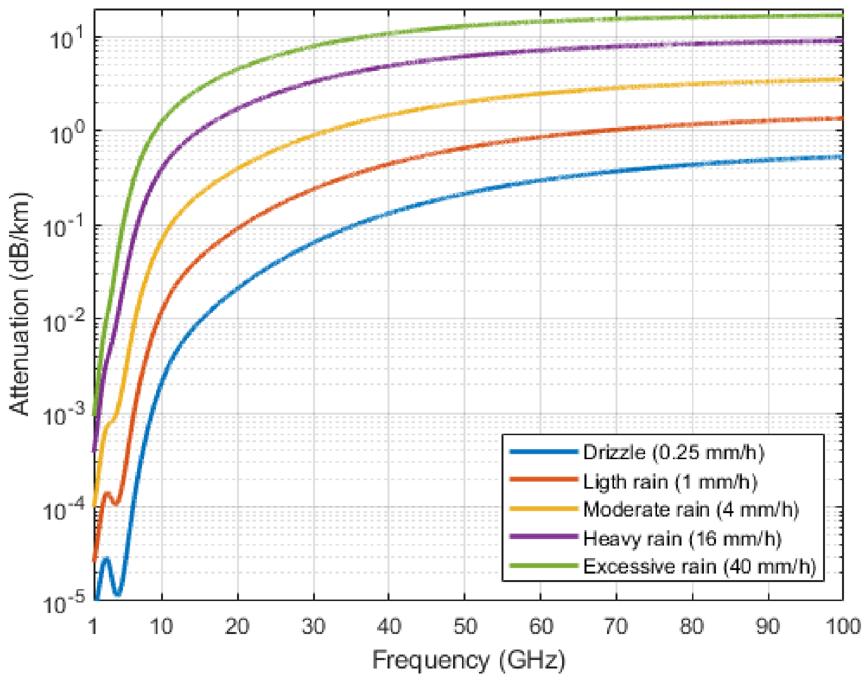

Figure 2.15: Attenuation of the electromagnetic waves by rain as a function of the frequency.

Both attenuations are included in the numerator of (2.17) by the factor $e^{-2\alpha R}$ [26], in which α is the sum of the attenuations of Figures 2.14 and 2.15, in m^{-1}, and R is the distance to the target, in meters. Thus, adding this term in (2.21), the *pulsed radar range equation* becomes

$$R_{\max}^4 = \frac{P_t G^2 n E_i(n) \lambda^2 \sigma e^{-2\alpha R}}{(4\pi)^3 k T_0 B_W^{RX} F (S/N)_1 L_f L_s}. \tag{2.22}$$

Important to notice that (2.22) is used for pulsed radar system only. For a FMCW radar system, instead of the improvement factor, $I_i(n)$, due to the integration of pulses, there is the relation given by

$$B_W^{TX} T_s = \frac{B_W^{TX}}{f_s}. \tag{2.23}$$

Then, replacing (2.15) by (2.23) in (2.22) and simplifying it, the *FMCW radar range equation* is given by

$$R_{\max}^4 = \frac{P_{cw} G_t G_r \lambda^2 \sigma e^{-2\alpha R}}{(4\pi)^3 k T_0 F (S/N)_1 L_f L_s f_s}, \tag{2.24}$$

in which P_{cw} is the average transmit power of the FMCW radar.

In this context, the construction of a radar must consider the purpose of the equipment. Generally, low-frequency radars require larger antennas and are not accurate at measuring angles and distances. On the other hand, they can accommodate higher voltages and currents, generating greater power and, consequently, greater range. Furthermore, at low frequencies, radars suffer less from external factors. Unlike low-frequency radars, those that use high frequency have smaller antennas that are easy to install and move, in addition to providing more precise measurements of angles and distance. However, they suffer more from attenuation caused by external factors and, therefore, have a shorter range.

2.3 Summary

Chapter 2 presented a comprehensive exploration of radar systems, delving into their intricate functions and historical evolution. Beginning with the definition of radar systems as devices emitting and receiving electromagnetic waves for target detection, measurement, and tracking, the chapter classified radar systems based on operating frequency bands, incorporating codes from IEEE standard and ITU-R recommendation. The discussion then turned to the Doppler effect, detailing the alterations in wave frequency due to relative motion between the radar source and observer. Noteworthy distinctions between coherent and incoherent radar systems were introduced, along with the concept of the micro-Doppler effect. Additionally, an examination of signal waveforms in radar systems was included, covering pulsed, CW, and FMCW radars, with insights into their advantages and applications. The chapter culminates in an exploration of the radar equation, revealing two distinct radar range equations: one for pulsed radars and one for FMCW radars. Addressing key parameters such as signal-to-noise ratio, radar cross-section, system losses, and atmospheric attenuation, Chapter 2 provided a comprehensive and invaluable resource, offering a nuanced foundation for understanding the diverse applications and complexities of radar systems across historical and contemporary contexts.

Chapter 3

UAS Detection by X-Band Pulsed Radar

In the dynamic scenario of modern warfare, the use of UASs has become increasingly prevalent. Recent conflicts around the world have highlighted the strategic importance of drones in war operations. In 2022, the conflict between Russia and Ukraine has witnessed significant use of drones for reconnaissance and intelligence gathering. News reports, such as those from BBC News [58], highlight instances in which Russian and Ukrainian forces deploy drones for surveillance along the front lines. In 2023, the ongoing conflicts that involve the organization of Israel and Hamas, the use of drones, for military purposes, has become a growing concern. According to reports from The New York Times [59], Hamas has employed drones to carry out surveillance and even deploy explosives over enemy troops.

As the role of drones evolves in the theater of war, the need for effective drone detection technologies has become paramount. The ability to detect and respond to these drones promptly is vital for safeguarding civilian populations and military assets. Radar technology, in conjunction with other detection methods, plays a key role in improving situational awareness and mitigating the threat posed by such unmanned aircraft [60]. In the context of drone detection, radar systems can perform real-time drone detection and tracking, providing valuable information for a timely response. Radar has several advantages, including long-range detection - providing early warning to security forces, all-weather capability - radar is not affected by adverse weather conditions, and independence from lighting conditions - radar operates effectively day and night - making it a reliable technology for continuous monitoring [61]. Despite their advantages, radar detection also has some challenges, such as false positives - mistaking birds or other objects for drones - and limited identification - it may not provide detailed information about the drone type or payload [60].

Considering the UAS detection by radar systems mentioned above, the present chapter has the following contributions:

- Proposition of one method of radar performance analysis. This is done through the radar range equation and known target parameters. Comparison of the proposed method and the radar range equation helps infer the value of the system loss parameter.
- Comparison of the detection range of the simulated data between AREPS and the proposed method, with respect to the detection probability of a commercial UAS.
- Evaluation of the proposed method based on field measurements, using the Furuno FAR-2117 X-band pulsed radar and the DJI Phantom IV UAS.

The remainder of this chapter is organized as follows: Section 3.1 formulates the problem of UAS radar detection by an X-band pulsed radar, regarding the existing infrastructure of the Brazilian Navy and previous works in that area. In the following, Section 3.2 introduces the mathematical formulation for the two proposed methods for analyzing the radar range equation and shows how the comparison between them both helps to determine the system loss parameter of a radar system. Section 3.3 presents the employed radar and UAS on the field measurements, as well as the drone's RCS simulation. Section 3.4 discusses the numerical results by comparing the simulations and the field measurements, and finally, Section 3.5 presents the final remarks of this chapter.

3.1 Problem Formulation

Radar detection of UAS stands out because it overcomes some of the main limitations of other types of detection [62]. As it is already consolidated and widely used in military and automotive applications, radar has been used in several studies on UAS detection. For example, in [63], a pulsed radar operating in the Ku-band was used to analyze the detection probability of 3 UASs with RCS of, respectively, 0.5 m^2, 1 m^2, and 1.5 m^2. According to the authors, it is possible to detect them with a high probability of detection at a distance of up to 1000 m. In [64], the authors analyzed the use of a FMCW radar, operating in the X-band, for the detection of UAS. They used a fixed-wing and a quadrotor UAS. According to the work, it was possible to detect the fixed wing at a distance of 600 m, while a quadrotor was detected at 400 m due to a lower RCS in the configuration proposed by the authors. In [65], the focus is on the impact of flying birds on the detection and identification of commercials UASs by radar. The researchers used a Ku-band pulse Doppler phased array radar to collect echoes from a pigeon and a commercial UAS (DJI Phantom 3 Vision). It was possible to detect the bird and the UAS at a distance of 12 and 11 km, respectively. The statistical results revealed that flying birds and drones exhibit similar RCS, velocity range, signal fluctuation, and signal amplitude. Importantly, the study suggests that the interference caused by flying birds significantly lowers the identification probability of UASs in radar automatic target recognition. In general, the findings highlight flying birds as a major source of interference in radar detection and identification of consumer drones, particularly in airport environments. In [66], the authors developed a small, low-powered radar system based on the ubiquitous radar concept, which can detect and track small commercial drones at ranges up to 2 km. The system uses a FMCW waveform at 8.75 GHz (X-band). Their system was tested with a DJI Phantom 4 drone, which has a low RCS and can fly at low altitudes and speeds. The tests showed that the system was able to detect and track the drone from the beginning to the end of the flights, with excellent range-speed association and acceptable azimuth accuracy. The system also achieved a detection probability of more than 0.7 for a false alarm probability of 10^-3. Furthermore, the authors used the received power data from the drone echoes to compute the drone RCS. They found that the drone RCS had an average value of 0.02 m^2 and followed an exponential distribution, which corresponds to a Swerling 1 target model.

Additionally, in [67], the authors presented a relatively new concept employing a multiple-input, multiple-output orthogonal frequency-division multiplexing (MIMO-OFDM) radar system for drone detection and localization in real-time. The system used a $4x4$ MIMO patch antenna array connected to software defined radios and operated at 4.05 GHz carrier frequency and 66.67 MHz bandwidth. The authors applied OFDM modulation with interleaved subcarriers for each transmit antenna and Fourier beam forming for direction-of-arrival estimation. Under test, the system successfully detected a DJI Phantom 3 Standard drone in a real-world scenario, despite the high clutter level from a metal balustrade, up to 27 m. The other technique of UAS detection using a radar system is the measurement of the micro-Doppler effect. For example, in [68], the authors proposed a unique method for extracting micro-Doppler characteristics, using spectral kurtosis to classify loaded or unloaded UASs. For this, they used a coherent pulsed radar, named NetRAD, which operates at 2.4 GHz (S-band) and the DJI Phantom Vision 2+, which hovered at 70 m and flew approximately from 90 m to 60 m from the radar. Using six different payloads configurations (unloaded, 200 g, 300 g,400 g, 500 g, and 600 g), the proposed feature achieves an average payload identification accuracy of 92.61%.

In general, the above-mentioned works investigated the use of radars with dedicated and ground-based infrastructure for drone detection. In this context, since no study or investigation has been found in the literature on the use of an X-band pulsed maritime radar for drone detection and, considering that the Brazilian Navy already has several radars of this type installed on ships and in coastal areas for navigation and monitoring of maritime traffic, this chapter proposes and analyzes the performance of the FAR-2117 radar, from Furuno® company, for the detection of a commercial UAS, the Phantom IV from DJI® company. The choice of this specific drone is due to the relationship between its significant size (L) and the wavelength (λ) of the X-band radar, with $L \approx 10\lambda$. This value places the drone on the limit between the resonance and optical regions, shown in Figure 2.10. In the former region there is a greater oscillation in the RCS of the UAS and therefore a lower probability of drone detection, while in the latter region there is a tendency towards stabilization of the RCS oscillations and, therefore, a greater probability of drone detection. This investigation is initially carried out through simulation and, later, via field measurement with the Phantom IV from DJI company.

3.2 Mathematical Formulation

Considering (2.22) presented in Chapter 2, observe that to analyze and choose a radar system for a given purpose, it is necessary to know all the parameters of the equation for a determined P_d and P_{fa}, which are generally not widely available by manufacturers. Since both $E_i(n)$ and $(S/N)_1$ depend on P_d and P_{fa}, then, for simplicity, replace (2.14) in (2.22) to get just one variable, $(S/N)_n$, dependent on P_d and P_{fa}. Thus

$$R_{\max}^4 = \frac{P_t G^2 \lambda^2 \sigma e^{-2\alpha R}}{(4\pi)^3 k T_0 B_w^{rx} F (S/N)_n L_f L_s}. \tag{3.1}$$

To overcome the difficulties of obtaining all the parameters of (3.1) to perform a radar range analysis, take the ratio between two different targets, with their own $(S/N)_n$ values

($(S/N)_{n,1}$ and $(S/N)_{n,2}$), RCS values (σ_1 and σ_2), and fluctuation loss (L_{f_1} and L_{f_2}), then

$$\frac{R^4_{\max_1}}{R^4_{\max_2}} = \frac{\dfrac{P_t G^2 \lambda^2 e^{-2\alpha R}}{(4\pi)^3 F k T_0 B_w^{rx} L_s} \dfrac{\sigma_1}{L_{f_1}(S/N)_{n,1}}}{\dfrac{P_t G^2 \lambda^2 e^{-2\alpha R}}{(4\pi)^3 F k T_0 B_w^{rx} L_s} \dfrac{\sigma_2}{L_{f_2}(S/N)_{n,2}}}. \tag{3.2}$$

Note that, except for L_f and σ, all other parameters are uniquely dependent on the radar system design requirements. Except for $(S/N)_n$ which also depends on P_d and P_{fa} of each target. Thus, considering that the radar system operates in the same conditions for both targets, then (3.2) can be simplified as

$$\frac{R^4_{\max_1}}{R^4_{\max_2}} = \frac{\sigma_1 L_{f_2}(S/N)_{n,2}}{\sigma_2 L_{f_1}(S/N)_{n,1}}. \tag{3.3}$$

Replacing (2.13) in (3.3) with the proper indices

$$\frac{R^4_{\max_1}}{R^4_{\max_2}} = \frac{\sigma_1 L_{f_2}\left[-5\log(n) + \left(6,2 + \dfrac{4,54}{\sqrt{n+0,44}}\right)\log(A_2 + 0.12A_2B_2 + 1.7B_2)\right]}{\sigma_2 L_{f_1}\left[-5\log(n) + \left(6,2 + \dfrac{4,54}{\sqrt{n+0,44}}\right)\log(A_1 + 0.12A_1B_1 + 1.7B_1)\right]}, \tag{3.4}$$

in which $A_i = \ln(0.62/P_{fa_i})$ and $B_i = \ln[P_{d_i}/(1-P_{d_i})]$, $i = \{1,2\}$.

Therefore, two methods of analyzing the parameters $R_{\max}$, P_d, P_{fa} of a radar for a given target are proposed, which are described below.

Method I: This method uses (3.1) for an individual analysis, which requires knowledge of all radars (P_t, G, λ, α, F, B_w^{rx} and L_s) and the target parameters (σ and L_f). The radar parameters can be found in its Operating Manual [69], in which L_s will be varied over a set of possible values, due to the difficult in obtaining the correct value from the manufacturer. The value of σ of the drone (target) will be estimated by simulations, while L_f will be obtained from the values of P_d and P_{fa} and Figures 2.11 and 2.12 depending on the Swerling case in which the drone fits.

Method II: This method, using (3.3), offers a comparative analysis. Knowing the parameters σ_1, L_{f_1}, P_{d_1}, P_{fa_1} and $R_{\max_1}$ of a reference target, it is possible to indirectly determine one of the parameters (σ_2, L_{f_2}, P_{d_2}, P_{fa_2} or $R_{\max_2}$) from another target of interest.

3.3 Materials and Method

The radar, model FAR-21x7 from Furuno company, is built to meet the exact performance standards stipulated by the International Maritime Organization (IMO) and the International Electrotechnical Commission (IEC), and therefore follows all specifications and resolutions of these organizations. This type of radar can be X-band or S-band, have antennas of different sizes, rotation speeds, and different transmission power. Basically, this radar consists of a rotating antenna, an RF transceiver, and a monitor. The radar, antenna, and transceiver models used for field measurements in this thesis are, respectively, FAR-2117, XN-24AF, and RTR-078. Table 3.1 shows the specifications of the radar used.

Table 3.1: Furuno FAR-2117 radar's technical specifications.

Parameter	**Description**
Frequency (f)	9410 MHz
Wavelength (λ)	31.9 mm
Polarization	Horizontal
Transmit Power (P_t)	12 kW
Antenna Length	2.5 m
Antenna's Rotation Speed	24 rpm
Antenna Gain (G)	31.5 dB
Horizontal Beam Width	0.95°
Vertical Beam Width	20°
Pulse Length (PL)	0.07/0.15/0.3/0.5/0.7/1.2 μs
Pulse Repetition Frequency (PRF)	3000/1500/1000/600 Hz
Receiver Bandwidth (B_w^{rx})	60 MHz
Noise Figure (F)	6 dB

The Furuno FAR-2117 radar is installed on top of the building of the Geosciences Institute at Praia Vermelha Campus of the Universidade Federal Fluminense (UFF), located in Niterói, RJ, and faces Guanabara Bay, as shown in Figure 3.1. The antenna altitude in relation to sea level is 32 m. The atmospheric conditions on the day of the measurement were favorable, with few clouds and no rain over the bay.

The UAS used was the DJI Phantom IV, shown in Figure 3.2. This aircraft is made up of four propellers, has a high-resolution camera, a built-in GPS, and the majority of its structure is built with plastic. Furthermore, this quadcopter measures approximately 35 cm diagonally and weighs approximately 1.38 kg.

To estimate the RCS of the drone, a simulation was carried out using *software* Feko® from Altair® company. Altair's Feko® is a comprehensive tool for high-frequency electro-

Figure 3.1: Radar Furuno FAR-2117's location, with Guanabara Bay in the background.

Figure 3.2: DJI Phantom IV.

magnetic simulations, used across various industries including aerospace, defense, automotive, communications, and consumer electronics [70]. It's a robust tool for designing and optimizing connected products, ensuring EMC compliance, and advancing radar technologies. Among other capabilities, this software is used for antenna design and placement, radio coverage, network planning, and spectrum management. Furthermore, Feko® performs RCS and scattering analysis. It enables customers to analyze performance for a wide range of electrical sizes and industries [70].

Thus, with this software, the incidence of a plane wave, with the same radar operating frequency, on the drone was simulated, varying the azimuth angles (ϕ) in steps of $1°$, as shown in Figure 3.3. The simulation was carried out using the Ray Launching Geometrical Optics (RL-GO) method, which is a technique that uses ray tracing to model the dispersion of electromagnetic waves based on the theories of propagation, reflection, and refraction. This method uses fewer computational resources and has relatively high accuracy for calculating RCS of drones [70].

After estimating the RCS of the drone, a simulation of the radar equation was carried

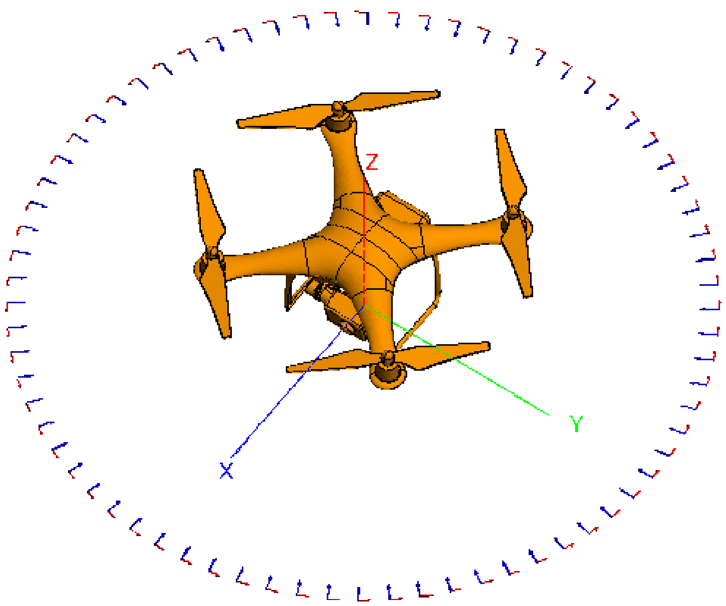

Figure 3.3: Simulation set up of DJI Phantom IV's RCS at Feko®.

out in the MATLAB® software, using the two analysis methods, presented in Section 3.2, to analyze the drone's maximum detection distance.

For Method I, it was used the parameters of the radar FAR-2117 presented in Table 3.1, considering the radar operating with $f_p = 3000$ Hz, $PL = 0.07$ μs and $n = 20$ given by (2.12), these parameters allow the radar to emit its pulses at a faster interval with a greater resolution, being the best configuration to detect near and small targets. The system losses, L_s, were varied from 10 to 20 dB in steps of 2dB, and thus, it is possible to estimate L_s by comparing both methods. Additionally, the fluctuation loss, L_f, for DJI Phantom IV, was obtained from Figure 2.11, for $P_{fa} = 10^{-4}$ [71] and P_d varying from 0.1 to 1 in steps of 0.01, considering it a Swerling case I because its RCS varies from scan to scan during the observation time. Table 3.2 shows the exact values of L_f for some P_d.

Table 3.2: Fluctuation loss of DJI Phantom IV as a Swerling case I.

$\boldsymbol{P_d}$	L_f (dB)
0.1	-1.8087
0.2	-0.9512
0.3	-0.1622
0.4	0.6372
0.5	1.4997
0.6	2.4857
0.7	3.6924
0.8	5.3282
0.9	8.0522
1	26.3426

For Method II, for the reference target, data relating to a channel marking buoy was used, taken from IMO resolution MSC.192(79) [71]. This resolution standardizes the parameters and performance of marine radars, including the Furuno FAR-2117 radar. According to this resolution, the parameters of the aforementioned buoy are $\sigma_1 = 1$ m^2, $R_{\max_1} = 3700$ m, $P_{d_1} = 0.8$, and $P_{fa_1} = 10^{-4}$, where $L_{f_1} = 1.5424$ dB $= 1.4264$ W was taken from Figure 2.13 for the values of P_{d_1} and P_{fa_1}, considering the buoy as a steady target or a Swerling case 0.

Subsequently, the Advanced Refractive Effects Prediction System (AREPS)® software was used to simulate the radar range for the DJI Phantom IV, using data on the weather conditions at the measurement location. This software is used in scientific research and military operational analysis to calculate and display various aids for making decisions regarding electromagnetic propagation, such as radar range prediction and the detection probability of a given target by a specific radar [72]. To do so, it is necessary to insert data from the radar, as shown in Figure 3.4, and the target, as shown in Figure 3.5, as well as the local climatology, which in this case was used the *standard atmosphere* available in the software.

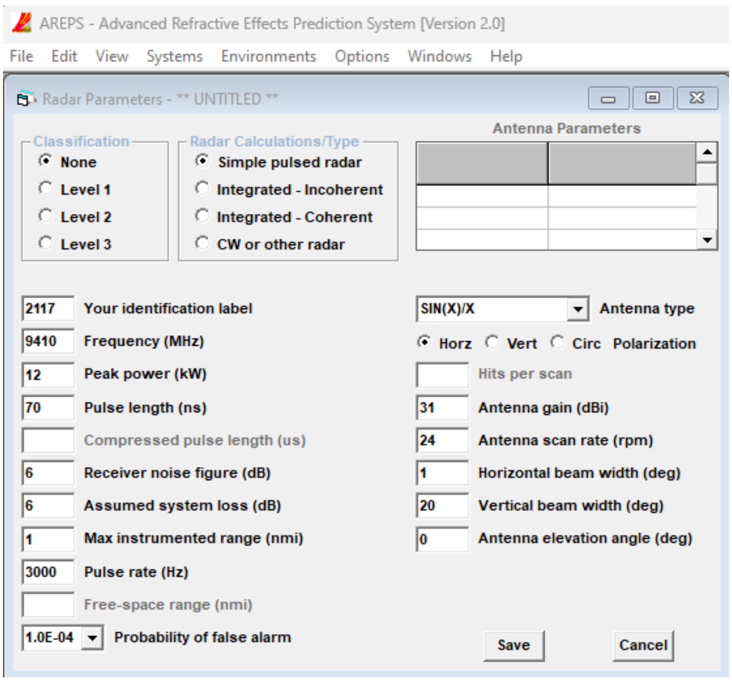

Figure 3.4: AREPS's screen to insert radar data.

Based on the simulated results in software MATLAB and AREPS, an evaluation was made of the performance that the Furuno FAR-2117 radar has to detect the DJI Phantom IV drone, as well as a comparison between the maximum detection distances obtained via simulation and through field measurements. The radar was configured with a pulse

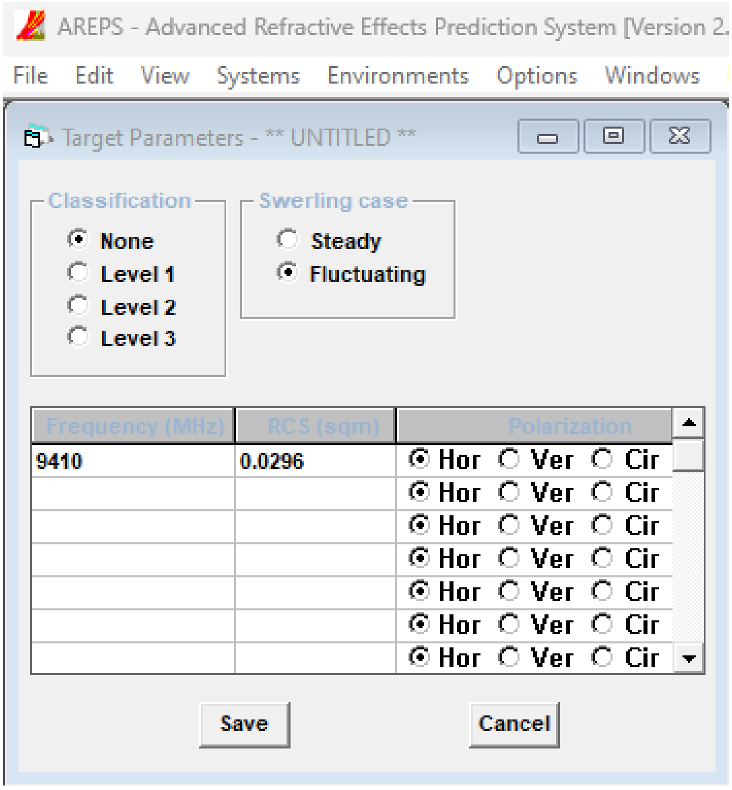

Figure 3.5: AREPS's screen to insert target data.

repetition frequency of 3000 Hz and pulse length of 0.07 μs. For field measurements with the Phantom IV, a flight was made over Guanabara bay at the same altitude as the radar antenna, with an average speed of 8 m/s. Besides, the measurement was performed for $P_d = 1$, i.e., the UAS was present on the radar monitor screen in every antenna scan without tracking loss. After being detected by the radar, the maximum detection distance for this drone model was evaluated. Figure 3.6 shows the flight area in yellow, as well as the Santos Dumont airport's (red circle) and the UFF's (blue circle) location. It is important to cite that because of the proximity between the flight area and the airport, regarding the safety and security, there were some limitations in flight altitude and distance.

3.4 Numerical Results

Figure 3.7 shows the simulated RCS values of the Phantom IV, in dBsm, as a function of the angle of incidence of the plane waves. Note that the highest RCS values occur when $\phi = 90°$ and $\phi = 270°$, which correspond to cases in which the UAS has one of its sides facing the radar direction. Considering equiprobability of occurrence for all values of ϕ, the arithmetic mean of all RCS values will be adopted in the remainder of this section.

Figure 3.6: Flight area's, Santos Dumont airport's and UFF's location.

This value is approximately -15.28 dBsm or 0.0296 m^2.

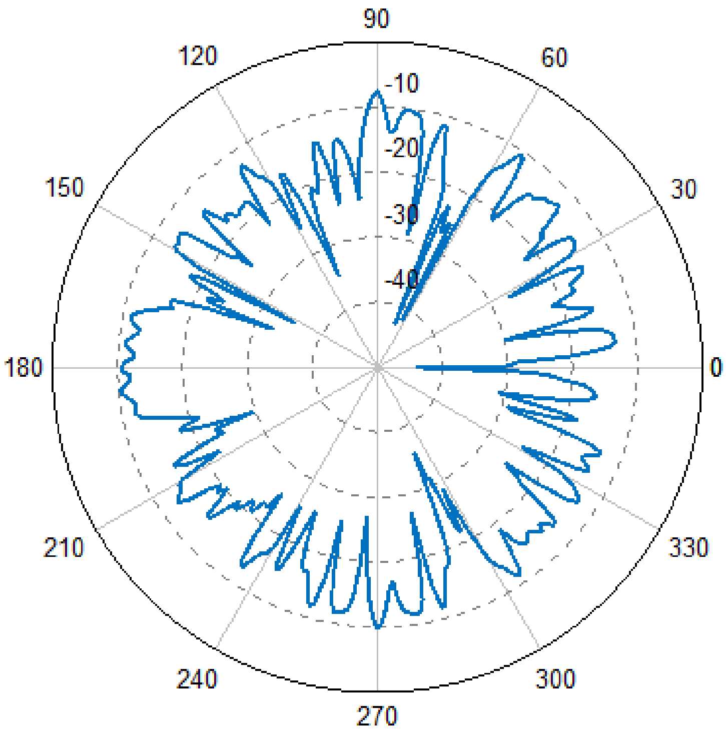

Figure 3.7: DJI Phantom IV's RCS (σ), in dBsm, as function of ϕ.

With the previously estimated RCS value, it is possible to analyze the UAS's P_d as a function of the maximum detection distance using the two methods presented in Section 3.2. Figure 3.8 shows the comparison between the two methods used.

Analyzing Figure 3.8, for Method I, note that the detection distance of the Phantom IV decreases with increases in L_s and P_d. Assuming $P_d = 0.9$, we have $R_{\max} = 1025$ m when $L_s = 15$ dB and $R_{\max} = 730$ m if $L_s = 21$ dB. Yet, for $P_d = 0.99$ and $L_s = 15$ dB, $R_{\max} = 570$ m. Considering $P_d = 0.5$ and $L_s = 11$ dB, it is, theoretically, possible to detect the DJI Phantom IV at $R_{\max} = 2082$ m.

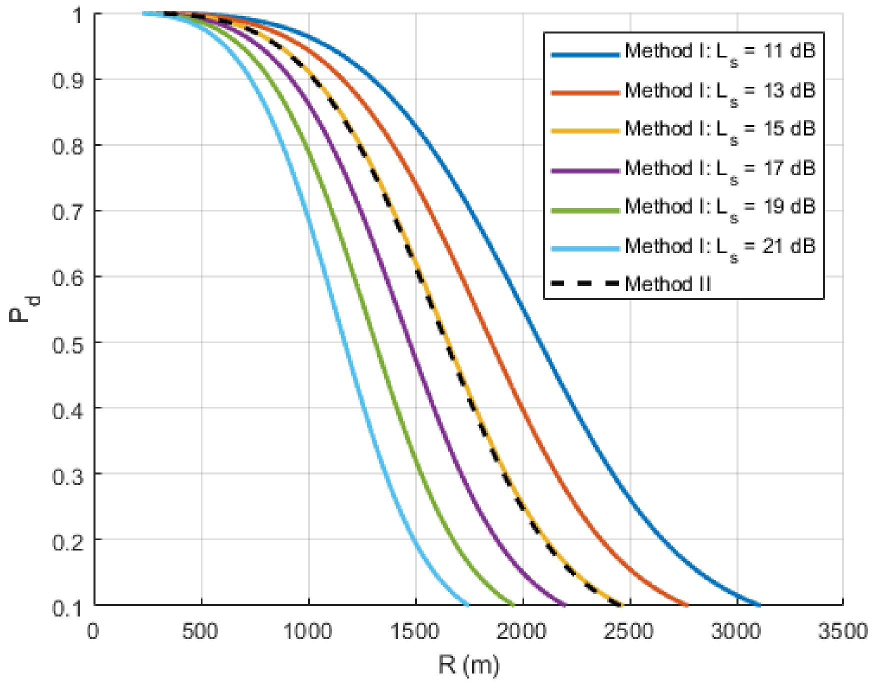

Figure 3.8: P_d as a function of distance, in meters, for Method I and II.

Using Method II, it is possible to observe that the Furuno FAR-2117 pulsed radar can detect the DJI Phantom IV up to $R_{\max} = 1000$ m away with $P_d = 0.9$, while distances greater than $R_{\max} = 2000$ m between the radar and the UAS result in $P_d = 0.24$. Moreover, comparing the curves in Figure 3.8, the system loss value, L_s, that makes Method I closer to Method II is $L_s = 15$ dB, which was used as a parameter for the continuity of the results. The error, in this case, calculating as the ratio between the difference from both curves and $R_{\max}$ from Method I, was $0,59\%$ and constant during each point of the curve.

Therefore, for the radar range simulation in AREPS, data from Table 3.1 were used, $\sigma = 0.0296$ m^2 and $L_s = 15$ dB, considering yet σ for all elevation angles of the drone. Both Figure 3.9 and Figure 3.10 show the result of this simulation, being the former extracted from AREPS software and the latter created in Matlab software for better presentation, in which a graph of the UAS's P_d is presented, represented by color intervals, as a function of its height in relation to sea level, in meters, and detection range, also in meters.

Analyzing both the Figures, it can be seen that for $1 \geq P_d > 0.9$ and $h = 0$ m it is possible to detect the drone within approximately $R_{\max} = 1250$ m, although the highest concentration of red dots (i.e., $P_d > 0.9$) is in the region where $R_{\max} < 400$ m. Furthermore, if $R_{\max} = 800$ m, then it is possible to observe the UAS detection with $P_d > 0.9$ in the region where $h < 190$ m.

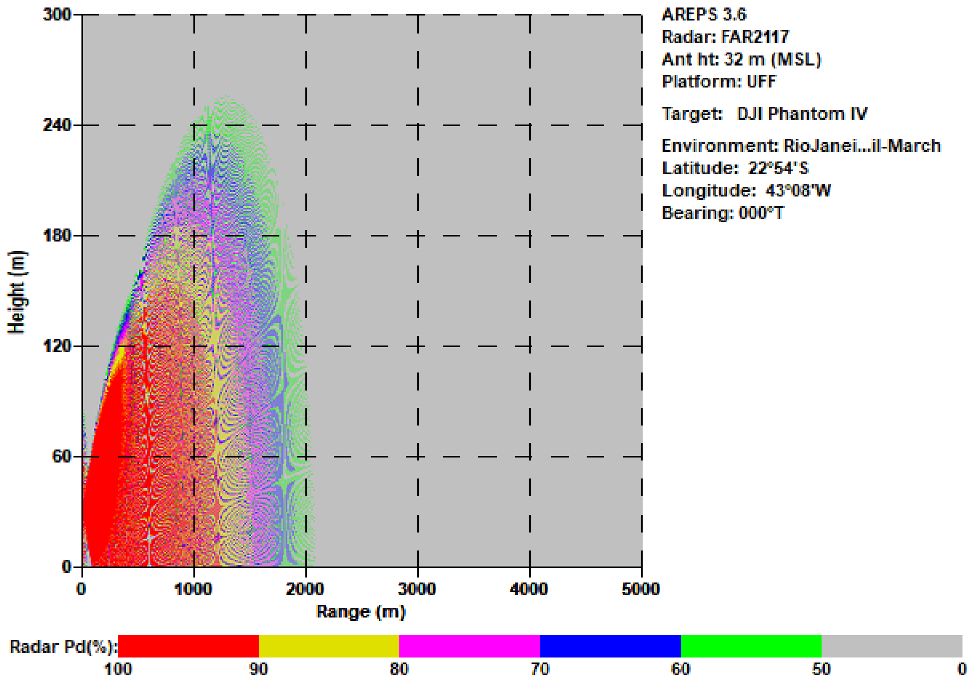

Figure 3.9: P_d as a function of the height in relation to sea level and detection distance with $\sigma = 0,0296\text{m}^2$ e $L_s = 15$ dB extracted from AREPS software.

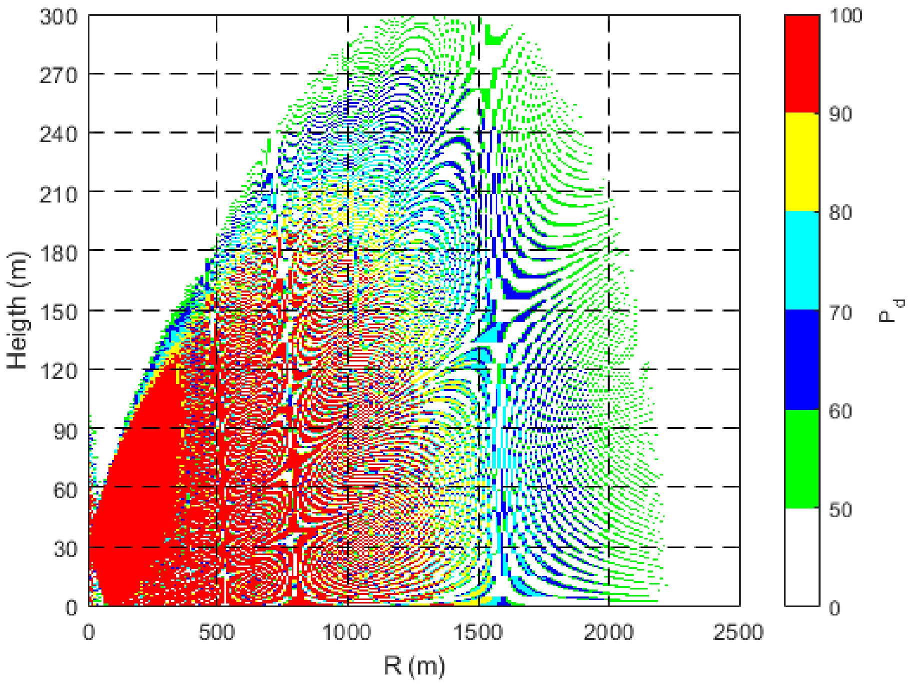

Figure 3.10: P_d as a function of the height in relation to sea level and detection distance with $\sigma = 0,0296\text{m}^2$ e $L_s = 15$ dB created in Matlab software.

To compare with the simulations carried out previously, a field measurement was performed using the FAR-2117 radar and the DJI Phantom IV, as described in Section 3.3.

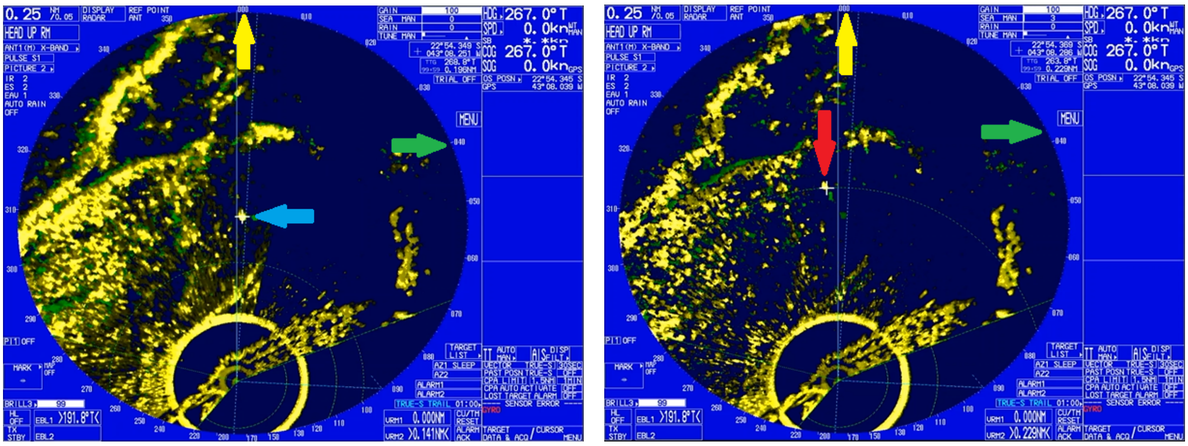

Figure 3.11: Phantom IV tracking on FAR-2117 radar monitor. The blue arrow indicates the first detection and the red arrow indicates the maximum detection. The yellow and green arrows represent, respectively, the directions in which Santos Dumont airport and the Rio-Niterói bridge are located.

Figure 3.11 shows drone tracking by the radar monitor, where the blue arrow shows the point of first detection of the aircraft at approximately 363 m away and the red arrow indicates the maximum distance that it was possible to track the target on the radar at approximately 425 m. Additionally, the green and yellow arrows indicate the direction of the Rio-Niterói bridge and the Santos Dumont airport, respectively. Moreover, Figure 3.12 illustrates the Phantom IV's trajectory during the flight and its first and maximum detection location.

Figure 3.12: Phantom IV's trajectory during flight. The Orange mark represents the radar location. The blue mark represents the first detection range and the red mark represents the maximum detection range.

The difference between the maximum detection range in simulations (597 m using Method I and II and about 400 m using AREPS) and the real measurement (425 m) is due to two factors. The first one is the increase in the system loss because it was used 80 m more cables for the radar installation than the described in the radar installation manual. This led to a radar performance degradation. The second one is the statistical nature of the RCS of complex target such the DJI Phantom IV. Once it was used a deterministic value (mean) to represent the UAS RCS in the simulations, then all the effects of the RCS variation were avoided. Furthermore, it was observed during the measurements that, depending on the direction of the drone in relation to the radar, its echo would become intermittent due to the oscillations of the RCS with the azimuth angle. Furthermore, it was possible to notice that the speed of the drone also caused a loss of energy in the echo. For a speed above 13 m/s it was not possible to identify the drone on the radar monitor.

Finally, based on simulations and field measurements, it can be stated that it is possible to detect a drone with low RCS that lies at the boundary between the Resonance and the Optic regions using an X-band pulsed radar, originally designed for maritime vessels. Therefore, and because it is a radar in common use in the Brazilian Navy, the use of this type of radar to detect drones could take advantage of an existing infrastructure and, consequently, reduce costs with installation or even acquisition of other radars for that purpose.

3.5 Summary

This chapter discussed the use of the Furuno FAR 2117 pulsed radar, normally used in maritime navigation, for detecting the DJI Phantom IV quadcopter. Simulations of RCS, radar range, and detection probability were carried out for this type of UAS. Furthermore, field measurements were made to prove the results obtained via simulation. Based on the numerical results, it was possible to observe that the radar specifications were sufficient to detect the drone, as indicated by the simulations. In field measurements, it was shown that the radar used was able to detect the drone, with a high probability of detection, at a maximum distance of 425 m. Finally, it was discussed that the difference between the maximum detection distances in the simulations and measurements was due to the use of more cables to install the radar, increasing the system losses, and the use of the RCS value as a constant instead of a random variable.

Chapter 4

Statistical Analysis and Modeling of UAS's Radar Cross-Section

The advent of UASs has revolutionized various fields, including military, surveillance and civilian applications. These aircraft exist in diverse shapes and sizes and their classification is often based on weight. ANAC [73] classifies them into three main categories with respect to their take-off weight, as shown in Table 4.1. However, in operational scenarios, where determining the UASs weight becomes impractical, such as in a war or urban areas, it is still necessary to differentiate those several types of UASs. The importance of differentiating between drones in these environments is underscored by the concept of RCS [74]. In modern warfare, accurate RCS differentiation enables military forces to minimize the risk of misidentification and facilitate targeted responses. In urban areas, where airspace is congested, distinguishing between drones of various sizes and capabilities becomes essential for safety and security. Thus, understanding and differentiating RCS values is vital for military operations, surveillance, and airspace management.

Table 4.1: ANAC's UAS classification by take-off weight.

Category	**Take-off weight**	**Models**
Class 3	≤ 25 kg	DJI Phantom series, DJI Mavic
Class 2	> 25 kg and ≤ 150 kg	Ehang184, DJI FlyCart 30
Class 1	> 150 kg	MQ-9 Reaper, RQ-4 Global Hawk

Unlike geometric targets such as spheres and corner reflectors, which have a deterministic value for the RCS, the RCS of real and complex targets, such as the UASs, may not be effectively modeled as a single constant [28]. For these targets, RCS strongly varies with azimuth and elevation angles, frequency, and polarization of the radar transmitter and receiver parts. As a consequence, RCS must be estimated by fitting an RCS dataset's histogram to distinct probability distributions [75]. This statistical analysis leads to statistical models, which can be of utmost importance for precisely investigating the RCS impact on radar detection.

In this context, the present chapter has the following contributions:

- A statistical analysis and modeling of the RCS of 9 different UASs, using three criteria: LLK, AIC, and BIC.
- A comparison of the simulated and measured RCS values for the DJI Phantom IV drone, showing the agreement between them and validating the simulation method.
- An evaluation of the impact of RCS modeling on the radar detection range, showing how different probability distributions affect the performance of a radar system.
- An analysis of the mean values of the RCS values when changing the operating frequency of a radar system and the elevation angle of the target.

The remainder of this work is organized as follows: Section 4.1 formulates the problem of considering UAS's RCS as a constant value and provides the motivation for this chapter. In the sequel, Section 4.2 introduces the mathematical formulation of the three statistical criteria used to measure the fit of the function in three different RCS datasets. Section 4.3 shows the materials and methods used in this chapter. More specifically, it presents the UASs used for test and simulation and the methods used to create each RCS dataset, as well as the RCS dataset measured provided by [29]. Furthermore, it also introduces the method to choose the best function to model each RCS dataset. In Section 4.4, the numerical results and statistical analysis of the different RCS datasets are discussed. Finally, Section 4.5 presents the final remarks of Chapter 4.

4.1 Problem Formulation

As discussed in Subsection 2.2.2, RCS is a crucial parameter for radar detection, as it measures the reflectivity of targets and plays a pivotal role in determining their detectability by radar systems. It depends on factors such as the size, shape, and composition of the target, as well as the frequency of the incident electromagnetic wave [27]. Basically, targets with high RCS are more reflective and easier for radar systems to detect, whereas targets with low RCS are less reflective and harder to detect. Furthermore, targets with complex structure and geometry have a unique RCS signature that can be used for the identification of the target [75].

In this context, many works are focusing on studying the RCS of UASs. For example, [76] investigated the influence of a small fixed-wing UAS's RCS on the detection range of an anti-drone system. Simulations of drone monostatic RCS were performed using real parameters from two radars, with operating frequencies of $8.70-9.65$ GHz and $3-16$ GHz. They found out that the UAS's mean RCS value were -17.62 dBsm and -22.77 dBsm each, achieving a detection range of 1784 m. In [77], the authors measured and analyzed the monostatic RCS of nine different types of drones in an anechoic chamber, with frequencies ranging from 26 GHz to 40 GHz. They showed that drones made of carbon fiber are easier to detect than those made of plastic and styrofoam. In [78], a drone classification was proposed using the monostatic RCS dataset provided by [77]. The classification through the drone's RCS signature was made by a new deep learning technique, called long short-term memory-adaptive learning rate optimizing (LSTM-ALRO). Accordingly, it was possible to achieve 99.88% of detection accuracy compared to the existing drone classification model. Moreover, [79] analyzed the RCS statistical properties of nine different commercial drones. To perform such an analysis, they measured their monostatic RCS in an anechoic chamber at 9 GHz. According to them, the RCS behavior of investigated drones is more in agreement with a random variable than a single constant number.

In general, previous works investigated the empirical values of RCS by solely measuring and analyzing them in deterministic terms. To the best of the authors' knowledge, the statistical analysis and modeling of UASs' RCS have not been thoroughly explored in the literature. Therefore, this work proposes a statistical approach to model the RCS of nine different UASs, employing a probability distribution that provides the best agreement with the histogram of the simulated and measured RCS dataset. Two RCS datasets were generated by simulations performed with Feko® software, and one RCS dataset was measured in an anechoic chamber and provided by [29]. Finally, but not least, comparative analyses between the chosen probability distribution and the RCS datasets are provided, in addition to an evaluation of the radar detection range.

4.2 Mathematical Formulation

In this chapter, three statistical criteria are used to perform probability distributions selection: LLK, AIC, and BIC.

Maximum Likelihood Estimation (MLE) is a method of estimating the parameters ($\boldsymbol{\theta}$) of an assumed probability distribution, given some observed data ($\boldsymbol{x}$). This is achieved by maximizing a likelihood function so that, under the assumed probability distribution, the observed data are most probable. In other words, the parameters of each probability distribution are varied, and the one with the maximum likelihood score, in relation to the histogram generated with the samples of the simulated RCS, is selected [80]. Defining $\mathcal{S}_{rv} = \{pd_0, pd_1, \dots, pd_{m-1}\}$ as the set of probability distributions, the likelihood of parameters $\boldsymbol{\theta_j} = \{\theta_{j,0}, \theta_{j,1}, \theta_{j,2}, \dots, \theta_{j,k_j-1}\}$ of the j-th probability distribution in $\mathcal{S}_{rv}$, being m the number of probability distributions and k_j the number of parameters of the j-th probability distribution, considering an independent and identically distributed random sample data set $\boldsymbol{x} = \{x_0, x_1, x_2, \dots, x_{n-1}\}$, is given by

$$\mathcal{L}(\boldsymbol{\theta_j}) = \prod_{i=0}^{n-1} f(\boldsymbol{\theta_j}|x_i), \tag{4.1}$$

$\forall j \in \{0, 1, \dots, m-1\}$, where $f(\boldsymbol{\theta_j}|x_i)$ is the likelihood of parameters $\boldsymbol{\theta_j}$ for a single outcome $x_i \in \boldsymbol{x}$. In practice, it is often convenient to work with the natural logarithm of the likelihood function, called the LLK, which can be expressed as

$$\mathrm{LLK}(\boldsymbol{\theta_j}) = \ln\{\mathcal{L}(\boldsymbol{\theta_j})\} = \sum_{i=0}^{n-1} \ln\{f(\boldsymbol{\theta_j}|x_i)\}. \tag{4.2}$$

Since the logarithm is a monotonic function, the maximum of $\mathrm{LLK}(\boldsymbol{\theta_j})$ occurs at the same value of $\boldsymbol{\theta_j}$ as the maximum of $\mathcal{L}(\boldsymbol{\theta_j})$. Once $\mathrm{LLK}(\boldsymbol{\theta_j})$ is maximized, the parameters of the j-th probability distribution can be obtained through

$$\hat{\boldsymbol{\theta}}_{\boldsymbol{j}\,\mathrm{LLK}} = \arg\max_{\boldsymbol{\theta_j}} \mathrm{LLK}(\boldsymbol{\theta_j}). \tag{4.3}$$

MLE is a usual criterion to estimate the best probability distribution that fits the dataset. However, it does not consider the effect of overfitting the dataset. The fit of any model can be improved by increasing the number of parameters, but there is a trade-off in the increasing variance [80]. Overfitting can be considered by penalizing the complexity of the given probability distribution. AIC and BIC criteria take this in consideration for the j-th probability distribution in $\mathcal{S}_{rv}$, respectively, through

$$\mathrm{AIC}(\boldsymbol{\theta_j}) = -2\mathrm{LLK}(\boldsymbol{\theta_j}) + 2k_j \tag{4.4}$$

and

$$\mathrm{BIC}(\boldsymbol{\theta_j}) = -2\mathrm{LLK}(\boldsymbol{\theta_j}) + k_j \ln n, \tag{4.5}$$

$\forall j \in \{0, 1, \dots, m-1\}$, in which n is the number of samples of the dataset. As can be seen, for AIC and BIC, the penalty terms are $2k_j$ and $k_j \ln n$, respectively. This means that AIC puts larger penalty on probability distribution functions with a higher number of parameters, while BIC additionally penalizes those regarding the number of samples contained in the dataset. In general, the best probability distribution model is the one with either the lowest AIC or BIC score [75]. Thus, the j-th probability distribution parameters can be obtained by minimizing AIC and BIC scores, respectively, as

$$\hat{\boldsymbol{\theta}}_{\boldsymbol{j}\,\mathrm{AIC}} = \arg\min_{\boldsymbol{\theta_j}} \mathrm{AIC}(\boldsymbol{\theta_j}) \tag{4.6}$$

and

$$\hat{\boldsymbol{\theta}}_{\boldsymbol{j}\,\mathrm{BIC}} = \arg\min_{\boldsymbol{\theta_j}} \mathrm{BIC}(\boldsymbol{\theta_j}). \tag{4.7}$$

Since the actual score of the LLK, AIC and BIC criteria depend on the sample values of the dataset, it is often convenient to work with their normalized versions. This is achieved by

$$\overline{\mathrm{LLK}}(\hat{\boldsymbol{\theta}}_{\boldsymbol{j}\,\mathrm{LLK}}) = \frac{\mathrm{LLK}(\hat{\boldsymbol{\theta}}_{\boldsymbol{j}\,\mathrm{LLK}})}{\max\limits_{j} \mathrm{LLK}(\hat{\boldsymbol{\theta}}_{\boldsymbol{j}\,\mathrm{LLK}})}, \tag{4.8}$$

$$\overline{\mathrm{AIC}}(\hat{\boldsymbol{\theta}}_{\boldsymbol{j}\,\mathrm{AIC}}) = \frac{\mathrm{AIC}(\hat{\boldsymbol{\theta}}_{\boldsymbol{j}\,\mathrm{AIC}})}{\max\limits_{j} \mathrm{AIC}(\hat{\boldsymbol{\theta}}_{\boldsymbol{j}\,\mathrm{AIC}})}, \tag{4.9}$$

and

$$\overline{\mathrm{BIC}}(\hat{\boldsymbol{\theta}}_{\boldsymbol{j}\,\mathrm{BIC}}) = \frac{\mathrm{BIC}(\hat{\boldsymbol{\theta}}_{\boldsymbol{j}\,\mathrm{BIC}})}{\max\limits_{j} \mathrm{BIC}(\hat{\boldsymbol{\theta}}_{\boldsymbol{j}\,\mathrm{BIC}})}, \tag{4.10}$$

respectively. In the manner that it is obtained $\overline{\mathrm{LLK}}(\hat{\boldsymbol{\theta}}_{\boldsymbol{j}\,\mathrm{LLK}}) \in [0,1], \overline{\mathrm{AIC}}(\hat{\boldsymbol{\theta}}_{\boldsymbol{j}\,\mathrm{AIC}}) \in [-1,0]$, and $\overline{\mathrm{BIC}}(\hat{\boldsymbol{\theta}}_{\boldsymbol{j}\,\mathrm{BIC}}) \in [-1,0]$. For simplicity, (4.8), (4.9), (4.10) will be denoted, respectively, by $\overline{\mathrm{LLK}}_j$, $\overline{\mathrm{AIC}}_j$, and $\overline{\mathrm{BIC}}_j$ from now on. Thus, the best probability distribution, for each criterion, is the one with the best score, that is, $\overline{\mathrm{LLK}}_j = 1$, $\overline{\mathrm{AIC}}_j = -1$, or $\overline{\mathrm{BIC}}_j = -1$.

4.3 Materials and Method

In this section the methodology used is presented considering three different RCS datasets: Datasets I, II, and III. Datasets I and II are the simulated DJI Phantom IV RCS for, respectively, 9.41 GHz and a range of frequencies varying from 1 to 40 GHz. Dataset III is a RCS database, available in [81], of nine different UAS measured in an anechoic chamber, using frequencies varying from 26 to 40 GHz. Therefore, this section first introduces each UAS used and its characteristics. Then, it shows how each RCS dataset was obtained and, finally, it explains how it was done to choose the best fitting distribution function to model each dataset's histogram.

4.3.1 UAS under simulation and test for statistical analysis

For this thesis, nine different types of UASs were used: DJI Phantom IV, DJI Mavic Pro, DJI F450, DJI Matrice 100, Parrot AR.Drone, Helicopter Kyosho, HMF Y600, Walkera Voyager 4, and a custom-built hexacopter. Figure 4.1 shows the previously mentioned UASs, while Table 4.2 summarizes their dimensions and material compositions.

Figure 4.1: UAS under simulation and test for statistical analysis. From left to right and from up to down, the UASs are: DJI Phantom IV, DJI Mavic Pro, DJI F450, DJI Matrice 100, Parrot AR.Drone, Helicopter Kyosho, HMF Y600, Walkera Voyager 4, and a custom-built hexacopter.

The simulations were carried out only for DJI Phantom IV using the Feko® software from the Altair® company, as explained in the following subsections.

4.3.2 Dataset I

To create the RCS Dataset I, the simulations were performed assuming a horizontally polarized plane wave at 9.41 GHz (i.e., $\lambda = 0.0319$ m) and DJI Phantom IV was used as UAS under simulation. Moreover, the incidence of plane waves occurred in the far-

Table 4.2: UAS characteristics.

UAS	L (mm)	Material compound
DJI Phantom IV	diagonal, 350	plastic
DJI Mavic Pro	diagonal, 335	plastic
DJI F450	diagonal, 450	plastic
DJI Matrice 100	diagonal, 650	carbon fiber
Parrot AR.Drone	diagonal, 580	styrofoam
Helicopter Kyosho	length, 780	plastic
HMF Y600	diagonal, 600	carbon fiber
Walkera Voyager 4	diagonal, 465	carbon fiber
Hexacopter	diagonal, 900	carbon fiber

field region on the three-dimensional model of the UAS, as illustrated in Figure 4.2. The method used to simulate the samples of the drone's RCS was Ray Launching - Geometrical Optics (RL-GO) because $L > 10\lambda$ characterizes the Optics scattering region.

The assumed azimuth and elevation angles of the incident wave are, respectively, $\boldsymbol{\phi}^I = \{\phi_0^I, \phi_1^I, \ldots, \phi_{N^I-1}^I\}$ and $\boldsymbol{\alpha}^I = \{\alpha_0^I, \alpha_1^I, \ldots, \alpha_{M^I-1}^I\}$, where the index I represents the Dataset I and the indexes N^I and M^I represent the size of $\boldsymbol{\phi^I}$ and $\boldsymbol{\alpha^I}$, respectively. The RCS Dataset I is then defined as a matrix $\boldsymbol{\Sigma}^I \in \mathbb{R}^{M^I \times N^I}$, in which each line corresponds to a vector with RCS values for a single elevation angle and each column corresponds to a vector with RCS values for a single azimuth angle, as

$$\boldsymbol{\Sigma}^I = \begin{bmatrix} \sigma_{0,0}^I & \sigma_{0,1}^I & \cdots & \sigma_{0,N^I-1}^I \\ \sigma_{1,0}^I & \sigma_{1,1}^I & \cdots & \sigma_{1,N^I-1}^I \\ \vdots & & \ddots & \vdots \\ \sigma_{M^I-1,0}^I & \sigma_{M^I-1,1}^I & \cdots & \sigma_{M^I-1,N^I-1}^I \end{bmatrix}. \tag{4.11}$$

In this manner, the set of RCS values, called now Subdataset I, that will be analyzed and modeled in this chapter is given by $\boldsymbol{\sigma}_i^I \in \boldsymbol{\Sigma}^I \,|\, \boldsymbol{\sigma}_i^I = \{\sigma_{i,0}^I, \sigma_{i,1}^I, \ldots, \sigma_{i,N^I-1}^I\}$, with $i = 0, 1, \ldots, M^I - 1$, which corresponds to the i-th line of the matrix $\boldsymbol{\Sigma}^I$. In other words, each element of Subdataset I is composed by the simulated RCS values for every element of $\boldsymbol{\phi}^I$ and for one fixed element of $\boldsymbol{\alpha}^I$.

4.3.3 Dataset II

To create the RCS Dataset II, simulations were performed assuming a horizontally polarized plane wave at a range of frequencies varying from 1 to 40 GHz in steps of 1 GHz, and the DJI Phantom IV was also used as UAS under simulation. Additionally, in this

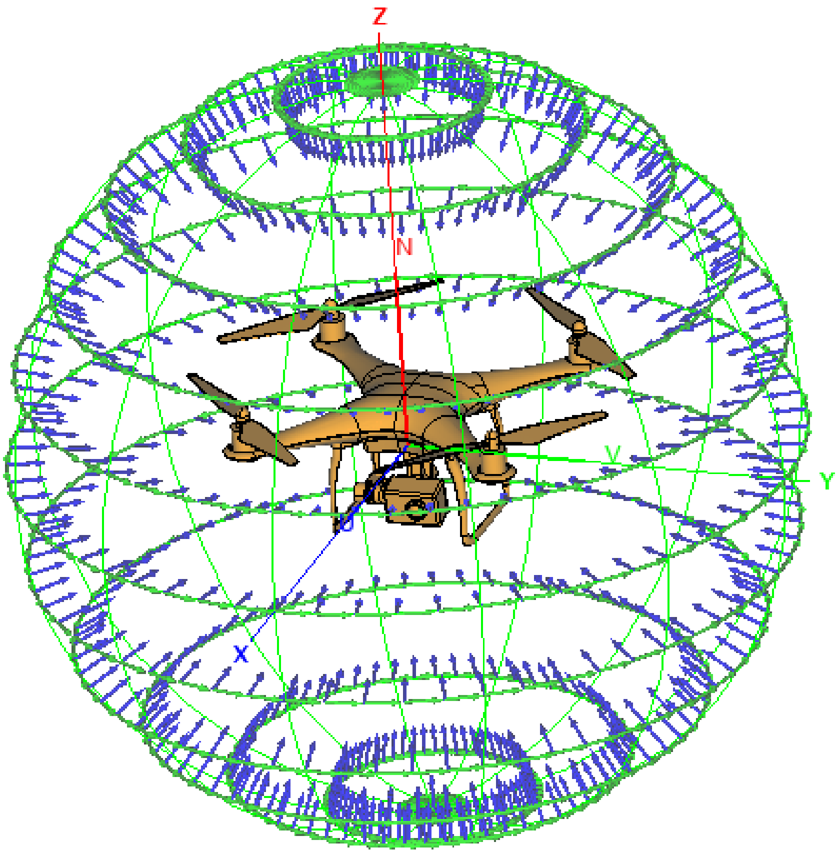

Figure 4.2: RCS simulation of DJI Phantom IV in Feko® for Dataset I.

simulation were considered a typical radar aperture of only 20°. Moreover, as in Dataset I, the incidence of plane waves occurred in the far-field region on the three-dimensional model of the UAS, as illustrated in Figure 4.3. The method used to simulate the samples of the drone's RCS was also Ray Launching - Geometrical Optics (RL-GO) as used in Dataset I.

The assumed frequencies and azimuth and elevation angles of the incident wave are, respectively, $\boldsymbol{f}^{II} = \{f_0^{II}, f_1^{II}, f_2^{II}, \ldots, f_{K^{II}-1}^{II}\}$, $\boldsymbol{\phi}^{II} = \{\phi_0^{II}, \phi_1^{II}, \ldots, \phi_{N^{II}-1}^{II}\}$ and $\boldsymbol{\alpha}^{II} = \{\alpha_0^{II}, \alpha_1^{II}, \ldots, \alpha_{M^{II}-1}^{II}\}$, where the index II represents the Dataset II and the indexes K^{II}, N^{II} and M^{II} represent the size of $\boldsymbol{f}^{II}$, $\boldsymbol{\phi}^{II}$ and $\boldsymbol{\alpha}^{II}$, respectively. N^{II} and M^{II} are the same for every simulated frequency. The RCS Dataset II is then defined as a matrix $\boldsymbol{\Sigma}_f^{II} \in \mathbb{R}^{M^{II} \times N^{II}}$, in which each line corresponds to a vector with RCS values for a single elevation angle and each column corresponds to a vector with RCS values for a single azimuth angle, for one frequency, $f \in \boldsymbol{f}^{II}$, as

$$\boldsymbol{\Sigma}_f^{II} = \begin{bmatrix} \sigma_{0,0}^{II} & \sigma_{0,1}^{II} & \cdots & \sigma_{0,N^{II}-1}^{II} \\ \sigma_{1,0}^{II} & \sigma_{1,1}^{II} & \cdots & \sigma_{1,N^{II}-1}^{II} \\ \vdots & & \ddots & \vdots \\ \sigma_{M^{II}-1,0}^{II} & \sigma_{M^{II}-1,1}^{II} & \cdots & \sigma_{M^{II}-1,N^{II}-1}^{II} \end{bmatrix}. \tag{4.12}$$

In this way, the set of RCS values that will be analyzed and modeled in this chapter, called now Subdataset II, is given by $\boldsymbol{\sigma}_{i,f}^{II} \in \boldsymbol{\Sigma}_f^{II} \,|\, \boldsymbol{\sigma}_{i,f}^{II} = \{\sigma_{i,0}^{II}, \sigma_{i,1}^{II}, \ldots, \sigma_{i,N^{II}-1}^{II}\}$, with $i = 0, 1, \ldots, M^{II} - 1$, which corresponds to each line of the matrix $\boldsymbol{\Sigma}_f^{II}$ for a single frequency, $f \in \boldsymbol{f}^{II}$. In other words, each element of Subdataset II is composed by the simulated RCS values for every element of $\boldsymbol{\phi}^{II}$, for one fixed element of $\boldsymbol{\alpha}^{II}$, and for one frequency of $\boldsymbol{f}^{II}$.

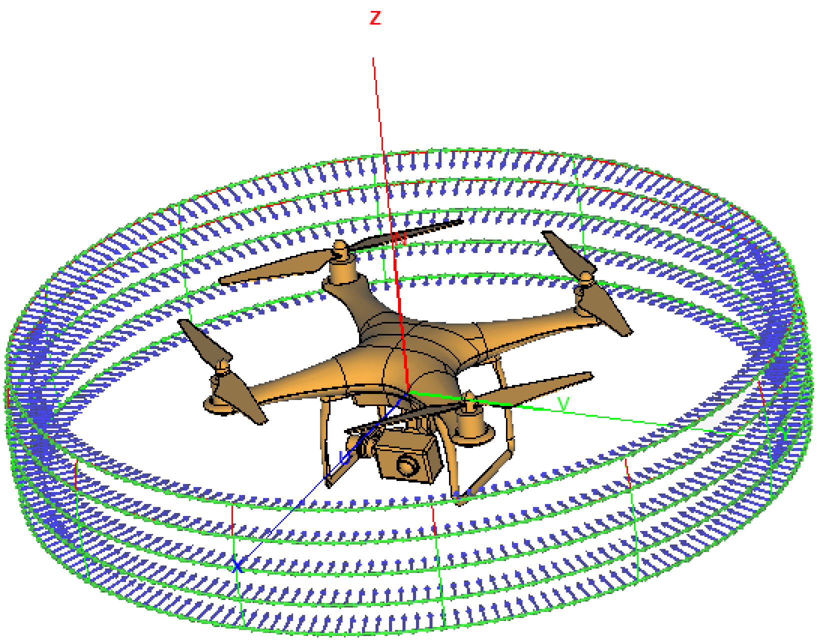

Figure 4.3: RCS simulation of DJI Phantom IV in Feko® for Dataset II.

4.3.4 Dataset III

For the Dataset III, measurements were made in an anechoic chamber at Aalto University, Finland, by [29], considering only horizontally polarized plane waves. The setup included transmitting (TX) and receiving (RX) antennas, vertically and horizontally polarized, on a mast, with frequencies varying from 26 to 40 GHz in an increment of 1 GHz. A Vector Network Analyzer (VNA) served as both a signal generator and a recorder. Each drone model took approximately 5 hours to measure, necessitating two sessions, with and without a power amplifier on the TX path. Calibration involved connecting the TX and RX ports through a 20 dB attenuator, compensating for losses in cables and equipment, and establishing a reference signal level.

The UASs used were placed on a rotating pillar on the opposite side of the antennas, initially with its bottom facing the antennas. There are two rotating axes: the azimuth (θ-axis) and the center-axis (ϕ-axis), as shown in Figure 4.4 [29]. The angular parameters were defined as $\theta \in [-90°, 90°]$ and $\phi \in [0°, 180°]$, with increments of 1°. By rotating the θ-axis and the ϕ-axis is obtained the measurements from the bottom hemisphere, illustrated in Figure 4.5, simulating radar exposure from a ground-based station. The distance between the antennas and the UASs was 5.8 m, maintaining a focus on half of the sphere to reduce measurement time while capturing crucial azimuth and elevation angle information [29].

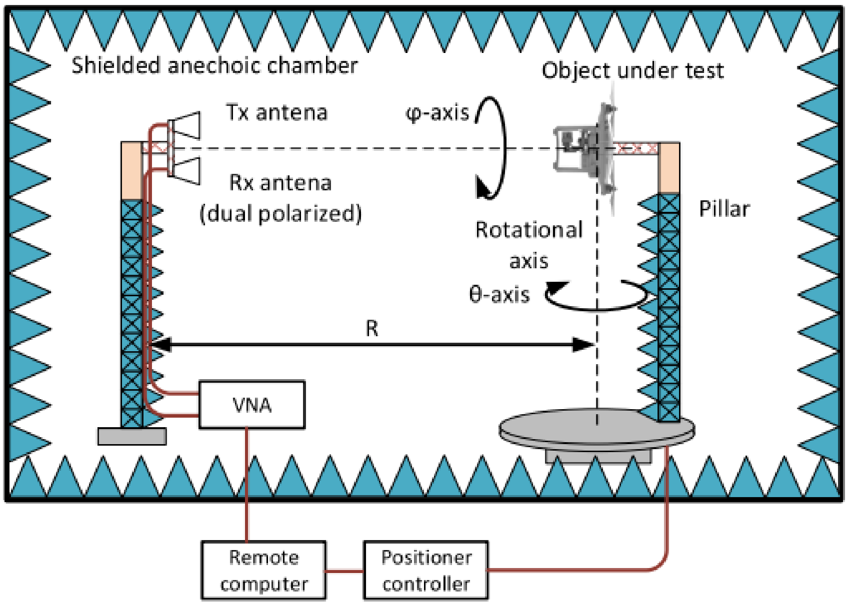

Figure 4.4: Schematic view of the measurement setup [29].

For a better comparison with the Dataset I and II, consider, without loss of generality, that the assumed frequencies and azimuth and elevation angles of the incident wave are, respectively, $\boldsymbol{f}^{III} = \{f_0^{III}, f_1^{III}, f_2^{III}, \ldots, f_{K^{III}-1}^{III}\}$, $\boldsymbol{\phi}^{III} = \{\phi_0^{III}, \phi_1^{III}, \ldots, \phi_{N^{III}-1}^{III}\}$ and $\boldsymbol{\alpha}^{III} = \{\alpha_0^{III}, \alpha_1^{III}, \ldots, \alpha_{M^{III}-1}^{III}\}$, where the index III represents the Dataset III and the indexes K^{III}, N^{III} and M^{III} represent the size of $\boldsymbol{f}^{III}$, $\boldsymbol{\phi}^{III}$ and $\boldsymbol{\alpha}^{III}$, respectively. N^{III} and M^{III} are the same for every simulated frequency. The RCS Dataset III is then defined as a matrix $\boldsymbol{\Sigma}_f^{III} \in \mathbb{R}^{M^{III} \times N^{III}}$, in which each line corresponds to a vector with RCS values for a single elevation angle and each column corresponds to a vector with RCS values for

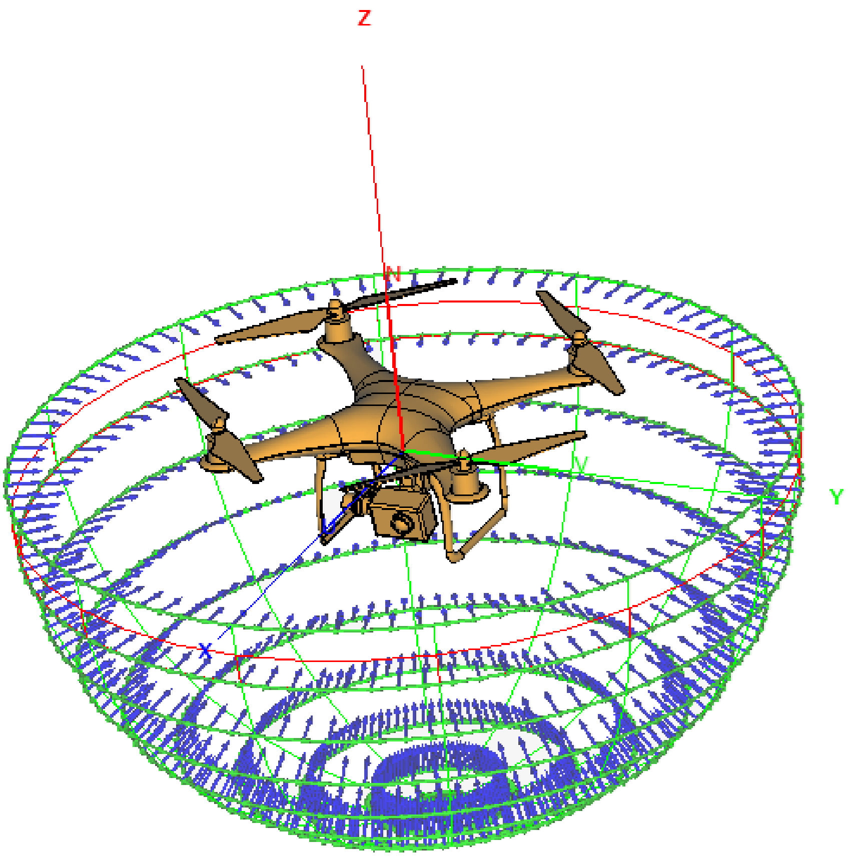

Figure 4.5: Illustration of the azimuth and elevation angles considered in the measurement.

a single azimuth angle, for one frequency, $f \in \boldsymbol{f}^{III}$, as

$$\boldsymbol{\Sigma}_f^{III} = \begin{bmatrix} \sigma_{0,0}^{III} & \sigma_{0,1}^{III} & \cdots & \sigma_{0,N^{III}-1}^{III} \\ \sigma_{1,0}^{III} & \sigma_{1,1}^{III} & \cdots & \sigma_{1,N^{III}-1}^{III} \\ \vdots & & \ddots & \vdots \\ \sigma_{M^{III}-1,0}^{III} & \sigma_{M^{III}-1,1}^{III} & \cdots & \sigma_{M^{III}-1,N^{III}-1}^{III} \end{bmatrix}. \tag{4.13}$$

Thus, the set of RCS values that will be analyzed and modeled in this chapter, now called Subdataset III, is given by $\boldsymbol{\sigma}_{i,f}^{III} \in \boldsymbol{\Sigma}_f^{III} \,|\, \boldsymbol{\sigma}_{i,f}^{III} = \{\sigma_{i,0}^{III}, \sigma_{i,1}^{III}, \ldots, \sigma_{i,N^{III}-1}^{III}\}$, with $i = 0, 1, \ldots, M^{III} - 1$, which corresponds to each line of the matrix $\boldsymbol{\Sigma}_f^{III}$ for a single frequency, $f \in \boldsymbol{f}^{III}$. In other words, each element of Subdataset III is composed by the measured RCS values for every element of $\boldsymbol{\phi}^{III}$, for one fixed element of $\boldsymbol{\alpha}^{III}$, and for one frequency of $\boldsymbol{f}^{III}$.

4.3.5 Choosing the best fitting distribution function

The set of probability distributions, $\mathcal{S}_{rv}$ = {*Exponential, Gamma, Generalized Extreme Value, Generalized Pareto, Log-normal, Nakagami, Rayleigh, Rician, Weibull*}, were chosen to represent random variables statistically belonging to $\mathbb{R}_+$ and because they are commonly used in the telecommunications field. In this regard, the statistical modeling is performed as follows for each Subdataset (the Subdataset superscript is omitted) and each frequency tone:

- **Step 1**: Select α_i, defining a unique RCS subdataset $\boldsymbol{\sigma}_{i,f}$ for modeling with a fixed elevation angle and only one frequency.
- **Step 2**: For each S_{rv} element, calculate $\overline{\mathrm{LLK}_j}$, $\overline{\mathrm{AIC}_j}$, and $\overline{\mathrm{BIC}_j}$ scores through Equations (4.8), (4.9), and (4.10), respectively.
- **Step 3**: Evaluate the number of occurrences of i) $\overline{\mathrm{LLK}_j} = 1$, ii) $\overline{\mathrm{AIC}_j} = -1$, and iii) $\overline{\mathrm{BIC}_j} = -1$. These are denoted $N_{\mathrm{LLK}_j}, N_{\mathrm{AIC}_j}$, and N_{BIC_j}, respectively, for the j-th probability distribution. They are incremented for each α_i.
- **Step 4**: Return to Step 1 for another not previously selected α_i, until there is unused $i \in \{0, 1, \ldots, M-1\}$. This step occurs M times.
- **Step 5**: Calculate the relative frequencies $R_{\mathrm{LLK}_j} = N_{\mathrm{LLK}_j}/M$, $R_{\mathrm{AIC}_j} = N_{\mathrm{AIC}_j}/M$, and $R_{\mathrm{BIC}_j} = N_{\mathrm{BIC}_j}/M$.
- **Step 6**: Evaluate the average relative frequencies $R_{avg_j} = (R_{\mathrm{LLK}_j} + R_{\mathrm{AIC}_j} + R_{\mathrm{BIC}_j})/3$.
- **Step 7**: The probability distribution chosen to model the Subdatasets for every element of $\boldsymbol{\alpha}$ and only one frequency is the one with the highest $R_{avg_j}, \forall j \in \{0, 1, \ldots, m-1\}$ associated with the set $\mathcal{S}_{rv}$.

4.4 Numerical Results

In this section, the results of the statistical analysis and modeling of the three RCS subdatasets are presented. Subsection 4.4.1 discusses the Dataset I created by simulation using a 3D model of the DJI Phantom IV for a horizontally polarized wave at 9.41 GHz. Subsection 4.4.2 brings the results of the analysis of Dataset II created, also, by simulation using DJI Phantom IV 3D model, but for a horizontally polarized wave ranging from 1 GHz to 40 GHz. Finally, in Subsection 4.4.3, the results for Dataset III are presented.

Additionally, for this section, the probability distributions used for fitting, analysis and presented in figures and tables are number as follows:

1. Exponential
2. Gamma
3. Generalized Extreme Value
4. Generalized Pareto
5. Log-normal
6. Nakagami
7. Rayleigh
8. Rician
9. Weibull

The PDFs and cumulative distribution functions (CDFs) of these probabilities distributions are provided in Appendix A.

4.4.1 Dataset I

The RCS simulation assumed $\boldsymbol{\phi}^I = \{0°, 2°, 4°, \ldots, 358°\}$ and $\boldsymbol{\alpha}^I = \{-90°, -85°, -80°, \ldots, 90°\}$. To analyze the impacts of RCS modeling in Equation (2.22), Furuno FAR-2117 radar specifications were considered as described in Table 3.1 with $L_s = 15$ dB.

Table 4.3 shows the normalized scores achieved by each probability distribution, for α_i^I varying in steps of 10° for a better presentation. The colored cells represent the best probability distribution for each criterion, being the yellow ones for $\overline{\mathrm{LLK}_j}$, green ones for $\overline{\mathrm{AIC}_j}$ and blue ones for $\overline{\mathrm{BIC}_j}$.

Note that for LLK, the best fitting is the Generalized Pareto probability distribution. However, when the penalizing factor for the number of parameters in AIC and BIC are introduced, the Generalized Pareto function presents a worst fit than the Exponential probability distribution in both criteria. This occurs due to the lower number of parameters in the latter distribution. Figure 4.6 shows the relative frequency of all probability distributions for each criterion. Observe that, for the Generalized Pareto distribution,

Table 4.3: $\overline{\text{LLK}_j}$, $\overline{\text{AIC}_j}$ and $\overline{\text{BIC}_j}$ scores for each probability distribution at some elevation angles.

Probability Distributions		Elevation Angle (α^I)																		
		-90°	-80°	-70°	-60°	-50°	-40°	-30°	-20°	-10°	0°	10°	20°	30°	40°	50°	60°	70°	80°	90°
1	$\overline{\text{LLK}_1}$	-0.244	0.921	0.999	0.967	0.990	0.983	0.965	0.982	0.999	0.998	0.999	0.999	0.991	0.982	0.997	0.994	0.994	0.989	-0.595
	$\overline{\text{AIC}_1}$	0.246	-0.931	-1	-0.969	-0.992	-0.985	-0.968	-0.984	-1	-1	-1	-1	-0.992	-0.986	-1	-0.999	-1	-0.996	0.602
	$\overline{\text{BIC}_1}$	0.249	-0.939	-1	-0.973	-0.995	-0.988	-0.971	-0.986	-1	-1	-1	-1	-0.995	-0.989	-1	-1	-1	-1	0.614
2	$\overline{\text{LLK}_2}$	0.984	0.973	1	0.999	1	0.998	0.997	0.997	0.999	0.998	1	0.999	1	0.988	0.997	0.994	0.995	0.999	0.965
	$\overline{\text{AIC}_2}$	-0.985	-0.978	-0.997	-0.999	-1	-0.998	-0.999	-0.997	-0.998	-0.998	-0.998	-0.998	-1	-0.990	-0.997	-0.997	-0.996	-1	-0.967
	$\overline{\text{BIC}_2}$	-0.987	-0.978	-0.992	-0.999	-1	-0.998	-1	-0.996	-0.995	-0.994	-0.996	-0.995	-1	-0.990	-0.994	-0.993	-0.990	-0.993	-0.971
3	$\overline{\text{LLK}_3}$	1	0.956	0.962	0.981	0.991	0.980	1	0.980	0.981	0.970	0.975	0.984	0.993	0.965	0.956	0.992	0.983	0.922	1
	$\overline{\text{AIC}_3}$	-1	-0.955	-0.956	-0.978	-0.989	-0.978	-1	-0.978	-0.978	-0.967	-0.973	-0.981	-0.991	-0.965	-0.953	-0.992	-0.981	-0.915	-1
	$\overline{\text{BIC}_3}$	-1	-0.944	-0.947	-0.974	-0.985	-0.975	-0.998	-0.975	-0.972	-0.960	-0.967	-0.976	-0.989	-0.963	-0.946	-0.984	-0.969	-0.897	-1
4	$\overline{\text{LLK}_4}$	0.684	1	0.999	0.986	0.993	0.999	0.977	0.999	1	1	0.999	1	0.994	1	1	1	1	1	0.447
	$\overline{\text{AIC}_4}$	-0.683	-0.999	-0.994	-0.983	-0.991	-0.998	-0.977	-0.997	-0.996	-0.997	-0.997	-0.997	-0.992	-1	-0.997	-1	-0.997	-0.994	-0.442
	$\overline{\text{BIC}_4}$	-0.681	-0.990	-0.985	-0.979	-0.987	-0.995	-0.975	-0.994	-0.990	-0.990	-0.991	-0.991	-0.990	-0.997	-0.990	-0.992	-0.985	-0.977	-0.435
5	$\overline{\text{LLK}}$	0.984	0.838	0.703	0.938	0.879	0.943	0.970	0.621	0.807	0.823	0.834	0.815	0.922	0.917	0.789	0.634	0.509	0.580	0.965
	$\overline{\text{AIC}}$	-0.985	-0.841	-0.699	-0.938	-0.879	-0.943	-0.971	-0.620	-0.805	-0.822	-0.832	-0.814	-0.921	-0.919	-0.788	-0.634	-0.506	-0.575	-0.967
	$\overline{\text{BIC}}$	-0.987	-0.838	-0.693	-0.937	-0.878	-0.943	-0.972	-0.618	-0.802	-0.818	-0.829	-0.810	-0.921	-0.919	-0.784	-0.628	-0.497	-0.563	-0.971
6	$\overline{\text{LLK}}$	0.984	0.782	0.955	0.975	0.984	0.980	0.969	0.985	0.987	0.944	0.953	0.987	0.979	0.950	0.975	0.946	0.980	0.945	0.964
	$\overline{\text{AIC}}$	-0.985	-0.784	-0.952	-0.975	-0.984	-0.980	-0.971	-0.985	-0.986	-0.943	-0.952	-0.986	-0.979	-0.951	-0.974	-0.949	-0.981	-0.945	-0.967
	$\overline{\text{BIC}}$	-0.987	-0.780	-0.947	-0.974	-0.984	-0.980	-0.971	-0.985	-0.983	-0.940	-0.949	-0.983	-0.979	-0.951	-0.971	-0.945	-0.975	-0.938	-0.971
7	$\overline{\text{LLK}_7}$	0.984	0.994	0.984	0.995	0.985	0.999	0.991	0.979	0.988	0.997	0.999	0.984	0.991	0.997	0.997	0.958	0.958	0.982	0.965
	$\overline{\text{AIC}_7}$	-0.985	-1	-0.981	-0.995	-0.985	-0.999	-0.993	-0.979	-0.987	-0.997	-0.997	-0.982	-0.991	-0.999	-0.997	-0.960	-0.959	-0.982	-0.967
	$\overline{\text{BIC}_7}$	-0.987	-1	-0.976	-0.995	-0.985	-0.999	-0.994	-0.978	-0.984	-0.993	-0.995	-0.980	-0.991	-1	-0.994	-0.956	-0.952	-0.975	-0.971
8	$\overline{\text{LLK}}$	-0.105	0.838	0.703	0.938	0.879	0.943	0.970	0.621	0.807	0.823	0.834	0.815	0.922	0.917	0.789	0.634	0.509	0.580	-0.270
	$\overline{\text{AIC}}$	0.107	-0.847	-0.702	-0.940	-0.881	-0.945	-0.973	-0.622	-0.807	-0.824	-0.834	-0.815	-0.923	-0.921	-0.790	-0.636	-0.509	-0.581	0.275
	$\overline{\text{BIC}}$	0.109	-0.854	-0.701	-0.944	-0.883	-0.947	-0.976	-0.622	-0.806	-0.824	-0.833	-0.815	-0.925	-0.924	-0.789	-0.635	-0.507	-0.579	0.283
9	$\overline{\text{LLK}_9}$	0.981	0.987	0.999	1	0.998	1	0.996	1	0.999	0.999	0.999	0.999	0.999	0.991	0.997	0.995	0.997	0.998	0.958
	$\overline{\text{AIC}_9}$	-0.982	-0.993	-0.997	-1	-0.998	-1	-0.998	-1	-0.998	-0.998	-0.998	-0.998	-0.999	-0.993	-0.997	-0.998	-0.998	-0.999	-0.960
	$\overline{\text{BIC}_9}$	-0.983	-0.992	-0.992	-1	-0.998	-1	-0.998	-1	-0.995	-0.995	-0.995	-0.995	-0.999	-0.993	-0.994	-0.994	-0.99	-0.992	-0.964

$R_{\text{LLK}_j} = 0.43$, $R_{\text{AIC}_j} = 0.16$, and $R_{\text{BIC}_j} = 0.08$, which gives $R_{avg_j} = 0.22$. On the other hand, the Exponential distribution has $R_{\text{LLK}_j} = 0$, $R_{\text{AIC}_j} = 0.35$, and $R_{\text{BIC}_j} = 0.46$, and thus $R_{avg_j} = 0.27$.

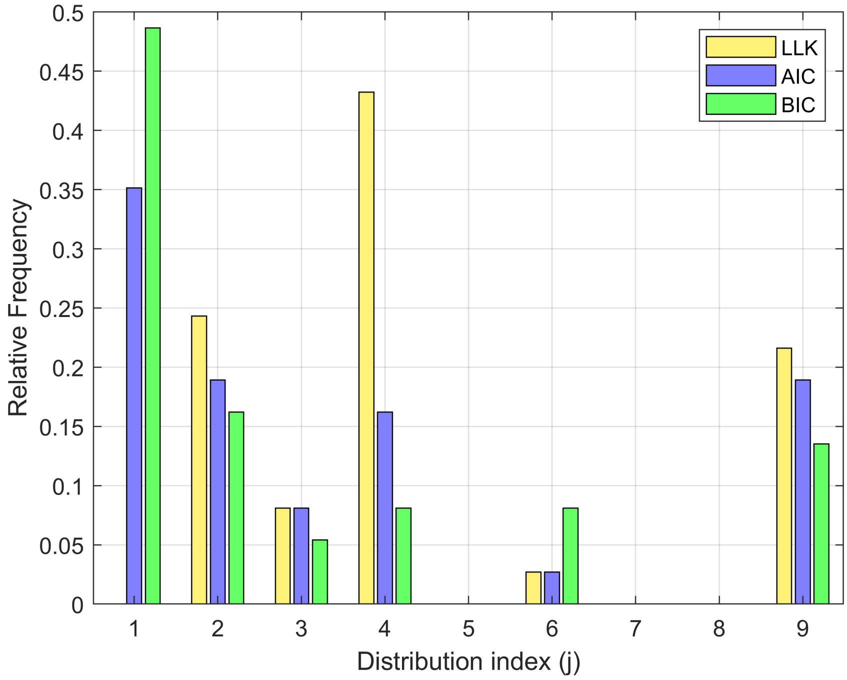

Figure 4.6: Relative frequency of each probability distributions for LLK, AIC, and BIC.

Once its average relative frequency was the highest, the Exponential probability distribution is chosen to model the entire RCS datasets' histogram for all elevation angles individually, i.e., each subdataset. However, it is important to note that some elevation angles of the incident wave are impractical, depending on the radar used. Although the RCS has been simulated for $\boldsymbol{\alpha}^I$ varying from -90° to 90°, typical maritime radars have 30° of beamwidth vertical aperture, corresponding to $\boldsymbol{\alpha}^I$ being bounded between -15° and 15°. Table 4.4 shows the parameter that defines the Exponential random variable γ for all simulated elevation angles.

To perform the analysis of the PDF and CDF of the Exponential probability distribution, the horizontal plane of the radar antenna corresponding to an elevation angle, $\alpha_{19}^I = 0°$, was used. Thus, Exponential's PDF, in function of x, is given by the following equation

$$f(x) = \begin{cases} \frac{1}{\gamma} e^{-\frac{x}{\gamma}} & , x \geq 0 \\ 0 & , x < 0 \end{cases}, \tag{4.14}$$

in which, $\gamma = 0.0284$ for $\alpha_{19}^I = 0°$. Figure 4.7 shows the Exponential PDF and the RCS dataset histogram for $\alpha_{19}^I = 0°$. Note that the RCS values, in the histogram, have a higher density for $\sigma_{19,j}^I \leq 0.01\ m^2$. Yet, from 0 m^2 to 0.03 m^2, the density decreases from 30 to 15, which corresponds approximately to a drop in 50%. Moreover, the higher $\sigma_{19,j}^I$, the lower the density, corresponding to a typical Exponential PDF characteristic.

The Exponential's CDF, also in function of x, is given by the following equation

$$F(x) = \begin{cases} 1 - e^{-\frac{x}{\gamma}} & , x \geq 0 \\ 0 & , x < 0 \end{cases}, \tag{4.15}$$

in which, $\gamma = 0.0284$ for $\alpha_{19}^I = 0°$. Figure 4.8 shows the curves of Exponential and Dataset I's CDFs, $F_{ds_I}(\sigma_{19,j}^I)$. Note that there is a probability of 0.9 or 90% for $x \leq 0.0655$ and $\sigma_{19,j}^I \leq 0.0652$, i.e. $F_{ds_I}(\sigma_{19,j}^I \leq 0.0652) = F(x \leq 0.0655) = 0.9$, which yields an error of $100 \times |x - \sigma_{19,j}^I|/\sigma_{19,j}^I = 100 \times |0.0655 - 0.0652|/0.0652 = 0.46\%$ between the RCS values. For $F_{ds_I}(\sigma_{19,j}^I \leq 0.0198) = F(x \leq 0.0199) = 0.5$, it results in an error of 0.5%. Yet, for $x = \sigma_{19,j}^I = 0.1m^2$, it can be seen that the Exponential and dataset CDFs yields 0.97 and 0.99 of probability, respectively, which correspond to 2% of difference.

One way to define whether a curve is well represented by another is through the linear

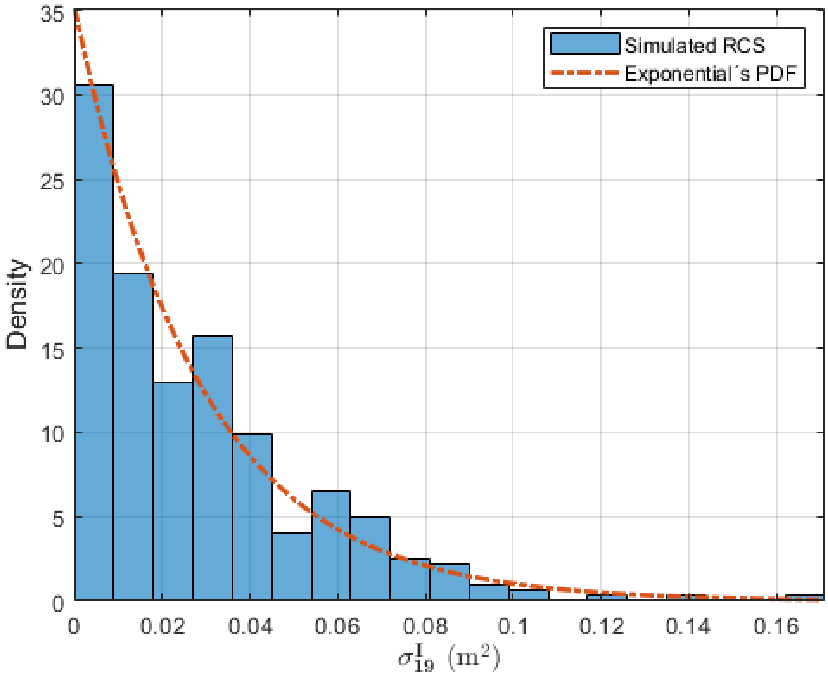

Figure 4.7: Histogram of simulated RCS values and PDF of the fitted Exponential distribution, when $\alpha_{19}^{I} = 0°$.

correlation, given by

$$c_{y,x} = \frac{\sum_{z=1}^{n}(F(y)_z - \overline{F(y)})(F(x)_z - \overline{F(x)})}{\sqrt{\sum_{z=1}^{n}(F(y)_z - \overline{F(y)})^2 \sum_{z=1}^{n}(F(x)_z - \overline{F(x)})^2}}, \tag{4.16}$$

in which $F(y)_z$ and $F(x)_z$ are the individual sample points indexed with z. $\overline{F(y)}$ and $\overline{F(x)}$ are the means of the $F(y)_z$ and $F(x)_z$ datasets, respectively. n is the total number of data points or observations. Equation (4.16) measures the strength and direction of the linear relationship between two variables. The value of $c_{y,x}$ lies between -1 and 1, where -1 indicates a perfect negative linear correlation, 1 indicates a perfect positive linear correlation, and 0 indicates no linear correlation. For the curves of Exponential and Dataset I's CDFs, it is obtained $c_{y,x} = 0.9965$.

To evaluate the impact of RCS modeling on Equation (3.1) and to compare the results shown in Figure 2.9, but now considering $L_s = 15$ dB, Figure 4.9 shows the curve with the assumed mean RCS values of the Section 3.4, $\sigma_1 = 0.0296$ m^2 and the curve with the RCS values of 50% probability of appearance, $\sigma_2 = 0.02$ m^2.

Note that, for $P_d = 0.99$, $\mathrm{R}_{\max} = 573$ m when used σ_1 as the drone RCS and $\mathrm{R}_{\max} = 520$ m when used σ_2, which leads to a difference of 50 m in detection range. Also, for a decrease in P_d it is observed that the difference in detection range is increased, reaching

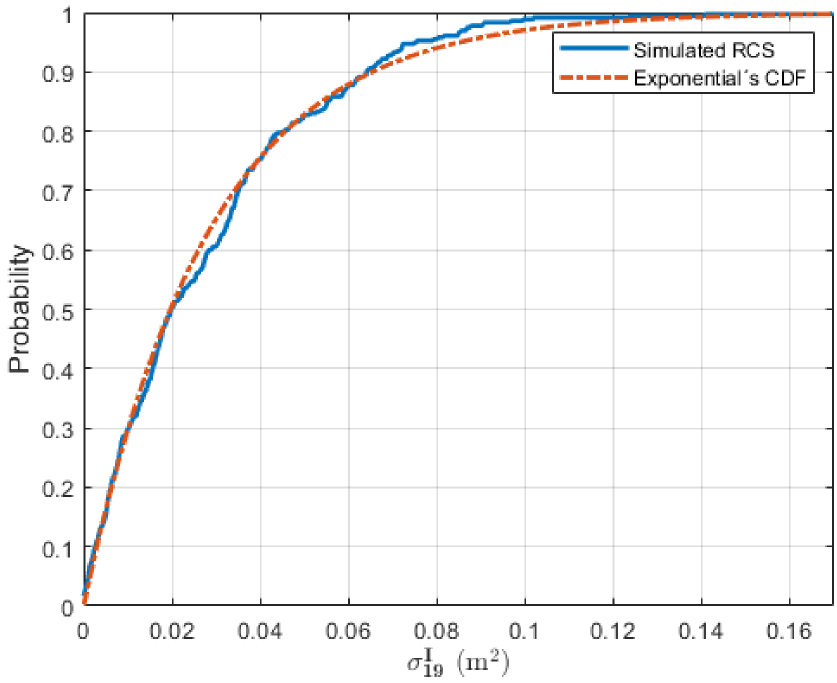

Figure 4.8: CDFs of the simulated RCS values and the fitted Exponential distribution, when $\alpha_{I,19} = 0°$.

197 m for $P_d = 0.2$.

Considering now the evaluation of the difference between the use of the simulated RCS values and the modeled RCS values in Equation (3.1), Figure 4.10 shows $\mathrm{R}_{\max}$ as a function of SNR, considering the parameters of the Furuno FAR-2117 radar presented in Table 3.1. These curves assume $\alpha_{19}^{I} = 0°$ and RCS values that satisfy $F(x \leq u) = F_{ds_I}(\sigma_{19,j}^{I} \leq v) = 0.1, 0.3, 0.5, \ldots, 0.9$, with $u \in \mathbb{R}$ and $v \in \boldsymbol{\sigma^{I}}$. Observe that for u and v that satisfies $F(x \leq u) = F_{ds_I}(\sigma_{19,j}^{I} \leq v) = 0.1$, 0.5, and 0.9, the curves are well-fitted, with an error less than 0.15%. The curve with the highest error, about 3.8%, occurs for $F(x \leq 0.0101) = F_{ds_I}(\sigma_{19,j}^{I} \leq 0.0101) = 0.3$. Note that increasing both F and F_{ds_I} corresponds to an increment in SNR, considering the same $\mathrm{R}_{\max}$.

4.4.2 Dataset II

For this dataset, the RCS simulation assumed $\boldsymbol{\phi}^{II} = \{0°, 2°, 4°, \ldots, 358°\}$, $\boldsymbol{\alpha}^{II} = \{-10°, -5°, 0°, 5°, 10°\}$, and the set of frequencies used as $\boldsymbol{f}^{II} = \{1, 2, 3, \ldots, 40\}$ GHz. Figure 4.11 shows the relative frequency for all probability distributions for each criterion and for $f_i^{II} = 10$ GHz (a), $f_i^{II} = 26$ GHz (b), $f_i^{II} = 33$ GHz (c), and $f_i^{II} = 39$ GHz (d).

Note that in (a), (b), and (c), even though the Exponential distribution does not

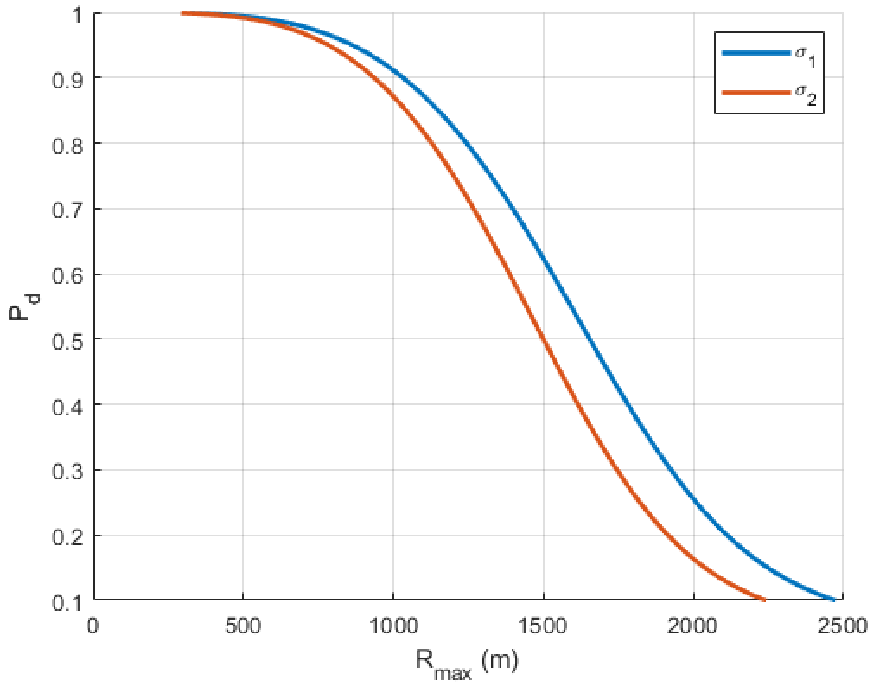

Figure 4.9: Pd as a function of distance, in meters, for $\sigma_1 = 0.0296$ m^2 from Chapter 3 and $\sigma_2 = 0.02$ m^2 from Chapter 4.

have an LLK score, it is the best-fit distribution, with $R_{avg_j} = 0.67$, $R_{avg_j} = 0.53$, and $R_{avg_j} = 0.27$, respectively. In (d), even when introduced the penalty terms of (4.4) and (4.5), the Log-normal distribution was the best-fit, with $R_{avg_j} = 0.47$. Furthermore, Table 4.5 shows the probability distribution functions with the highest average relative frequency for each simulated frequency. The probability distributions that appear the most are the Exponential, 23 times, followed by the Log-Normal, 11 times.

To perform the analysis of PDF and CDF of the two probability distributions that appear the most - Exponential and Log-normal -, consider $\alpha_2^{II} = 0°$ and x the random variable for the Exponential and Log-normal distributions. The PDF, $f(x)$, and CDF, $F(x)$, of the Exponential distribution are given by (4.14) and (4.15), respectively. For the Log-normal distribution, consider the following equations

$$f(x) = \frac{1}{x\gamma\sqrt{2\pi}} \exp\left(-\frac{(\ln x - \mu)^2}{2\gamma^2}\right) \tag{4.17}$$

and

$$F(x) = \frac{1}{2}\left[1 + \operatorname{erf}\left(\frac{\ln x - \mu}{\gamma\sqrt{2}}\right)\right], \tag{4.18}$$

in which $x > 0$, μ is the mean of the logarithm of the random variable, γ is the standard deviation of the logarithm of the random variable, and erf is the error function. (4.17)

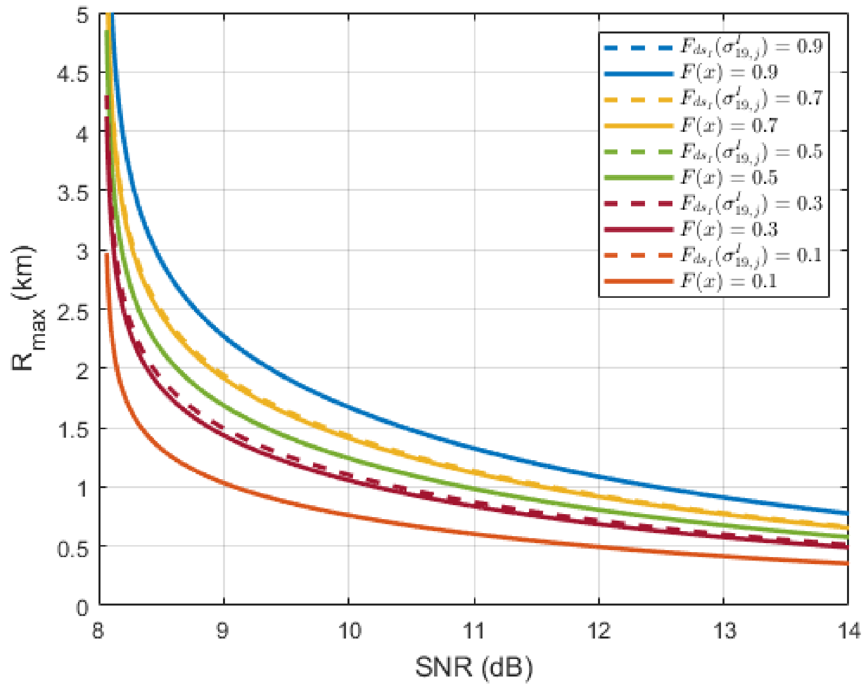

Figure 4.10: R_{max} as a function of SNR for some simulated RCS values.

and (4.18) are, respectively, the PDF and CDF of the Log-normal distribution.

Figure 4.12 shows the histogram of the simulated subdatasets of RCS values, $\boldsymbol{\sigma^{II}_{2,f}}$, for $\alpha_2^{II} = 0°$, and for $f_i^{II} = 10$ GHz (a), $f_i^{II} = 26$ GHz (b), $f_i^{II} = 33$ GHz (c), and $f_i^{II} = 39$ GHz (d) along the PDFs of the best-fit probability distribution for the mentioned frequencies.

Note that in (a) the highest densities are concentrated for $\sigma^{II}_{2,j} \leq 0.025$ m^2. In (b) and (d) the highest densities are concentrated for $\sigma^{II}_{2,j} \leq 0.05$ m^2. In (c), the highest densities are located for $\sigma^{II}_{2,j} \leq 0.1$ m^2. Moreover, to analyze the CDFs, observe Figure 4.13. It shows the curves of the CDF's simulated RCS, $F_{ds_{II}}(\sigma^{II}_{2,j,f})$, for $\alpha_2^{II} = 0°$, and for $f_i^{II} = 10$ GHz (a), $f_i^{II} = 26$ GHz (b), $f_i^{II} = 33$ GHz (c), and $f_i^{II} = 39$ GHz (d) along the CDFs of the best-fit probability distribution for the mentioned frequencies.

Figure 4.13 (a) shows that there is a probability of 0.9 or 90% for $\sigma^{II}_{2,j} \leq 0.0648$ m^2 and $x \leq 0.0613$ m^2, i.e. $F_{ds_{II}}(\sigma^{II}_{2,j} \leq 0.0648) = F(x \leq 0.0613) = 0.9$, that produces an error of $100 \times |x - \sigma^{II}_{2,j}|/\sigma^{II}_{2,j} = 100 \times |0.0613 - 0.0648|/0.0648 = 5.40\%$. Considering now $F_{ds_{II}}(\sigma^{II}_{2,j} \leq 0.0166) = F(x \leq 0.0184) = 0.5$, it results in an error of approximately 10.84%. Furthermore, the linear correlation, given by Equation (4.16), between both curves is $c_{y,x} = 0.9965$. In (b), $F_{ds_{II}}(\sigma^{II}_{2,j} \leq 0.1373) = F(x \leq 0.1539) = 0.9$ and $F_{ds_{II}}(\sigma^{II}_{2,j} \leq 0.0457) = F(x \leq 0.0457) = 0.5$ yield errors of approximately 12.1% and 0%,

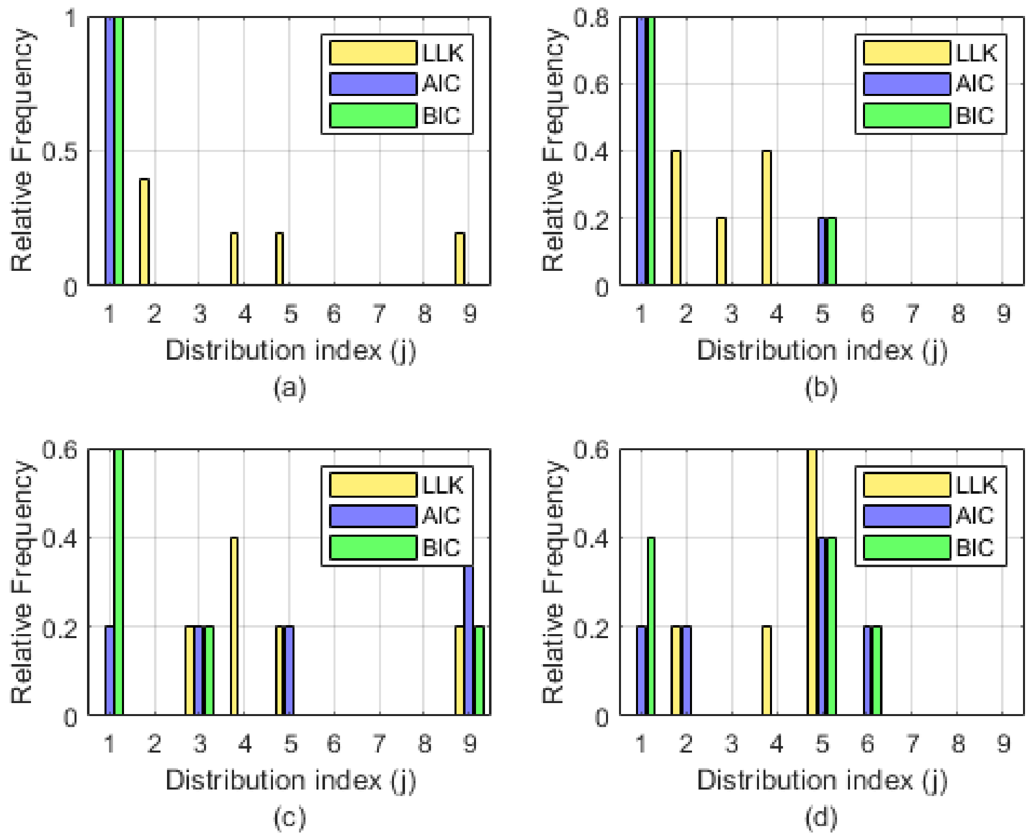

Figure 4.11: Relative frequency for (a) $f_i^{II} = 10$ GHz, (b) $f_i^{II} = 26$ GHz, (c) $f_i^{II} = 33$ GHz, and $f_i^{II} = 39$ GHz.

respectively. The linear correlation for these curves is $c_{y,x} = 0.9984$. When doing the same calculations as in (c) and (d), it results in errors of 7.7% and 57.0% for (c) and 26.2% and 14.7% for (d). The linear correlations between the curves in (c) and (d) are, respectively, 0.9937 and 0.9924.

In order to be reproducible, Table 4.6 provides the parameter values of each best-fit probability distribution for each frequency, f, and elevation angle, α_i^{II}.

4.4.3 Dataset III

This dataset, provided by [29], assumed $\boldsymbol{\phi}^{III} = \{0°, 2°, 4°, \ldots, 358°\}$, $\boldsymbol{\alpha}^{III} = \{-90°, -85°, -80°, \ldots, 0°\}$, and $\boldsymbol{f}^{III} = \{26, 27, 28, \ldots, 40\}$ GHz. Among the nine drone models measured, statistical analyzes will initially be performed for the DJI Phantom IV and the results for the other UASs models will be presented in the following subsection. Figure 4.14 shows the measured RCS of the DJI Phantom IV, for all frequencies. From left to right and from top to bottom, the frequencies increase from 26 to 40 GHz in step of

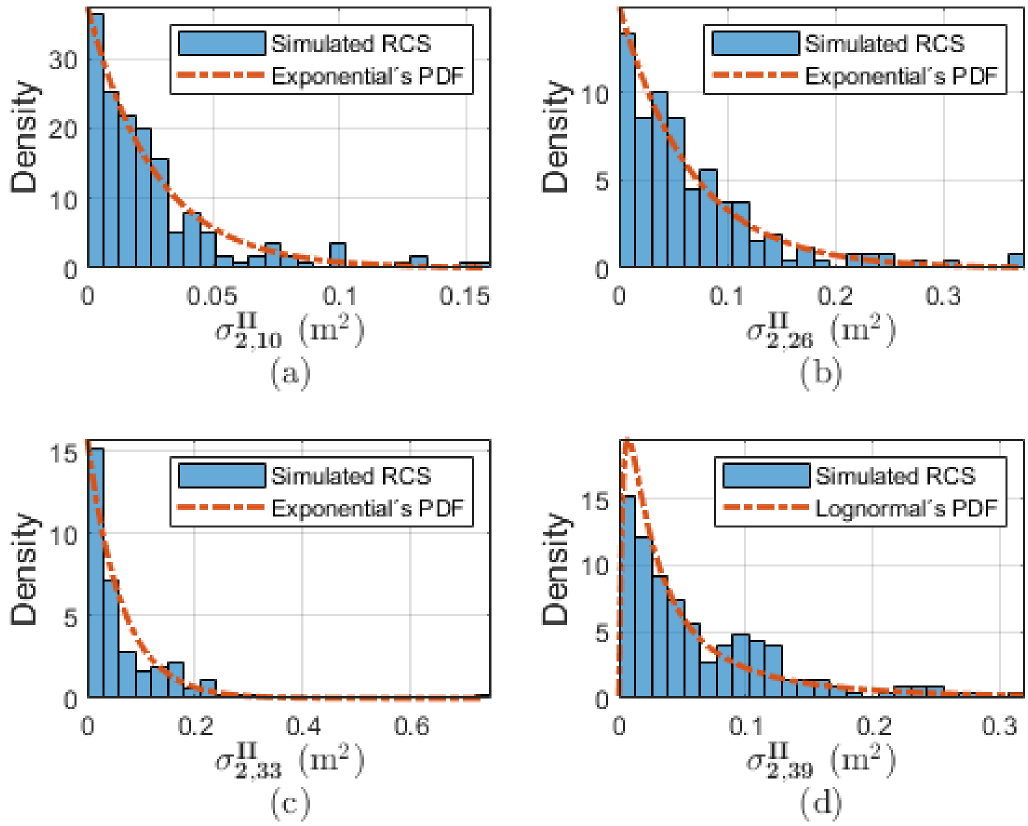

Figure 4.12: Histogram of simulated RCS values, $\boldsymbol{\sigma}^{II}_{f}$, for $\alpha^{II}_{2} = 0°$, and the best fitting probability distributions PDFs for (a) $f^{II}_{i} = 10$ GHz, (b) $f^{II}_{i} = 26$ GHz, (c) $f^{II}_{i} = 33$ GHz, and $f^{II}_{i} = 39$ GHz.

1 GHz. For the other UASs, the measured RCS is founded in Appendix B. Note that with increasing frequency, there is a tendency for the RCS values to increase, as seen for $\alpha^{III}_{0} = -90°$, in which the concentration of colored RCS dots are increasing.

Applying the steps presented in Subsection 4.3.5, Figure 4.15 shows the relative frequency of each probability distribution and the criterion for all frequencies used. Table 4.7 summarizes the best-fit probability distribution for each frequency and each UAS.

Observing this table, Figure 4.1, and Table 4.2 note that, in general, the Exponential distribution is well-fitted in UASs with large geometrical areas such as the Hexacopter and in UASs with more rounded geometric parts, such as DJI Phantom IV, DJI F450, and Walkera Voyager 4. The Generalized Pareto distribution appears to best fit UASs with lowest RCS, such as DJI Mavic Pro, Parrot AR.Drone, or Helicopter Kyosho and some UASs with more squared geometric parts such as DJI Matrice 100 and HMF Y600. Furthermore, besides the simulations of the Datasets I and II do not follow the entire setup of the measurement of the Dataset III, done by [29], it is possible to note that the

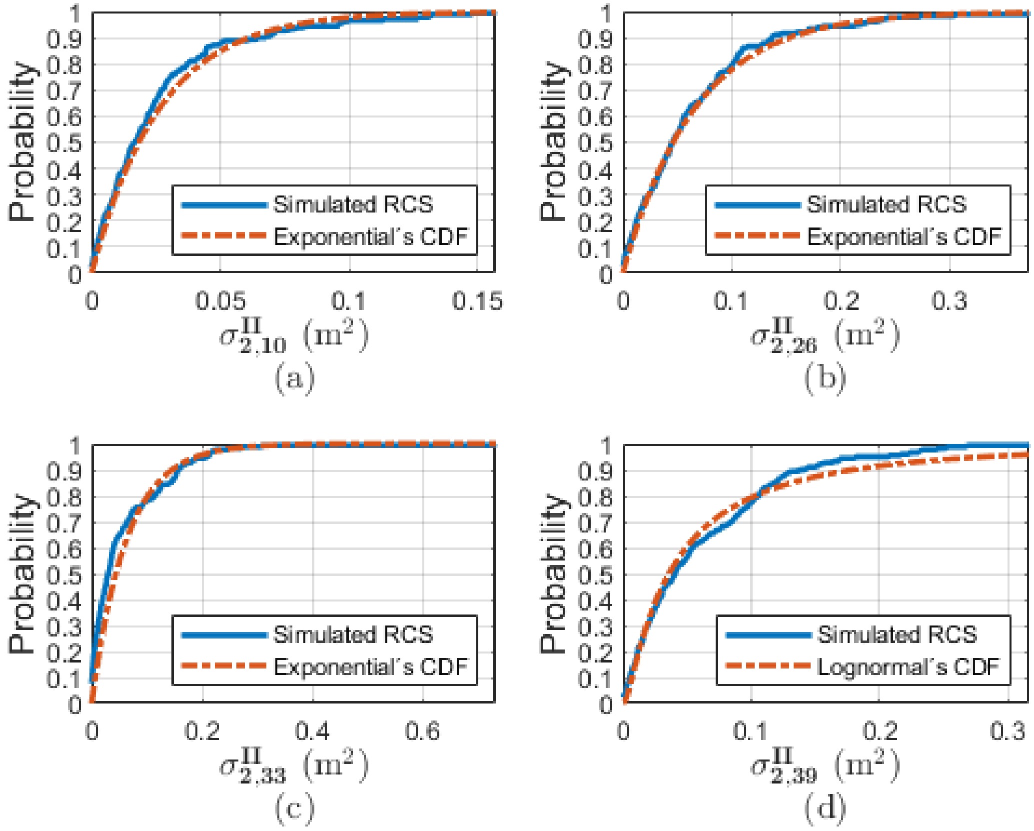

Figure 4.13: CDF of simulated RCS values, $\sigma^{II}_{2,j,f}$, for $\alpha^{II}_2 = 0°$, and the best fitting probability distributions CDFs for (a) $f^{II}_i = 10$ GHz, (b) $f^{II}_i = 26$ GHz, (c) $f^{II}_i = 33$ GHz, and $f^{II}_i = 39$ GHz.

Exponential distribution was also the best-fit distribution for the DJI Phantom IV.

To perform the analysis of PDF and CDF for DJI Phantom IV, consider $\alpha^{III}_{19} = 0°$ and x, the random variable for the Exponential distribution. The PDF, $f(x)$, and CDF, $F(x)$, of the Exponential distribution are given by (4.14) and (4.15), respectively. Figure 4.16 shows the histogram of the measured RCS values, $\boldsymbol{\sigma}^{III}_{19,f}$, for $\alpha^{III}_{19} = 0°$, and for $f^{III}_i =$ 26 GHz (a), $f^{III}_i = 31$ GHz (b), $f^{III}_i = 36$ GHz (c), and $f^{III}_i = 40$ GHz (d) along the PDFs of the best-fit probability distribution for the mentioned frequencies. In (a), (b), (c) and (d) the highest density is for $\sigma^{III}_{19,j} \leq 0.1$ m^2.

In order to analyze the CDFs, Figure 4.17 presents the curves of the CDF's measured RCS, $F_{ds_{III}}(\sigma^{III}_{19,j,f})$, for $\alpha^{III}_{19} = 0°$, and for $f^{III}_i = 26$ GHz (a), $f^{III}_i = 31$ GHz (b), $f^{III}_i = 36$ GHz (c), and $f^{III}_i = 40$ GHz (d) along the CDFs of the best-fit probability distribution for the mentioned frequencies.

Figure 4.17 (a) shows that there is a probability of 0.9 or 90% for $\sigma^{III}_{19,j} \leq 0.12$ m^2

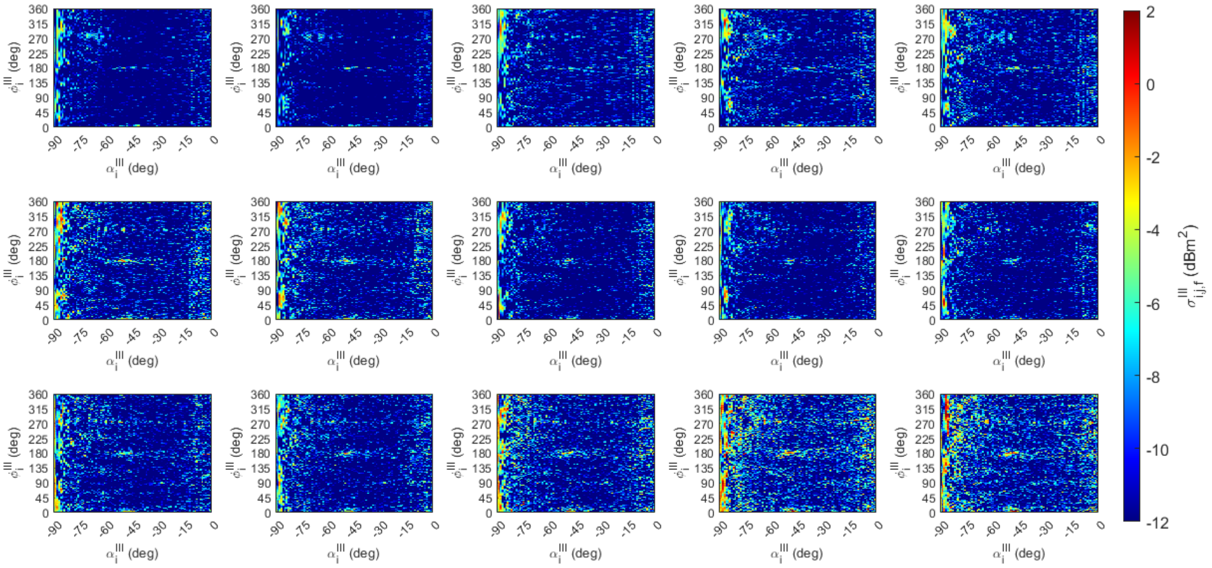

Figure 4.14: Measured RCS of the DJI Phantom IV for frequencies ranging from 26 to 40 GHz.

and $x \leq 0.1225$ m^2, i.e. $F_{ds_{III}}(\sigma_{19,j}^{III} \leq 0.12) = F(x \leq 0.1225) = 0.9$, that produces an error of $100 \times |x - \sigma_{19,j}^{III}|/\sigma_{19,j}^{III} = 100 \times |0.1225 - 0.12|/0.12 = 2.1\%$. Considering now $F_{ds_{III}}(\sigma_{19,j}^{III} \leq 0.04) = F(x \leq 0.0375) = 0.5$, it results in an error of approximately 6.25%. Furthermore, the linear correlation, given by (4.16), between both curves is $c_{y,x} = 0.9964$. In (b), $F_{ds_{III}}(\sigma_{19,j}^{III} \leq 0.1905) = F(x \leq 0.2032) = 0.9$ and $F_{ds_{III}}(\sigma_{19,j}^{III} \leq 0.06) = F(x \leq 0.0635) = 0.5$ yield errors of approximately 6.67% and 5.8%, respectively. The linear correlation for these curves is $c_{y,x} = 0.9979$. When performing the same calculations as in (c) and (d), it results in errors of 3.2% and 0% for (c) and 8.9% and 25.2% for (d). The linear correlations between the curves in (c) and (d) are, respectively, 0.9971 and 0.996.

4.4.4 Mean RCS values analysis

Despite the mean value itself does not provide robust information, it serves as a starting point for further analysis. Therefore, for Dataset I, Figure 4.18 shows the mean value of RCS, $\overline{\boldsymbol{\sigma}_i^I}$, as a function of the elevation angle, α_i^I. Note that the two largest RCS values are $\overline{\boldsymbol{\sigma}_0^I} = 1.24$ m^2 and $\overline{\boldsymbol{\sigma}_{37}^I} = 1.31$ m^2 for, respectively $\alpha_0^I = -90°$ and $\alpha_{37}^I = 90°$, which correspond to the bottom and top, respectively, of Phantom IV, where the area is greater.

For Dataset II, Figure 4.19 shows, on the left, the azimuth angle mean RCS values, $\overline{\boldsymbol{\sigma}_{i,f}^{II}}$, for each frequency, f, and each element of $\boldsymbol{\alpha}^{II}$, given by

$$\overline{\boldsymbol{\sigma}_{i,f}^{II}} = \sum_{j=0}^{N^{II}-1} \frac{\sigma_{i,j}^{II}}{N^{II}}, \tag{4.19}$$

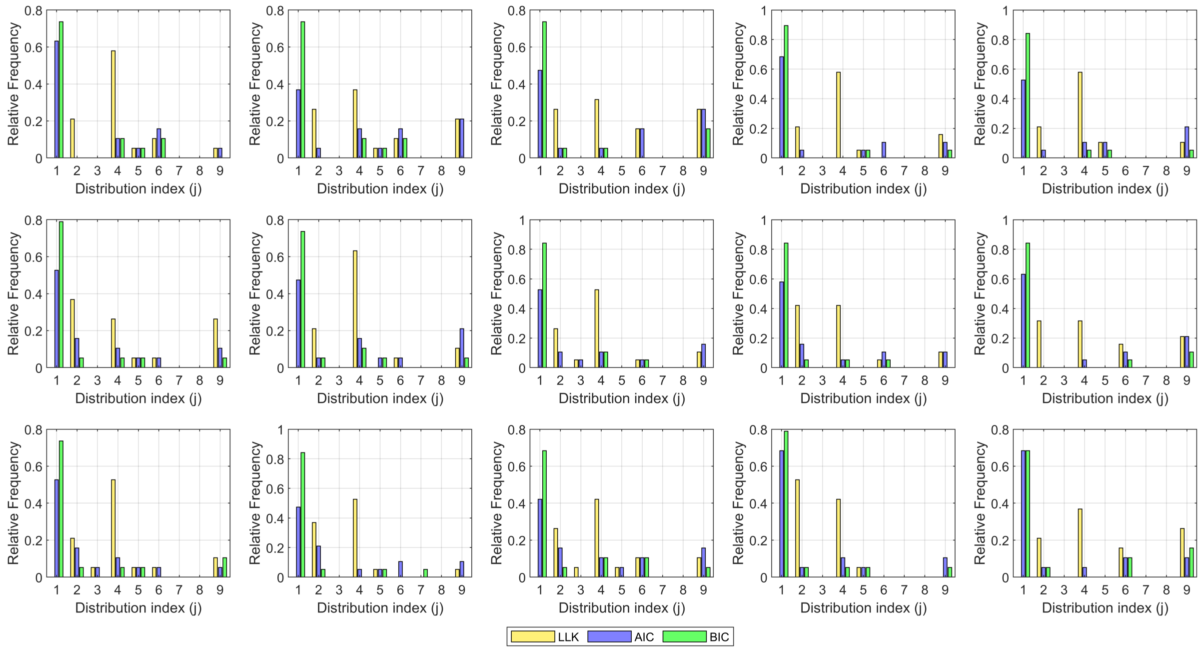

Figure 4.15: Relative frequency of each probability distribution for LLK, AIC and BIC in all $\boldsymbol{f}^{III}$ for DJI Phantom IV.

with $i = 0, 1, 2, \ldots, M^{II} - 1$ and $f \in \boldsymbol{f}^{\boldsymbol{II}}$. On the right, it shows the frequency mean RCS values of $\overline{\boldsymbol{\sigma}_{i,f}^{II}}$, named $\overline{\boldsymbol{\sigma}_{i}^{II}}$, over all the frequencies, $\boldsymbol{f}^{II}$, for each element of $\boldsymbol{\alpha}^{II}$, given by

$$\overline{\boldsymbol{\sigma}_{i}^{II}} = \sum_{f \in \boldsymbol{f}^{\boldsymbol{II}}} \frac{\overline{\boldsymbol{\sigma}_{i,f}^{II}}}{K^{II}}. \tag{4.20}$$

It is possible to note that for $\alpha_2^{II} = 0°$, $\overline{\boldsymbol{\sigma}_{i,f}^{II}}$ increases as the frequency also increases, which may demonstrate that the DJI Phantom IV sides are geometrically more uniform and with decreasing radar signal wavelength, the area which scatters the incident plane wave appears to be bigger. For the other values of α_i^{II}, there is a decrease in $\overline{\boldsymbol{\sigma}_{i}^{II}}$ as α_i^{II} moves away from 0°.

Figure 4.20 shows the elevation angle mean RCS values, $\overline{\boldsymbol{\sigma}_{f}^{II}}$, over all values of $\boldsymbol{\alpha}^{II}$ for each frequency, f, given by

$$\overline{\boldsymbol{\sigma}_{f}^{II}} = \sum_{i=0}^{M^{II}-1} \frac{\overline{\boldsymbol{\sigma}_{i,f}^{II}}}{M^{II}}. \tag{4.21}$$

Note that, in general, $\overline{\boldsymbol{\sigma}_{f}^{II}}$ increases with the increasing of the frequency, being $\overline{\boldsymbol{\sigma}_{f}^{II}} = 0.012$ m^2 for $f = 1$ GHz, $\overline{\boldsymbol{\sigma}_{f}^{II}} = 0.023$ m^2 for $f = 10$ GHz, and $\overline{\boldsymbol{\sigma}_{f}^{II}} = 0.037$ m^2 for $f = 40$ GHz.

For Dataset III, Figure 4.21 illustrates the increase in the mean of $\boldsymbol{\sigma}_{i,f}^{III}$, called $\overline{\boldsymbol{\sigma}_{f}^{III}}$,

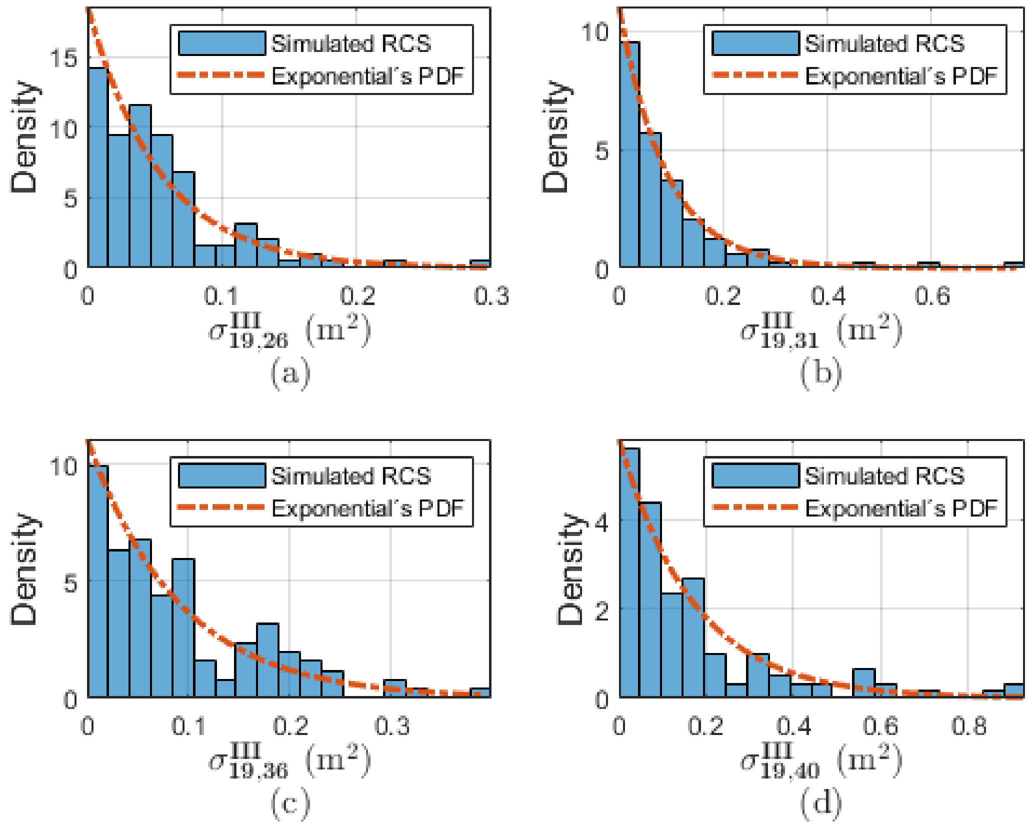

Figure 4.16: Histogram of measured RCS values, $\boldsymbol{\sigma}^{III}_{19,f}$, for $\alpha^{III}_{19} = 0°$, and the best fitting probability distributions PDFs for (a) $f^{III}_i = 26$ GHz, (b) $f^{III}_i = 31$ GHz, (c) $f^{III}_i = 36$ GHz, and $f^{III}_i = 40$ GHz.

$\forall \alpha^{III}_i \in \boldsymbol{\alpha}^{III}$, for some frequencies. Note that for $\alpha^{III}_0 = -90°$, the bottom of the drone, $\overline{\boldsymbol{\sigma}^{III}_{i,f}}$ is larger than the others because it has the largest area where the radar signal can reflect and scatter. Furthermore, it is important to observe that there is, for all frequencies, an approximate interval, $-40° \leq \alpha^{III}_i \leq -30°$, where $\overline{\boldsymbol{\sigma}^{III}_f}$ is minimum.

4.5 Summary

In this chapter, a statistical analysis of the RCS of nine UASs models was carried out, using three data sets: two simulated and one measured, provided by [29]. The goal was to verify the best probability distribution to model the RCS of the UASs at different frequencies and incidence angles. Thus, three criteria were used to evaluate the fit of the probability distributions to the RCS data: LLK, AIC, and BIC. These criteria allow comparing different distributions and penalizing the complexity of the models, avoiding overfitting the data. Furthermore, it was examined the mean values of the RCS as a

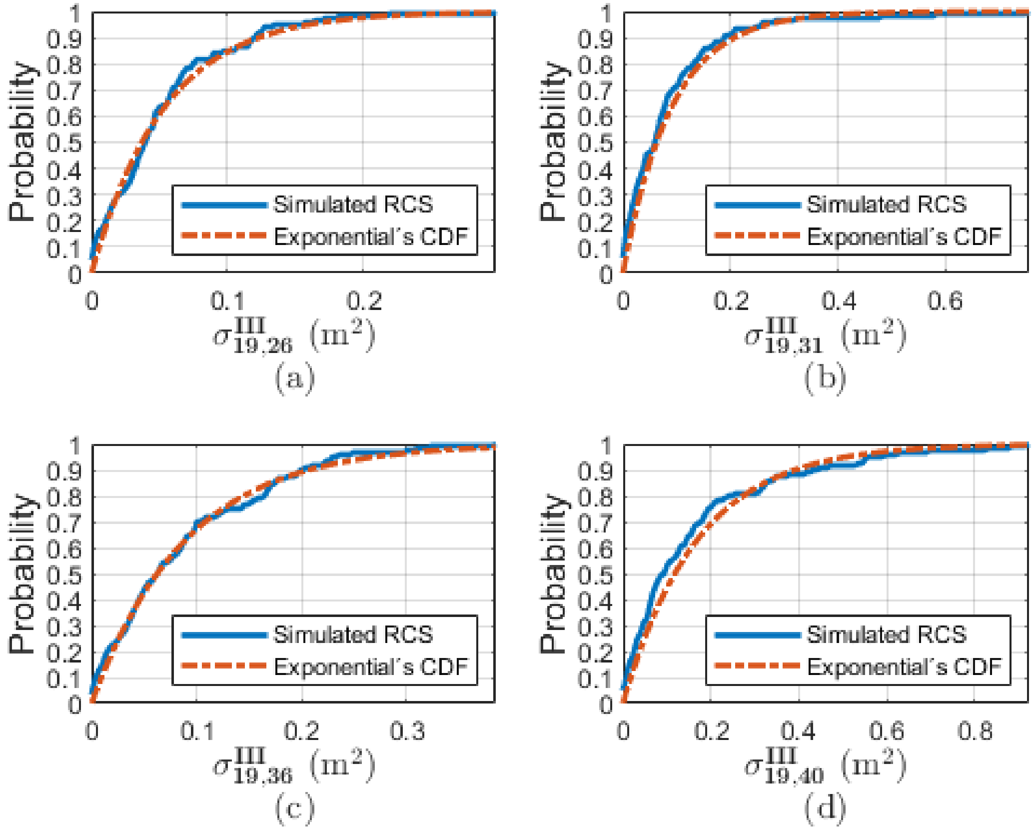

Figure 4.17: CDFs of measured RCS values, $\sigma^{III}_{19,j}$, for $\alpha^{III}_{19} = 0°$, and the best fitting probability distributions CDFs for (a) $f^{III}_i = 26$ GHz, (b) $f^{III}_i = 31$ GHz, (c) $f^{III}_i = 36$ GHz, and $f^{III}_i = 40$ GHz.

function of elevation angle and frequency. It highlights the impact of these factors on the RCS values and, consequently, on radar detection performance. The analysis contributes to understanding how RCS variability are affected by the changing of operating frequency and the elevation angle of the target.

The numerical results suggested that the Exponential distribution was the most frequent in the simulated and measured data for DJI Phantom IV and UASs with more rounded geometric parts, while the Generalized Pareto distribution was the most frequent for the data provided by [29], adapting itself with UASs with lowest RCS. These distributions presented the best LLK, AIC, and BIC values, in addition to a good agreement between the observed and expected PDF and CDF curves. Additionally, the analysis of the mean value of the RCS shows that, in general, the RCS increases with increasing frequency. Moreover, the RCS is shown to be higher at the top and bottom of the UAS where there is more reflective area.

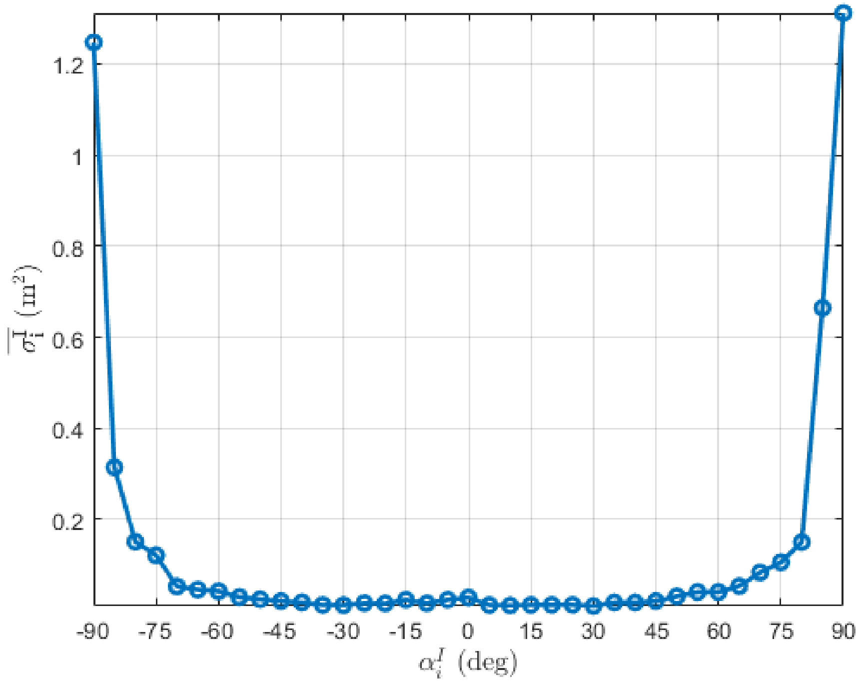

Figure 4.18: Mean values of the RCS as a function of the elevation angle.

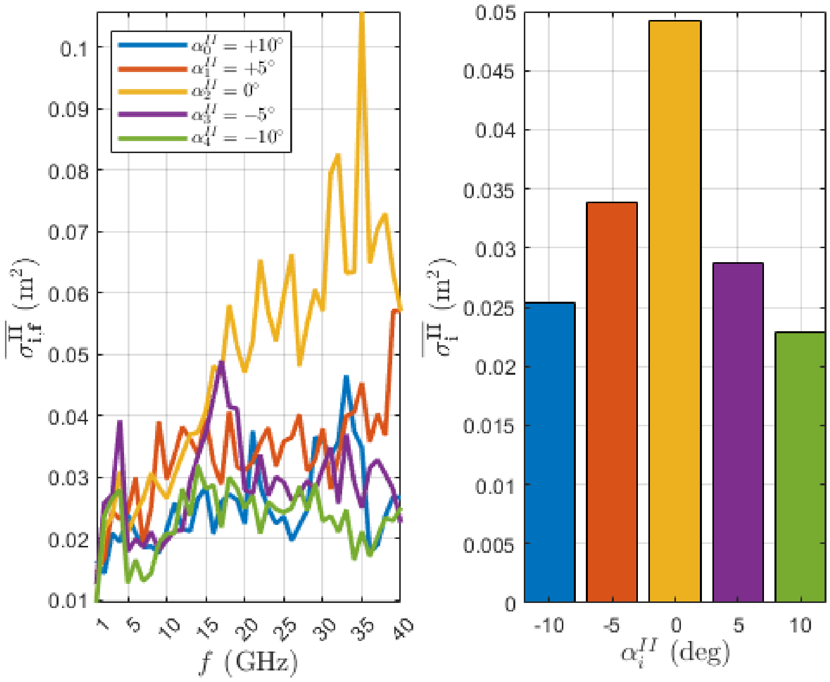

Figure 4.19: Azimuth angle mean RCS values, $\overline{\boldsymbol{\sigma}_{i,f}^{II}}$, as a function of the frequency for the simulated elevation angles, α_i^{II}, (left) and frequency mean RCS values, $\overline{\boldsymbol{\sigma}_i^{II}}$, over all the frequencies, for each simulated elevation angle, α_i^{II} (right).

Table 4.4: Exponential's parameter, γ, for distinct elevation angles, $\boldsymbol{\alpha}^I$.

$\boldsymbol{\alpha}^I$	γ
-90º	1.2473
-85º	0.3144
-80º	0.1511
-75º	0.1210
-70º	0.0527
-65º	0.0457
-60º	0.0423
-55º	0.0292
-50º	0.0246
-45º	0.0206
-40º	0.0177
-35º	0.0121
-30º	0.0116
-25º	0.0162
-20º	0.0155
-15º	0.0235
-10º	0.0160
-5º	0.0236
0º	0.0284
5º	0.0119
10º	0.0112
15º	0.0122
20º	0.0123
25º	0.0125
30º	0.0099
35º	0.0176
40º	0.0175
45º	0.0205
50º	0.0310
55º	0.0405
60º	0.0405
65º	0.0535
70º	0.0835
75º	0.1056
80º	0.1502
85º	0.6645
90º	1.3116

Table 4.5: Best probability distribution and its average relative frequency for all frequencies.

f^{II} (GHz)	**Best-fit distribution**	R_{II,avg_j}
1	Nakagami	0.33
2	Log-normal	0.80
3	Exponential	0.40
4	Exponential	0.40
5	Exponential	0.40
6	Gamma	0.33
7	Exponential	0.33
8	Exponential	0.27
9	Log-normal	0.53
10	Exponential	0.67
11	Exponential	0.60
12	Exponential	0.47
13	Exponential	0.47
14	Exponential	0.40
15	Log-normal	0.33
16	Exponential	0.33
17	Log-normal	0.53
18	Exponential	0.40
19	Log-normal	0.53
20	Generalized Pareto	0.33
21	Log-normal	0.33
22	Exponential	0.53
23	Exponential	0.60
24	Exponential	0.47
25	Log-normal	0.53
26	Exponential	0.53
27	Log-normal	0.53
28	Log-normal	0.40
29	Exponential	0.33
30	Exponential	0.40
31	Exponential	0.33
32	Gamma	0.27
33	Exponential	0.27
34	Log-normal	0.53
35	Exponential	0.47
36	Exponential	0.27
37	Gamma	0.27
38	Exponential	0.40
39	Log-normal	0.47
40	Gamma	0.53

Table 4.6: Parameters values of the best-fits distribution for each frequency.

			α^{II}				
f_i^{II} **GHz**	**Distribution**	**Parameters**	$-10°$	$-5°$	$0°$	$5°$	$10°$
1	Nakagami	μ, Ω	$0.5265, 0.0004$	$0.5625, 0.0003$	$0.3839, 0.0002$	$0.7116, 0.0002$	$0.7673, 0.0001$
2	Lognormal	μ, σ	$-5.0038, 1.3175$	$-4.8225, 1.3136$	$-4.7389, 1.4262$	$-4.2935, 1.1367$	$-4.1883, 0.9585$
3	Exponential	μ	0.0207	0.0242	0.0234	0.0268	0.0262
4	Exponential	μ	0.0199	0.0238	0.0310	0.0388	0.0276
5	Exponential	μ	0.0258	0.0249	0.0215	0.0178	0.0133
6	Gamma	a, b	$1.3747, 0.0144$	$1.1083, 0.0277$	$1.1290, 0.0218$	$1.3858, 0.0145$	$1.5177, 0.0120$
7	Exponential	μ	0.0174	0.0205	0.0260	0.0188	0.0150
8	Exponential	μ	0.0201	0.0243	0.0328	0.0192	0.0135
9	Lognormal	μ, σ	$-4.4585, 0.9624$	$-3.5702, 0.7547$	$-4.2391, 1.32$	$-4.5827, 0.9089$	$-4.6905, 1.4165$
10	Exponential	μ	0.0181	0.0301	0.0271	0.0223	0.0218
11	Exponential	μ	0.0254	0.0375	0.0307	0.0232	0.0232
12	Exponential	μ	0.0231	0.0346	0.0295	0.0213	0.0251
13	Exponential	μ	0.0207	0.0358	0.0350	0.0385	0.0233
14	Exponential	μ	0.0247	0.0313	0.0308	0.0398	0.0305
15	Lognormal	μ, σ	$-4.3385, 1.04$	$-4.0246, 1.37$	$-3.7661, 1.4753$	$-3.4856, 0.8565$	$-3.9650, 0.8899$
16	Exponential	μ	0.0184	0.0266	0.0529	0.0585	0.0344
17	Lognormal	μ, σ	$-4.2219, 0.9499$	$-4.0580, 0.9607$	$-3.6578, 0.9088$	$-3.4156, 1.2325$	$-4.2405, 1.1228$
18	Exponential	μ	0.0272	0.0376	0.0486	0.0493	0.0368
19	Lognormal	μ, σ	$-4.1432, 1.0046$	$-3.9469, 0.9628$	$-3.5106, 0.9846$	$-3.6378, 1.2003$	$-4.4471, 1.0957$
20	Gen. Pareto	k, σ, θ	$-0.3038, 0.0242, 0$	$-0.37, 0.0375, 0$	$-0.5129, 0.0682, 0$	$-0.0564, 0.0228, 0$	$0.3249, 0.0191, 0$
21	Lognormal	μ, σ	$-4.4235, 1.1207$	$-4.0116, 1.2978$	$-3.4628, 1.1738$	$-4.1645, 1.3023$	$-4.2757, 1.1832$
22	Exponential	μ	0.0247	0.0507	0.0881	0.0354	0.0202
23	Exponential	μ	0.0197	0.0320	0.0485	0.0258	0.0233
24	Exponential	μ	0.0201	0.0285	0.0675	0.0297	0.0204
25	Lognormal	μ, σ	$-4.2236, 0.9230$	$-3.6892, 1.0759$	$-3.5116, 1.0370$	$-4.2429, 0.9571$	$-4.2643, 1.1758$
26	Exponential	μ	0.0193	0.0402	0.0577	0.0323	0.0235
27	Lognormal	μ, σ	$-4.3760, 0.8094$	$-3.9194, 0.9822$	$-3.6540, 1.1809$	$-3.9453, 0.8218$	$-4.1877, 1.1230$
28	Lognormal	μ, σ	$-4.3806, 1.1166$	$-4.1796, 1.2473$	$-3.3444, 1.2409$	$-4.3126, 1.1954$	$-4.0104, 0.8676$
29	Exponential	μ	0.0165	0.0317	0.0693	0.0307	0.0339
30	Exponential	μ	0.0212	0.0290	0.0523	0.0299	0.0249
31	Exponential	μ	0.0186	0.0276	0.0708	0.0357	0.0234
32	Gamma	a, b	$0.9529, 0.02$	$1.3617, 0.0221$	$0.7543, 0.1218$	$1.3645, 0.02$	$1.0948, 0.0205$
33	Exponential	μ	0.0264	0.0394	0.0635	0.032	0.025
34	Lognormal	μ, σ	$-4.6798, 1.2171$	$-3.9463, 1.2941$	$-3.5387, 1.2218$	$-4.0855, 1.0824$	$-4.8369, 1.1348$
35	Exponential	μ	0.0165	0.0376	0.1129	0.0251	0.0221
36	Exponential	μ	0.018	0.0366	0.0691	0.0327	0.0167
37	Gamma	a, b	$1.0335, 0.0171$	$1.4766, 0.0251$	$1.4863, 0.0493$	$1.4137, 0.0239$	$1.1263, 0.0171$
38	Exponential	μ	0.0248	0.0384	0.1014	0.0336	0.0229
39	Lognormal	μ, σ	$-4.4527, 1.1416$	$-3.2924, 1.0343$	$-3.2477, 0.9595$	$-4.1576, 0.9440$	$-4.2924, 1.0731$
40	Gamma	a, b	$1.5177, 0.0120$	$1.7102, 0.0791$	$1.4917, 0.0415$	$1.2762, 0.029$	$1.2909, 0.0199$

Table 4.7: Best-fit distribution for each UAS model and for each frequency.

		Best-Fit Distribution								
		Phantom IV	**Mavic**	**F450**	**M100**	**Parrot**	**Kyosho**	**Y600**	**Voyager 4**	**Hexa**
f_i^{III} **(GHz)**	26	Exponential	Lognormal	Exponential	Gen. Pareto	Gen. Pareto	Gen. Pareto	Gen. Pareto	Weibull	Exponential
	27	Exponential	Gen. Pareto	Gen. Pareto	Gen. Pareto	Gen. Pareto	Gen. Pareto	Gen. Pareto	Exponential	Exponential
	28	Exponential	Gen. Pareto	Exponential	Exponential	Gen. Pareto	Gen. Pareto	Gamma	Exponential	Exponential
	29	Exponential	Gen. Pareto	Exponential	Gen. Pareto	Gen. Pareto	Exponential	Exponential	Exponential	Exponential
	30	Exponential	Gen. Pareto	Gen. Pareto	Exponential	Lognormal	Gen. Pareto	Exponential	Exponential	Exponential
	31	Exponential	Gen. Pareto	Gen. Pareto	Exponential	Gen. Pareto	Gen. Pareto	Exponential	Exponential	Exponential
	32	Exponential	Gen. Pareto	Exponential	Exponential	Lognormal	Gen. Pareto	Gen. Pareto	Gen. Pareto	Exponential
	33	Exponential	Gen. Pareto	Exponential	Weibull	Gen. Pareto	Gen. Pareto	Weibull	Exponential	Weibull
	34	Exponential	Gen. Pareto	Gen. Pareto	Gen. Pareto	Gen. Pareto	Gen. Pareto	Gen. Pareto	Gen. Pareto	Exponential
	35	Exponential	Gen. Pareto	Exponential	Gen. Pareto	Gen. Pareto	Gen. Pareto	Gen. Pareto	Exponential	Exponential
	36	Exponential	Gen. Pareto	Gen. Pareto	Exponential	Gen. Pareto	Weibull	Gen. Pareto	Exponential	Exponential
	37	Exponential	Gen. Pareto	Exponential	Gen. Pareto	Lognormal	Gen. Pareto	Gen. Pareto	Exponential	Exponential
	38	Exponential	Gen. Pareto	Gen. Pareto	Gen. Pareto	Gen. Pareto	Gen. Pareto	Gen. Pareto	Exponential	Exponential
	39	Exponential	Gen. Pareto	Gen. Pareto	Gen. Pareto	Gen. Pareto	Gen. Pareto	Gen. Pareto	Exponential	Exponential
	40	Exponential	Gen. Pareto	Gen. Pareto	Exponential	Gen. Pareto	Gen. Pareto	Gen. Pareto	Weibull	Exponential

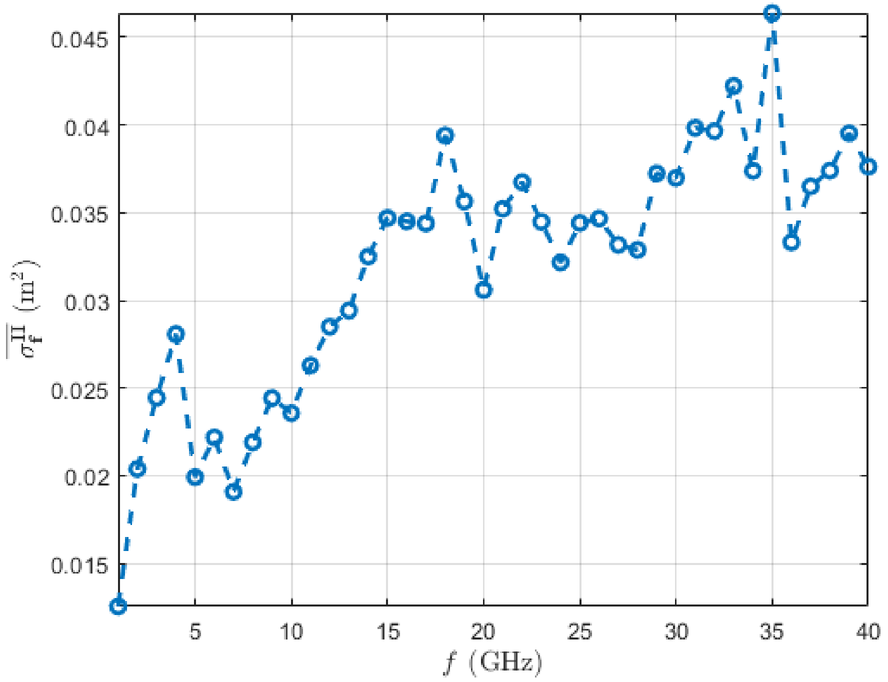

Figure 4.20: Elevation angle mean RCS values, $\overline{\boldsymbol{\sigma}_f^{II}}$, over all values of $\boldsymbol{\phi}^{II}$ and $\boldsymbol{\alpha}^{II}$ for each frequency.

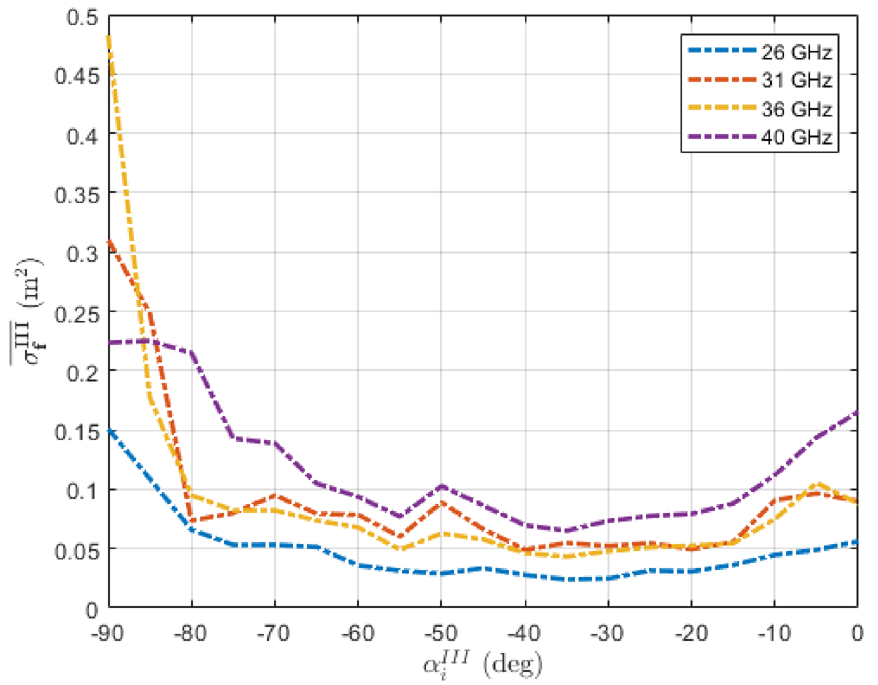

Figure 4.21: $\overline{\boldsymbol{\sigma}_f^{III}}$ from DJI Phantom IV for $f_i^{III} = 26, 31, 36$ and 40 GHz.

Chapter 5

Conclusion

This work presented a statistical analysis and modeling of the RCS of UASs, as well as an evaluation of their detection by an X-band pulsed radar. The goal was to contribute to the development of countermeasure techniques against potential threats caused by the misuse of UAS.

Chapter 2 discussed the radar system, a technology that emits electromagnetic waves and captures reflected signals to determine the presence, distance, and speed of targets. It explained the classification of radar systems according to their operating frequency range, which affects their performance and characteristics. The chapter also covered the Doppler Effect, which is the change in the measured frequency of a wave due to the relative motion between the source and the observer. It further elaborated on the transmitted signal's waveform, the shape of the signal emitted by the radar system, which can be either pulsed or continuous wave. Lastly, it introduced the radar equation, a mathematical expression that relates the maximum range and the parameters that affect radar detection.

In Chapter 3, the use of the Furuno FAR-2117 pulsed radar to detect the DJI Phantom IV drone was investigated. For this, RCS simulations, radar range, and detection probability were performed. Subsequently, a field measurement was conducted using the Furuno FAR-2117 radar and the DJI Phantom IV drone, which was flying over Guanabara Bay. The results indicated that the radar was able to detect the drone at a maximum range of 425 m and a maximum height of 32 m, under favorable electromagnetic propagation conditions and for $P_d \geq 0.99$. Furthermore, the two proposed methods helped infer the value of the system loss, L_s, a parameter that is not easily obtained from the manufacturer and essential to perform such analysis. The difference between the simulated results and the field measurements was due to the statistical nature of the RCS of the UAS and the fact that more cables were used than necessary, in the installation of the product, to obtain the best performance of the FAR-2117 radar which increases the loss of the system.

In Chapter 4, the statistical analysis and modeling of the RCS of a DJI Phantom IV drone and a database composed of nine different UASs were discussed. For the Phantom IV drone, the RCS datasets were generated through simulations for distinct frequencies and azimuth and elevation angles, and for the UAS database, the RCSs were measured in an anechoic chamber by [29]. Then, the subdatasets, created from the datasets, were fitted to usual probability distributions using three criteria, namely: Log-Likelihood (LLK), Akaike Information Criterion (AIC), and Bayesian Information Criterion (BIC). In addition, the impacts of RCS modeling on radar detection range were analyzed and were found a difference ,between the use of the mean RCS value from Chapter 3 and the 50% RCS value from the CDF curve, of 53 m for $P_d = 0.99$ and 197 m for $P_d = 0.2$. Moreover when comparing the simulated and modeled RCS values it was obtained an error of 3.8%. Furthermore, the results indicated that the exponential distribution best fit the simulated and measured RCS data, in general. Also, it was analyzed the mean RCS values. It showed that, in general, the RCS increases with increasing frequency. Moreover, the RCS is higher at the top and bottom of the UAS where there is more reflective area.

Finally, for future work, it is intended as follows:

- To use different UASs for field measurements of the maximum range for the Furuno FAR-2117 pulsed radar and a FMCW radar, in order to compare each other performance.
- To perform a known setup for RCS measurement, in an anechoic chamber, of different drones in order to simulate it in the same conditions and better validate it.
- To use statistical criteria to perform a mean of UAS classification, analyzing the different scores that each drone has achieved for each criterion.
- To study the relationship between average RCS peaks at certain frequencies.
- To treat RCS as a stochastic process combining variables such as frequency, elevation angle and azimuth and radar straight section to analise their behavior.

References

[1] ALVARADO, E. *Discover the Use of Drones for VLOS and BVLOS*. Nov 2023. Drone Industry Insights. Accessed: December 4, 2023. Disponível em: <https://droneii.com/use-of-drones-around-the-world-drone-utilization>.

[2] FAA. *FAA Aerospace Forecast Fiscal Years 2023–2043*. May 2023. Federal Aviation Administration. United States Department of Transportation. Accessed: December 4, 2023. Disponível em: <https://www.faa.gov/data_research/aviation/aerospace_forecasts>.

[3] ANAC. *Quantidade de Cadastros - Drones*. May 2022. Agência Nacional de Aviação Civil (ANAC). Accessed: December 4, 2023. Disponível em: <https://www.gov.br/anac/pt-br/assuntos/drones/quantidade-de-cadastros>.

[4] CHABOT, D.; HODGSON, A. J.; HODGSON, J. C.; ANDERSON, K. 'drone': technically correct, popularly accepted, socially acceptable. *Drone Systems and Applications*, v. 10, n. 1, p. 399–405, 2022. Disponível em: <https://doi.org/10.1139/dsa-2022-0041>.

[5] BUCKER, A.; BONATTI, R.; SCHERER, S. Do you see what i see? coordinating multiple aerial cameras for robot cinematography. In: IEEE. *2021 IEEE International Conference on Robotics and Automation (ICRA)*. [S.l.], 2021. p. 7972–7979.

[6] CHIANG, W.-C.; LI, Y.; SHANG, J.; URBAN, T. L. Impact of drone delivery on sustainability and cost: Realizing the uav potential through vehicle routing optimization. *Applied energy*, Elsevier, v. 242, p. 1164–1175, 2019.

[7] BALDISSERI, A.; SIRAGUSA, C.; SEGHEZZI, A.; MANGIARACINA, R.; TUMINO, A. Truck-based drone delivery system: An economic and environmental assessment. *Transportation Research Part D: Transport and Environment*, Elsevier, v. 107, p. 103296, 2022.

[8] HELL, P. M.; VARGA, P. J. Drone systems for factory security and surveillance. *Interdisciplinary Description of Complex Systems: INDECS*, Croatian Interdisciplinary Society, v. 17, n. 3-A, p. 458–467, 2019.

[9] KLAUSER, F. Policing with the drone: Towards an aerial geopolitics of security. *Security Dialogue*, SAGE Publications Sage UK: London, England, v. 53, n. 2, p. 148–163, 2022.

[10] SAGE, A. T. Testing the delivery of human organ transportation with drones in the real world. *Science Robotics*, v. 7, n. 73, p. eadf5798, 2022.

[11] KALLENBORN, Z.; ACKERMAN, G.; BLEEK, P. C. A plague of locusts? a preliminary assessment of the threat of multi-drone terrorism. *Terrorism and political violence*, Taylor & Francis, v. 35, n. 7, p. 1556–1585, 2023.

[12] SCHMERSAHL, A. R. *Fifty feet above the wall: cartel drones in the US-Mexico border zone airspace, and what to do about them.* Tese (Doutorado) — Monterey, California: Naval Postgraduate School, 2018.

[13] NASSI, B.; BEN-NETANEL, R.; SHAMIR, A.; ELOVICI, Y. Game of drones-detecting spying drones using time domain analysis. In: SPRINGER. *Cyber Security Cryptography and Machine Learning: 5th International Symposium, CSCML 2021, Be'er Sheva, Israel, July 8–9, 2021, Proceedings 5*. [S.l.], 2021. p. 128–144.

[14] SEIDALIYEVA, U.; AKHMETOV, D.; ILIPBAYEVA, L.; MATSON, E. T. Real-time and accurate drone detection in a video with a static background. *Sensors*, MDPI, v. 20, n. 14, p. 3856, 2020.

[15] LIU, H.; QU, F.; LIU, Y.; ZHAO, W.; CHEN, Y. A drone detection with aircraft classification based on a camera array. In: IOP PUBLISHING. *IOP Conference Series: Materials Science and Engineering*. [S.l.], 2018. v. 322, n. 5, p. 052005.

[16] SVANSTRÖM, F.; ENGLUND, C.; ALONSO-FERNANDEZ, F. Real-time drone detection and tracking with visible, thermal and acoustic sensors. In: IEEE. *2020 25th International Conference on Pattern Recognition (ICPR)*. [S.l.], 2021. p. 7265–7272.

[17] SAMARAS, S.; DIAMANTIDOU, E.; ATALOGLOU, D.; SAKELLARIOU, N.; VAFEIADIS, A.; MAGOULIANITIS, V.; LALAS, A.; DIMOU, A.; ZARPALAS, D.; VOTIS, K. Deep learning on multi sensor data for counter uav applications—a systematic review. *Sensors*, MDPI, v. 19, n. 22, p. 4837, 2019.

[18] BERNARDINI, A.; MANGIATORDI, F.; PALLOTTI, E.; CAPODIFERRO, L. Drone detection by acoustic signature identification. *Electronic Imaging*, Society for Imaging Science and Technology, v. 2017, n. 10, p. 60–64, 2017.

[19] TAHA, B.; SHOUFAN, A. Machine learning-based drone detection and classification: State-of-the-art in research. *IEEE Access*, v. 7, p. 138669–138682, 2019.

[20] SHI, Z.; CHANG, X.; YANG, C.; WU, Z.; WU, J. An acoustic-based surveillance system for amateur drones detection and localization. *IEEE transactions on vehicular technology*, IEEE, v. 69, n. 3, p. 2731–2739, 2020.

[21] SEDUNOV, A.; HADDAD, D.; SALLOUM, H.; SUTIN, A.; SEDUNOV, N.; YAKUBOVSKIY, A. Stevens drone detection acoustic system and experiments in acoustics uav tracking. In: IEEE. *2019 IEEE International Symposium on Technologies for Homeland Security (HST)*. [S.l.], 2019. p. 1–7.

[22] NGUYEN, P.; TRUONG, H.; RAVINDRANATHAN, M.; NGUYEN, A.; HAN, R.; VU, T. Cost-effective and passive rf-based drone presence detection and characterization. *GetMobile: Mobile Computing and Communications*, ACM New York, NY, USA, v. 21, n. 4, p. 30–34, 2018.

[23] MEDAIYESE, O. O.; SYED, A.; LAUF, A. P. Machine learning framework for rf-based drone detection and identification system. In: IEEE. *2021 2nd International Conference On Smart Cities, Automation & Intelligent Computing Systems (ICON-SONICS)*. [S.l.], 2021. p. 58–64.

[24] NGUYEN, P.; KIM, T.; MIAO, J.; HESSELIUS, D.; KENNEALLY, E.; MASSEY, D.; FREW, E.; HAN, R.; VU, T. Towards rf-based localization of a drone and its controller. In: *Proceedings of the 5th workshop on micro aerial vehicle networks, systems, and applications*. [S.l.: s.n.], 2019. p. 21–26.

[25] FLAK, P. Drone detection sensor with continuous 2.4 ghz ism band coverage based on cost-effective sdr platform. *IEEE Access*, IEEE, v. 9, p. 114574–114586, 2021.

[26] SKOLNIK, M. *Radar Handbook*. 3rd. ed. [S.l.]: New York: McGraw-Hill, 2008.

[27] KNOTT, E. F.; SCHAEFFER, J. F.; TULLEY, M. T. *Radar cross-section*. 2nd. ed. [S.l.]: SciTech Publishing, 2004.

[28] RICHARDS, M. A. *Principles of modern radar*. [S.l.]: SciTech Publishing, 2010.

[29] SEMKIN, V.; HAARLA, J.; PAIRON, T.; SLEZAK, C.; RANGAN, S.; VIIKARI, V.; OESTGES, C. *Drone RCS measurements (26-40 GHz)*. IEEE Dataport, 2019. Disponível em: <https://dx.doi.org/10.21227/m8xk-dr55>.

[30] BROWN, L. First clashes. In: *A Radar History of World War II*. [S.l.]: Institute of Physics Publishing, 1999. cap. 3.

[31] CICHON, D.; WIESBECK, W. The heinrich hertz wireless experiments at karlsruhe in the view of modern communication. In: *Proceedings of the 1995 International Conference on 100 Years of Radio*. [S.l.: s.n.], 1995. p. 1–6.

[32] GRIFFITHS, H.; KNOTT, P.; KOCH, W. Christian hülsmeyer: Invention and demonstration of radar, 1904. *IEEE Aerospace and Electronic Systems Magazine*, v. 34, n. 9, p. 56–60, 2019.

[33] RIDENOUR, L. N. Radar in war and peace. *Electrical Engineering*, v. 65, n. 5, p. 202–207, 1946.

[34] CURRY, G. R. *Radar System Performance Modeling*. 2nd. ed. [S.l.]: Artech House, 2004.

[35] IEEE. IEEE standard letter designations for radar-frequency bands. *IEEE Std 521-2019 (Revision of IEEE Std 521-2002)*, p. 1–15, 2020.

[36] ITU. Nomenclature of the frequency and wavelength bands used in telecommunications. *Recommendation ITU-R V.431-8*, p. 1–5, 2015.

[37] JAHANGIR, M.; BAKER, C. Persistence surveillance of difficult to detect micro-drones with l-band 3-d holographic radar™. In: IEEE. *2016 CIE International Conference on Radar (RADAR)*. [S.l.], 2016. p. 1–5.

[38] TORVIK, B.; OLSEN, K. E.; GRIFFITHS, H. Classification of birds and uavs based on radar polarimetry. *IEEE geoscience and remote sensing letters*, IEEE, v. 13, n. 9, p. 1305–1309, 2016.

[39] PARK, S.; PARK, S.-O. Configuration of an x-band fmcw radar targeted for drone detection. In: IEEE. *2017 International Symposium on Antennas and Propagation (ISAP)*. [S.l.], 2017. p. 1–2.

[40] KIM, B. K.; KANG, H.-S.; PARK, S.-O. Drone classification using convolutional neural networks with merged doppler images. *IEEE Geoscience and Remote Sensing Letters*, IEEE, v. 14, n. 1, p. 38–42, 2016.

[41] ZULKIFLI, S.; BALLERI, A. Design and development of k-band fmcw radar for nano-drone detection. In: IEEE. *2020 IEEE Radar Conference (RadarConf20)*. [S.l.], 2020. p. 1–5.

[42] FUHRMANN, L.; BIALLAWONS, O.; KLARE, J.; PANHUBER, R.; KLENKE, R.; ENDER, J. Micro-doppler analysis and classification of uavs at ka band. In: *2017 18th International Radar Symposium (IRS)*. [S.l.: s.n.], 2017. p. 1–9.

[43] MAHAFZA, B. R. *Radar systems analysis and design using MATLAB*. [S.l.]: Chapman and Hall/CRC, 2005.

[44] ZHANG, P.; YANG, L.; CHEN, G.; LI, G. Classification of drones based on micro-doppler signatures with dual-band radar sensors. In: IEEE. *2017 Progress in Electromagnetics Research Symposium-Fall (PIERS-FALL)*. [S.l.], 2017. p. 638–643.

[45] ENGELHARDT, W. Relativistic doppler effect and the principle of relativity. *Apeiron*, v. 10, n. 4, p. 29–49, 2003.

[46] SKOLNIK, M. An introduction and overview of radar. *Radar Handbook*, New York: McGraw-Hill, v. 3, p. 1–1, 2008.

[47] JANKIRAMAN, M. *FMCW Radar Design*. [S.l.]: Artech House, 2018. (Artech House radar library). ISBN 9781630815677.

[48] DONG, B.; CHEN, Z.; LI, G. Unambiguous doppler extension for fmcw radar via poisson disk sampling. *IEEE Geoscience and Remote Sensing Letters*, v. 19, p. 1–5, 2022.

[49] ALBERSHEIM, W. J. A closed-form approximation to robertson's detection characteristics. In: *Proceeding IEEE 69*. [S.l.: s.n.], 1969.

[50] IEEE Recommended Practice for Radar Cross-Section Test Procedures. *IEEE Std 1502-2020 (Revision of IEEE Std 1502-2007)*, p. 1–78, 2020.

[51] BALANIS, C. A. *Antenna theory: analysis and design*. [S.l.]: John wiley & sons, 2016.

[52] BARTON, D. *Radar Equations for Modern Radar*. [S.l.]: Artech House, 2012.

[53] SWERLING, P. Probability of detection for fluctuating targets. *IRE Transactions on Information Theory*, v. 6, n. 2, p. 269–308, 1960.

[54] MAHAFZA, B. R. *Radar systems analysis and design using MATLAB*. Third edition. [S.l.]: Chapman and Hall/CRC, 2013.

[55] BARTON, D. Radar system analysis and modeling. *IEEE Aerospace and Electronic Systems Magazine*, v. 20, n. 4, p. 23–25, 2005.

[56] BURROWS, C.; ATTWOOD, S. *Radio Wave Propagation: Consolidated Summary Technical Report of the Committee on Propagation of the National Defense Research Committee*. Elsevier Science, 2013. ISBN 9781483258546. Disponível em: <https://books.google.com.br/books?id=k7g4BQAAQBAJ>.

[57] DEPARTMENT, A. *Electronic Warfare and Radar Systems Engineering Handbook*. [S.l.], 2013.

[58] NEWS, B. *Drones in Modern Warfare: A Growing Threat*. 2023. Disponível em: <https://www.bbc.com/news/world-54726960>.

[59] TIMES, T. N. Y. *Ukraine's Use of Drones in the Conflict with Russia*. 2023. Disponível em: <https://www.nytimes.com/article/ukraine-drones-conflict.html>.

[60] JONES, M. Comparative analysis of drone detection technologies. *International Journal of Security and Defense*, v. 18, n. 3, 2022.

[61] SMITH, J.; AL. et. Advancements in radar technology for drone detection. *Journal of Defense Technology*, v. 25, n. 2, 2023.

[62] FARLIK, J.; KRATKY, M.; CASAR, J.; STARY, V. Multispectral detection of commercial unmanned aerial vehicles. *Sensors*, v. 19, n. 7, 2019. ISSN 1424-8220.

[63] OCHODNICKý, J.; MATOUSEK, Z.; BABJAK, M.; KURTY, J. Drone detection by ku-band battlefield radar. In: *2017 International Conference on Military Technologies (ICMT)*. [S.l.: s.n.], 2017. p. 613–616.

[64] LAUČYS, A.; RUDYS, S.; KINKA, M.; RAGULIS, P.; ALEKSANDRAVIČIUS, J.; JABLONSKAS, D.; BRUČAS, D.; DAUGĖLA, E.; MAČIULIS, L. Investigation of detection possibility of uavs using low cost marine radar. *Aviation*, v. 23, n. 2, p. 48–53, 2019.

[65] GONG, J.; YAN, J.; LI, D.; KONG, D.; HU, H. Interference of radar detection of drones by birds. *Progress In Electromagnetics Research M*, EMW Publishing, v. 81, p. 1–11, 2019.

[66] QUEVEDO, A. D. de; URZAIZ, F. I.; MENOYO, J. G.; LóPEZ, A. A. Drone detection with x-band ubiquitous radar. In: *2018 19th International Radar Symposium (IRS)*. [S.l.: s.n.], 2018. p. 1–10.

[67] NUSS, B.; SIT, L.; FENNEL, M.; MAYER, J.; MAHLER, T.; ZWICK, T. Mimo ofdm radar system for drone detection. In: *2017 18th International Radar Symposium (IRS)*. [S.l.: s.n.], 2017. p. 1–9.

[68] PALLOTTA, L.; CLEMENTE, C.; RADDI, A.; GIUNTA, G. A feature-based approach for loaded/unloaded drones classification exploiting micro-doppler signatures. In: *2020 IEEE Radar Conference (RadarConf20)*. [S.l.: s.n.], 2020. p. 1–6.

[69] FURUNO. *Operator's Manual: Marine Radar/Arpa Model FAR-21x7(-BB) series*. Nishinomiya, Japão, 2004.

[70] ALTAIR. *Altair Feko: High-Frequency Electromagnetic Simulation Software*. 2023. Accessed: 2023-12-26. Disponível em: <https://altair.com/feko/>.

[71] MSC. Adoption of the revised performance standards for radar equipment. *Resolution MSC.192(79)*, 2004.

[72] SOARES, A. S.; SOARES, W. S. L.; COLEN, G. R.; SILVEIRA, A. P. da; SAMPAIO, P. V. G.; MAGRI, V. P. R. Análise da detecção de drones por radar marítimo de navegação empregando o software advanced refractive effects prediction system (areps). *Revista Pesquisa Naval*, v. 1, n. 33, p. 59–65, 2021.

[73] ANAC. *Classification of Drones*. August 2018. Agência Nacional de Aviação Civil (ANAC). Accessed: January 16, 2024. Disponível em: <https://www.anac.gov.br/en/drones/classification-of-drones>.

[74] EZUMA, M.; ANJINAPPA, C. K.; SEMKIN, V.; GUVENC, I. Comparative analysis of radar-cross-section- based uav recognition techniques. *IEEE Sensors Journal*, v. 22, n. 18, p. 17932–17949, 2022.

[75] EZUMA, M. Radar cross section based statistical recognition of uavs at microwave frequencies. *IEEE Transactions on Aerospace and Electronic Systems*, v. 58, n. 1, p. 27–46, 2022.

[76] KAPOULAS, I. K. Small fixed-wing UAV radar cross-section signature investigation and detection and classification of distance estimation using realistic parameters of a commercial anti-drone system. *Drones*, MDPI, v. 7, n. 1, p. 39, 2023.

[77] SEMKIN, V. Analyzing radar cross section signatures of diverse drone models at mmwave frequencies. *IEEE access*, IEEE, v. 8, p. 48958–48969, 2020.

[78] FU, R. Deep learning-based drone classification using radar cross section signatures at mmwave frequencies. *IEEE Access*, IEEE, v. 9, p. 161431–161444, 2021.

[79] SEDIVY, P.; NEMEC, O. Drone rcs statistical behaviour. In: *Proceedings of the MSG-SET-183 Specialists' Meeting*. [S.l.: s.n.], 2021. p. 4–1–4–18.

[80] BURNHAM, K. P.; ANDERSON, D. R. *Model selection and multi-model inference: a practical information-theoretic approach*. 2nd. ed. [S.l.]: Springer-Verlag, 2004.

[81] SEMKIN, V.; HAARLA, J.; PAIRON, T.; SLEZAK, C.; RANGAN, S.; VIIKARI, V.; OESTGES, C. Drone rcs measurements (26-40 ghz). IEEE Dataport, 2019. Disponível em: <https://dx.doi.org/10.21227/m8xk-dr55>.

APPENDIX A – Probability Density Functions (PDFs) and Cumulative Distribution Functions (CDFs)

The PDFs and CDFs of the probability distributions used in this thesis and not presented are:

1 - Exponential PDF:

$$f(x) = \begin{cases} \frac{1}{\gamma} e^{-\frac{x}{\gamma}} & , x \geq 0 \\ 0 & , x < 0 \end{cases} \tag{A.1}$$

in which x is the random variable and γ is the parameter.

CDF:

$$F(x) = \begin{cases} 1 - e^{-\frac{x}{\gamma}} & , x \geq 0 \\ 0 & , x < 0 \end{cases} \tag{A.2}$$

in which x is the random variable and γ is the parameter.

2 - Gamma distribution PDF:

$$f(x; a, b) = \frac{b^a x^{a-1} e^{-bx}}{\Gamma(a)} \tag{A.3}$$

in which x is the random variable, $a > 0$ is the shape parameter, $b > 0$ is the rate parameter, and $\Gamma(a)$ is the Gamma function.

CDF:

$$F(x; a, b) = \frac{\gamma(a, bx)}{\Gamma(a)} \tag{A.4}$$

in which $\gamma(a, bx)$ is the lower incomplete gamma function.

3 - Generalized Extreme Value PDF:

$$f(x;\mu,\sigma,\xi) = \frac{1}{\sigma}\exp\left(-\left(1+\xi\frac{x-\mu}{\sigma}\right)^{-\frac{1}{\xi}}\right)\left(1+\xi\frac{x-\mu}{\sigma}\right)^{-\frac{1}{\xi}-1} \tag{A.5}$$

in which x is the random variable, ξ is the shape parameter, $\sigma > 0$ is the scale parameter, and μ is the location parameter.

CDF:

$$F(x;\mu,\sigma,\xi) = \exp\left(-\left(1+\xi\frac{x-\mu}{\sigma}\right)^{-\frac{1}{\xi}}\right) \tag{A.6}$$

4 - Generalized Pareto PDF:

$$f(x;\theta,\sigma,k) = \frac{1}{\sigma}\left(1+k\frac{x-\theta}{\sigma}\right)^{-\frac{1}{k}-1} \tag{A.7}$$

in which x is the random variable, k is the shape parameter, $\sigma > 0$ is the scale parameter, and θ is the location parameter.

CDF:

$$F(x;\theta,\sigma,k) = 1-\left(1+k\frac{x-\theta}{\sigma}\right)^{-\frac{1}{k}} \tag{A.8}$$

5 - Log-normal PDF:

$$f(x) = \frac{1}{x\gamma\sqrt{2\pi}}\exp\left(-\frac{(\ln x-\mu)^2}{2\gamma^2}\right) \tag{A.9}$$

CDF:

$$F(x) = \frac{1}{2}\left[1+\mathrm{erf}\left(\frac{\ln x-\mu}{\gamma\sqrt{2}}\right)\right], \tag{A.10}$$

in which $x > 0$, μ is the mean of the logarithm of the random variable, γ is the standard deviation of the logarithm of the random variable, and erf is the error function.

6 - Nakagami PDF:

$$f(x;m,\Omega) = \frac{2m^m}{\Gamma(m)\Omega^m}x^{2m-1}\exp\left(-\frac{m}{\Omega}x^2\right) \tag{A.11}$$

in which x is the random variable, $m > 0$ is the shape parameter, and $\Omega > 0$ is the spread parameter.

CDF:

$$F(x;m,\Omega) = P\left(m,\frac{m}{\Omega}x^2\right) \tag{A.12}$$

in which $P(m,z)$ is the regularized lower incomplete gamma function.

7 - Rayleigh PDF:

$$f(x;\sigma) = \frac{x}{\sigma^2} \exp\left(-\frac{x^2}{2\sigma^2}\right) \tag{A.13}$$

in which x is the random variable and $\sigma > 0$ is the scale parameter.

CDF:

$$F(x;\sigma) = 1 - \exp\left(-\frac{x^2}{2\sigma^2}\right) \tag{A.14}$$

8 - Rician PDF:

$$f(x;s,\sigma) = \frac{x}{\sigma^2} \exp\left(-\frac{x^2+s^2}{2\sigma^2}\right) I_0\left(\frac{xs}{\sigma^2}\right) \tag{A.15}$$

in which x is the random variable, s is the non-centrality parameter, $\sigma > 0$ is the scale parameter, and I_0 is the modified Bessel function of the first kind with order zero.

CDF:

$$F(x;s,\sigma) = 1 - Q_1\left(\frac{s}{\sigma}, \frac{x}{\sigma}\right) \tag{A.16}$$

in which $Q_1(a,b)$ is the Marcum Q-function.

9 - Weibull PDF:

$$f(x;\lambda,k) = \frac{k}{\lambda}\left(\frac{x}{\lambda}\right)^{k-1} \exp\left(-\left(\frac{x}{\lambda}\right)^k\right) \tag{A.17}$$

in which x is the random variable, $\lambda > 0$ is the scale parameter, and $k > 0$ is the shape parameter.

CDF:

$$F(x;\lambda,k) = 1 - \exp\left(-\left(\frac{x}{\lambda}\right)^k\right) \tag{A.18}$$

APPENDIX B – Measured RCS

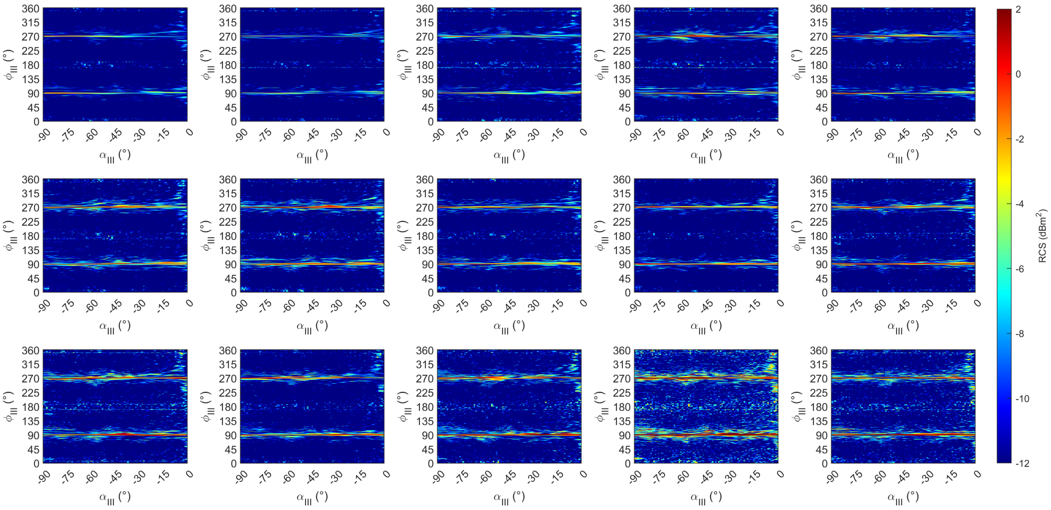

Figure B.1: Measured RCS of the DJI Mavic Pro for frequencies ranging from 26 to 40 GHz.

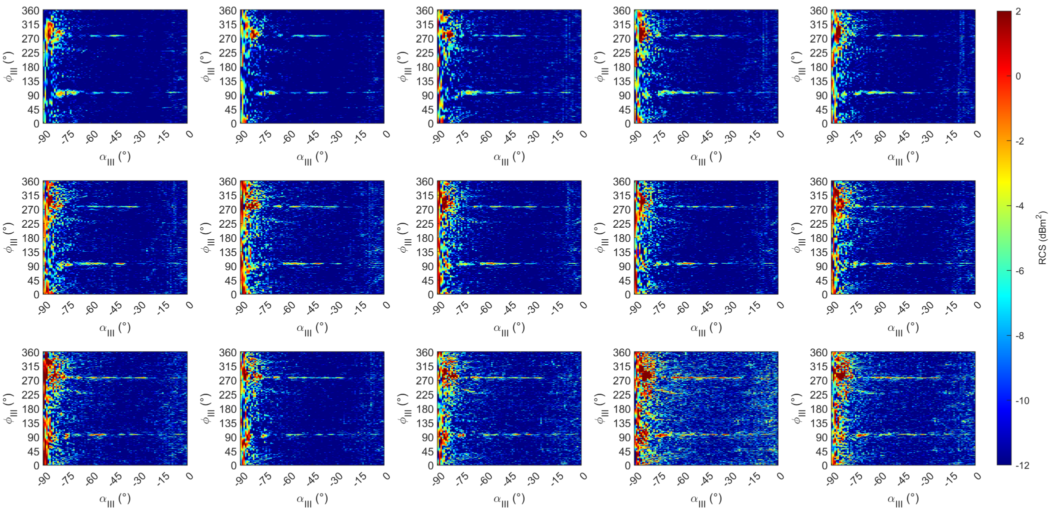

Figure B.2: Measured RCS of the DJI F450 for frequencies ranging from 26 to 40 GHz.

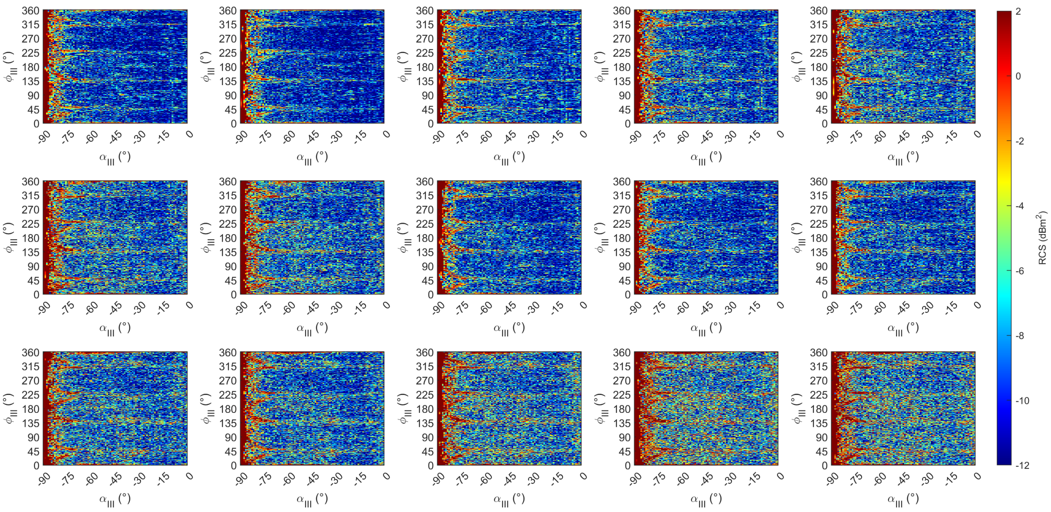

Figure B.3: Measured RCS of the DJI Matrice 100 for frequencies ranging from 26 to 40 GHz.

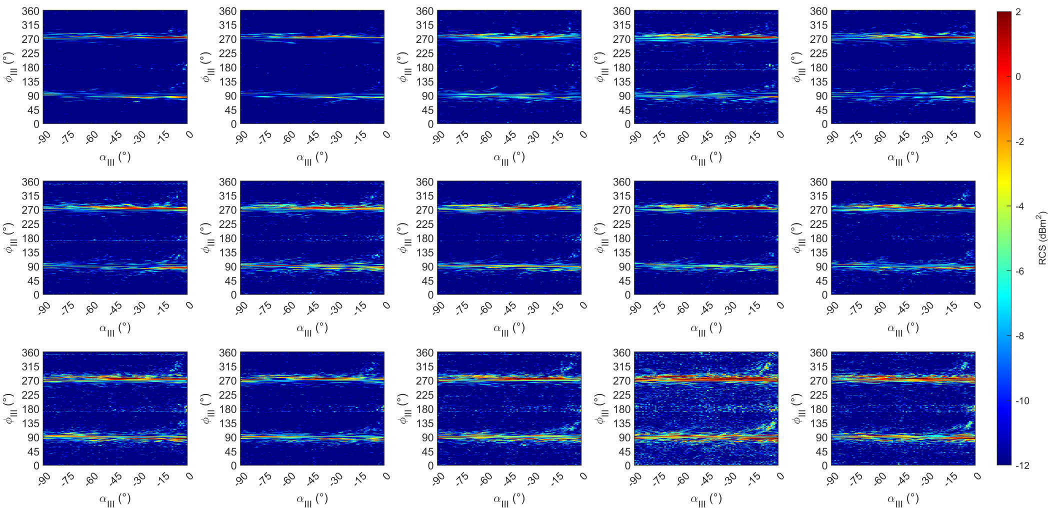

Figure B.4: Measured RCS of the Parrot AR.Drone for frequencies ranging from 26 to 40 GHz.

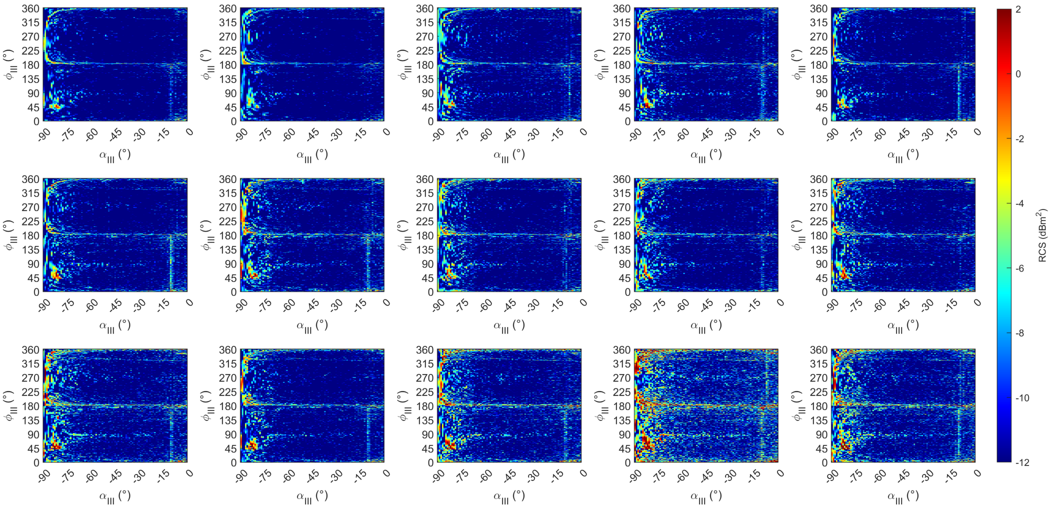

Figure B.5: Measured RCS of the Helicopter Kyosho for frequencies ranging from 26 to 40 GHz.

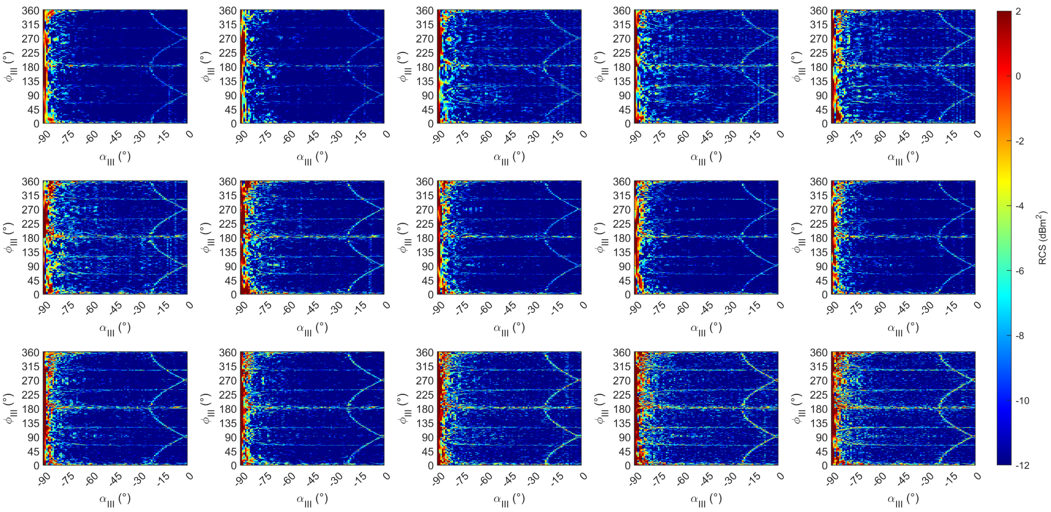

Figure B.6: Measured RCS of the HMF Y600 for frequencies ranging from 26 to 40 GHz.

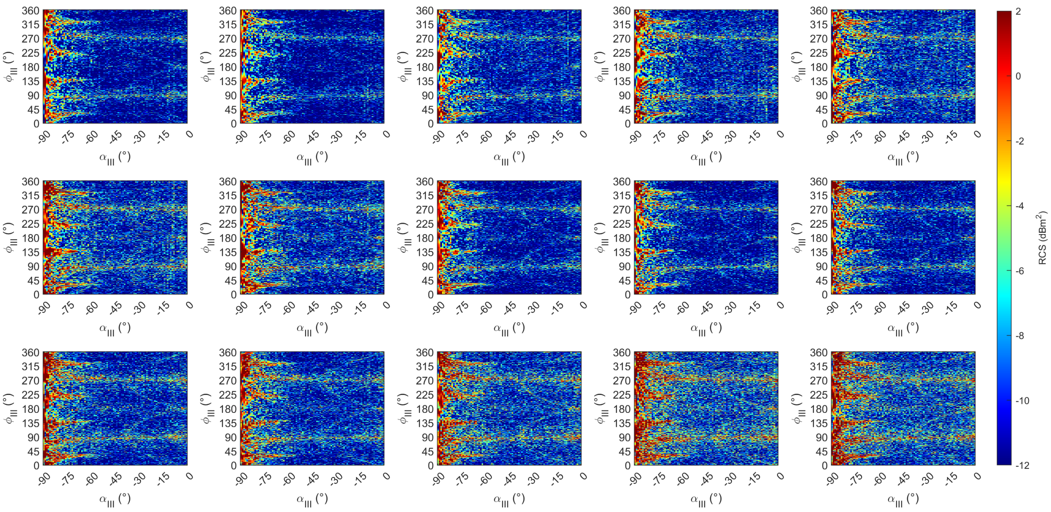

Figure B.7: Measured RCS of the Walkera Voyager 4 for frequencies ranging from 26 to 40 GHz.

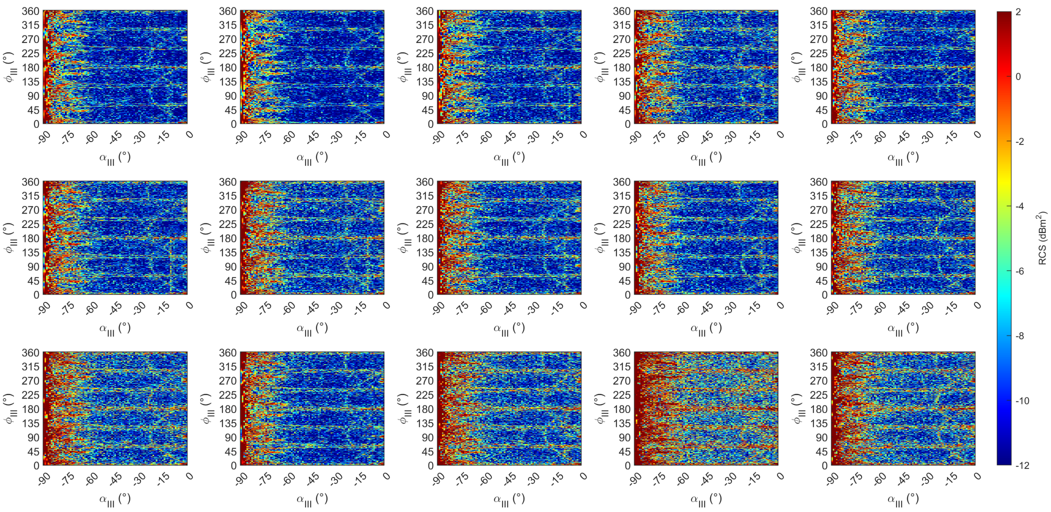

Figure B.8: Measured RCS of the custom Hexacopter for frequencies ranging from 26 to 40 GHz.